An Integrated Approach for Assessing the Impact of Tunnel Excavations in Urban Areas



Gianluigi Della Ragione

Department of Civil, Building and Environmental Engineering
University of Naples Federico II

This dissertation is submitted for the degree of
Doctor of Philosophy

Naples
January 2024

Supervisor
Prof. Emilio Bilotta

Qualis pater, talis filius.
Ad perpetuam rei memoriam.

Declaration

I hereby declare that this dissertation is the result of my own work and includes nothing which is the outcome of work done in collaboration except where specified in the text. I further state that no substantial part of my dissertation has already been submitted, or, is being concurrently submitted for any such degree, diploma or other qualification at the University of Naples Federico II or any other University or similar institution.

Acknowledgments

I had never thought in my life about attending a doctoral course. But as we know, life cannot be planned as one would like. Despite this, it was incredibly pleasant to have dedicated three years of my life to research in subjects and topics unknown to me. It is obvious that my experience at the University of Cambridge has radically changed my way of thinking and, above all, the way in which I approach the new, which can be intimidating, but which can turn out to be a magnificent experience if approached with curiosity and a spirit of challenge. Well, in a Country (the Italian one) in which scientific research is placed at the same level as the most humble jobs, the very first thanks goes to the sacrifices made by my family for the support received. To my father, admirable worker. To my mother, who always believed in me. To my brother, who showed me that you can do even better. To my Lauren, who tirelessly supported and put up with me (and will put up with me for many years to come!). The doctoral experience was very rewarding, and for this reason I express heartfelt thanks to my supervisor, Prof. Emilio Bilotta, who allowed me to calmly study interesting and innovative topics in the geotechnical engineering sector (i.e. fiber optics and satellite interferometry). A warm thank you also to colleagues from the University of Cambridge including Dr. Christelle Abadie and Dr. Xiaomin Xu, and to colleagues from the Polytechnic University of Barcelona including Prof. Alessandra di Mariano. A heartfelt thank you to Prof. Daniele Perissin and the dear Alfredo Rocca for having introduced me so well into the sector of satellite interferometry. Finally, thanks to all those friends who not only took an interest in my studies, but shared good and bad moments with me, above all Alfonso, Gere, Giuseppe, Stefano.

Abstract

In the evolving landscape of civil engineering, innovative monitoring solutions play a pivotal role, particularly in industrialized societies. This thesis delves into the application of two advanced monitoring techniques, Distributed Fibre Optic Sensing (DFOS) and Interferometric Synthetic Aperture Radar (InSAR), within the realm of geotechnical engineering, focusing on tunneling excavations in urban environments.

The exploration of DFOS begins with small-scale experiments and 3D Finite Element Analysis (FEA). Numerical results showcase the technique's efficacy in real-world scenarios. The thesis then transitions to InSAR, employing it in two real case studies: the metro lines in Naples and Barcelona. The first case investigate the technique's suitability for free-field conditions, while the second assesses tunnel-induced displacements on a residential structure affected by excavation.

DFOS emerges as a robust method for the detection of strain profiles at depth caused by excavations. However, further research is needed, especially concerning the soil-cable interface in diverse soil types. At the same time, InSAR proved adapted at capturing superficial tunnel-induced subsidence, albeit constrained by the limitations of its one-look side geometry.

This research contributes to the advancement of geotechnical engineering monitoring techniques, providing valuable insights for assessing the impacts of tunneling in urban settings. The findings underscore the significance of merging experimental validations with real-world applications, paving the way for refined monitoring practices in civil engineering.

Contents

1 Introduction **1**

1.1 Background 1

1.2 Application areas 4

1.3 Aim and objective of research 6

1.4 Overview of thesis 6

2 Literature review **8**

2.1 Introduction 8

2.2 Review on DFOS monitoring 12

2.2.1 Background on DFOS technique 12

Basic principles of Brillouin scattering 16

Basic principles of Rayleigh scattering 17

2.2.2 General applications of DFOS monitoring 18

Crack monitoring for structures 18

Bridge monitoring 19

Pile monitoring 20

Tunnel monitoring 22

Slope and landslide monitoring 23

2.2.3 DFOS for subsidence monitoring 24

2.3 Review on InSAR monitoring 26

2.3.1 Overview of SAR satellites for InSAR applications 26

2.3.2 A review of InSAR techniques 29

2.3.3 Satellite InSAR for tunnelling-induced subsidence monitoring . . 32

2.4 Review on tunnel excavations 37

2.4.1 Empirical method for vertical displacements 37

2.4.2 Empirical method for horizontal displacements 40

3 Methodology **42**

3.1 Fibre optics testing 42

3.1.1 Tests with DFOS cables . . . 43
Experimental rig . . . 43
Particle Image Velocimetry and LVDTs . . . 44
Fibre optic cable and analyser . . . 45
Full scale validation . . . 47
3.1.2 Numerical model . . . 47
Geometry and meshing . . . 47
Stiffness decay with strain level at low confining stress . . . 50
Dependency of the stiffness on stress at medium to large strain level 51
3.2 Interferometric SAR technique . . . 54
3.2.1 Background on electromagnetic waves . . . 55
Fundamentals of electromagnetic waves . . . 55
Electromagnetic waves in radar systems . . . 56
3.2.2 Radar image characteristics . . . 59
The amplitude of radar images . . . 59
The phase of radar images . . . 62
3.2.3 SAR interferometry . . . 64
Flat terrain phase component . . . 67
Topographic phase component . . . 69
Displacement phase component . . . 70
Atmospheric phase component . . . 73
3.2.4 Persistent Scatterers Interferometry . . . 73
3.2.5 Synthetic InSAR displacements from tunnelling . . . 78

4 Applications and results 83
4.1 Fibre optic sensing . . . 83
4.1.1 Validation of numerical results . . . 83
4.1.2 Results of small scale tests . . . 86
4.1.3 Large scale application . . . 95
Plane strain conditions . . . 95
Axialsymmetric conditions . . . 98
4.2 MT-InSAR - Naples . . . 101
4.2.1 Introduction . . . 101
4.2.2 Excavation details and geological conditions . . . 102
4.2.3 MT-InSAR monitoring . . . 104
Assessment of the AoI before the excavations . . . 107
Displacements maps after the excavations . . . 108
Empirical settlement prediction . . . 109

Volume loss assessment from MT-InSAR data 110
4.3 MT-InSAR - Barcelona 113
4.3.1 Introduction 113
4.3.2 Excavation details and geological conditions 114
4.3.3 Numerical analysis 116
4.3.4 MT-InSAR monitoring 118
Assessment of the AoI before the excavation 118
Displacements map after the excavation 120
Comparison with traditional monitoring 122
Comparison with 3D numerical analysis 125

5 Conclusions **128**

Appendix A **132**
Solution of Equation 3.46 132
Solution of Equation 3.47 133
Proof $V_L^* = V_L$ 134

Bibliography **135**

List of Figures

1.1 Gartner hype cycle, modified after Soga 2023 3

2.1 General components of a fibre optic cable: core, cladding and buffer coating. 12

2.2 Frequencies of the backscattered light (modified afer Güemes, Fernández-López and Soller 2010). 14

2.3 Historic and recent radar satellite missions. Figure downloaded from EO College - 2023. 27

2.4 Subsidence map of Pomona City detected via PSInSAR analysis (Ferretti, Prati and Rocca 2000). 33

2.5 Time series relative to one scattered identified as point P2 in the subsiding area (Ferretti, Prati and Rocca 2000). 33

2.6 Subsidence map of Beijing area in the year of 2009, adapted from Ge et al. 2011 34

2.7 Subsidence map around Line 7, 9, 10, 11 and 14 of the Shanghai subway (Perissin, Z. Wang and Lin 2012). Note the settlements detected via PS analysis along the tunnel stretches. 35

2.8 (a) Transverse subsidence profile near Xiaonanmen Station on Line 9 (Perissin, Z. Wang and Lin 2012). (b) Transverse subsidence profile near Laoximen Station on Line 10 (Perissin, Z. Wang and Lin 2012). 35

2.9 (a) Settlement trough on the surface resulting from tunnel excavation, adapted from Rankin 1988. (b) Transversal settlement profile with the indication of key elements: the inflection point position denoted as i_x, the maximum settlement marked as w_{max}, and the position of the tunnel. 37

2.10 (a) Variation of inflection point location i_x with tunnel depth z_0 for tunnels in clays. (b) Variation of inflection point location i_x with tunnel depth z_0 for tunnels in sands and gravels (modified after Mair and Taylor 1997) 38

2.11 (a) Superposition of effects using Equation 2.8 when $\Delta x < 2i_x$. (b) Superposition of effects using Equation 2.8 when $\Delta x > 2i_x$. The black solid lines represent two Gaussian profiles of both tunnels (1 and 2) and the solid red line represents the superposition of effects. 39
2.12 Direction of ground displacement vectors above tunnels in clays (modifed after Mair and Taylor 1997). (a) Vectors directed towards tunnel axis (Attewell 1978, O'Reilly and New 1982). (b) Vectors directed below tunnel axis (Taylor 1995). 40

3.1 Photograph of the experimental set-up for the 1g tests. 44
3.2 Schematic representation of experimental strain sensing cable cross section (courtesy Dr. Xiaomin Xu). 46
3.3 Plaxis 3D numerical model representing half of the plane-strain problem with soil modelled as tetrahedral element and fibre-optic cable modelled as an embedded beam element ($395 \times 200 \times 200mm$). Dimensions in mm. 48
3.4 Atmospheric signal transmission (adapted from Henderson and Lewis 1998), with the indication of the main bands used in satellite remote sensing. 54
3.5 Equation 3.15 with the indication of the phase ϕ and amplitude A of the wave function. 56
3.6 Plot of *cardinal sine* 57
3.7 Radar resolution in azimuth direction. Point A and B (or A and C) have different range and can be uniquely identified. Point B and C fall within the same resolution cell in azimuth direction and cannot be uniquely identified. 58
3.8 Amplitude of an acquisition in descending orbit made by Sentinel 1 on March 28^{th} 2021 over the city of Naples, Italy. Notice the presence of strong scatters in the urban area while the sea and the vegetations show poor scattering. Figure obtained using the software SARproZ (Perissin, Z. Wang and T. Wang 2011). 60
3.9 Layover and shadow effects. In red the detected scatters. 61
3.10 Foreshortening and shadow. In green the cells affected by foreshortening. 62
3.11 Phase of an acquisition in descending orbit made by Sentinel 1 on March 28^{th} 2021 over the city of Naples, Italy. The phase illustrated here refers to the same image shown in Figure 3.8. Figure obtained using the software SARproZ (Perissin, Z. Wang and T. Wang 2011). 63
3.12 Interaction between targets within the same resolution cell. (a) Constructive interaction, (b) destructive interaction. 64

3.13 Interferogram between Sentinel 1 images acquired in descending orbits respectively on March 28^{th} 2021 (Master Image) and April 3^{rd} 2021 (Slave Image). Figure obtained using the software SARproZ (Perissin, Z. Wang and T. Wang 2011). 65
3.14 Acquistion geometry for interferogram formation. 67
3.15 Interferogram of Figure 3.13 after removing the flat phase component using Equation 3.26. Figure obtained using the software SARproZ (Perissin, Z. Wang and T. Wang 2011). 68
3.16 Digital Elevation Model (DEM) from the Shuttle Radar Topography Mission (SRTM) 1 Arc-Second. DEM obtained from the U.S. Geological Survey database. Figure obtained using the software SARproZ (Perissin, Z. Wang and T. Wang 2011). 71
3.17 Interferogram of Figure 3.15 after removing the topographic phase component using Equation 3.27. Figure obtained using the software SARproZ (Perissin, Z. Wang and T. Wang 2011). 72
3.18 Conversion of a generic displacement $\vec{d}$ in a displacement along the line of sight of the satellite $\overrightarrow{d_{LOS}}$. 72
3.19 Types of connection graphs for interferograms generation. 76
3.20 (a) Influence of horizontal displacements on the assumption inherent in Equation 3.41, under the assumption that the cross section is contained in the LOS plane. (b) Effect of the angular deviation γ between the cross-sectional plane and the line-of-sight plane on the magnitude of horizontal monitored displacements. 80
3.21 (a) Amplification factor of settlement peaks as a function of the local incidence angle ϑ' and the geotechnical parameter k. (b) Maximum settlement shift as a function of the local incidence angle ϑ' and the geotechnical parameter k. 81

4.1 (a) Image acquired from the Canon Powershot G10, used for PIV analysis. (b) Numerical half-space deformed mesh. (c) Experimental contour plot of vertical displacements from PIV. (d) Numerical contour plot of vertical displacements (D_R=52% δ=2 mm). 84
4.2 (a) Vertical displacements from PIV and numerical results. (b) Horizontal displacements from PIV and numerical results. (D_R=52% δ= 2 mm and z=150 mm). 84
4.3 (a) Soil strain from PIV and strain within the fibre optic cable. (b) Numerical horizontal soil strain, rough and smooth cables numerical strain. (1g test, D_R=52%, δ=2 mm and z=150 mm). 85

4.4 Geometry for strain calculation 86

4.5 Comparison between soil strains induced by (a) horizontal, (b) vertical and (c) total displacement in the $1g$ experimental results and numerical analysis of the laboratory test, far from the cables (D_R=20%, δ=1 mm, z=150 mm). 88

4.6 Comparison between cable strains induced by (a) horizontal, (b) vertical and (c) total displacements in the 1g experimental results and numerical analysis of the laboratory test (D_R=20%, δ=1 mm, z=150 mm, rough cable). 89

4.7 Comparison between soil strains from horizontal movements at different densities and at three heights in the soil body in the $1g$ experimental results and numerical analysis of the laboratory test, far from the cables (δ=1 mm). 90

4.8 Comparison between horizontal cable strains at different densities and at three heights in the soil body in the $1g$ experimental results and numerical analysis of the laboratory test, rough cables (δ=1 mm). . . . 91

4.9 Horizontal and vertical displacement of numerical cables for D_R=52% and δ=1 mm, comparison between rough and smooth cables. (a), (d) Top cable; (b), (e) central cable; (c), (f) bottom cable. 93

4.10 Strain induced by horizontal movements for D_R=52% and δ=1 mm, comparison between soil's strain (far from and close to the cable) and the rough cable for: (a) top layer and top cable; (b) central layer and central cable; (c) bottom layer and bottom cable. 94

4.11 Comparison between centrifuge experimental and numerical surface soil settlement profiles. 96

4.12 Comparison between rough and smooth cable, top cable δ=40 mm: (a) strains induced by horizontal displacements; (b) strains induced by vertical settlements; (c) total strains induced by horizontal and vertical displacements. 97

4.13 Plaxis 3D numerical model representing a quarter of the axisymmetric problem with soil modelled as tetrahedral element and fibre optic cable modelled as an embedded beam element ($15.8 \times 15.8 \times 4$ m). Dimensions in meters. 99

4.14 (a) Soil settlements at z=3 m above circular trapdoor. (b) Rough cables settlements at z=3 m above circular trapdoor. (δ=40 mm). 99

4.15 Horizontal strain profiles within the cable in axial symmetric conditions for δ=40 mm: (a) $y/D = 0$; (b) y/D=0.25; (c) y/D=0.50; (d) y/D=0.75; (e) y/D=1.00; (f) y/D=1.25; (g) y/D=1.50; (h) y/D=2.00. 100
4.16 City of Naples, Italy. Highlighted in blue is the city center and in orange is the airport of Capodichino. The red solid line represents the city bounds. (Image modified after Google Earth©, Google) 101
4.17 (a) Metro Line 1 of the city of Naples. The existing line is represented with a continuous line, while the extension is represented with a dashed line. In dashed orange the segment Capodichino-Poggioreale. (b) Google Earth map of the Area of Interest (in blue). Red lines represent the longitudinal axes of the excavated tunnels (after [24]). In orange the cemetery of Poggioreale. (Image modified after Google Earth©, Google) 102
4.18 Geological section between Poggioreale and Capodichino stations 103
4.19 (a) Reflectivity Map (RM) and (b) subset of RM showing the analysed area and in red the tunnel alignments. Both figures are viewed in the local satellite coordinate system (Line and Sample directions, i.e. Azimuth and Range directions) 105
4.20 Interferogram network (single Master PS analysis), where it can be noted the timeline of data acquisition and normal baseline with reference to the Master Image (December 23^{rd} 2019) 106
4.21 Example of time series multi-linear interpolation. Each colored line represents a linear interpolation. Notice that this scatter lies on the longitudinal axis of the first excavated tunnel (coherence γ =0.85.) . . . 107
4.22 Cumulative displacements in mm along the LOS occurred from March 7^{th} 2018 to July 2^{nd} 2020, prior the beginning of the first tunnel excavation. (Image modified after Maxar for Microsoft) 108
4.23 (a) Cumulative displacements in mm along the LOS occurred from to July 2^{nd} 2020 to March 23^{rd} 2021, due to the excavation of the first tunnel (right red longitudinal axes). (b) Cumulative displacements along the LOS occurred from to July 2^{nd} 2020 to January 29^{th} 2022, due to the excavation of both tunnels. (Images modified after Maxar for Microsoft). 109
4.24 Comparison between monitored data projected on the vertical plane (black dots) and predicted settlement profiles d_v using Equation 3.48 (dashed-solid-dashed lines for V_L=0.25, 1, and 1.75%, respectively). Sections A to I refer respectively to those in Figures 4.23 (a), (b). . . . 111
4.25 First excavation - monitored settlements d_v (black dots) vs Gaussian fit (solid red line, Equation 3.48). 112

4.26 Second excavation - monitored settlements d_v (black dots) vs Gaussian fit (solid red line, Equation 3.48). The profiles are centered on the first tunnel axis. 113
4.27 Overview of Metro Line 9 in Barcelona (Di Mariano 2023). 114
4.28 Portion of section number 2 of Figure 4.27. Area of Interest (AoI) with the indication of the Metro Line 9 (red solid line) and the monitored residential complex (in orange solid texture). 115
4.29 Geological profile of the tunnel alignment in the area of study. 115
4.30 Conventional monitoring at PK4888, in proximity to the monitored residential building. 116
4.31 Finite Element Model for the excavation. D is the tunnel diameter. . . 117
4.32 Velocity displacement map of the AoI from January 7^{th} 2009 to October 2^{nd} 2012. 119
4.33 Line of sight cumulative displacements in mm from January 7^{th} 2009 to January 25^{th} 2011, prior the beginning of the excavation. 120
4.34 Line of sight cumulative displacements along the LOS from January 25^{th} 2011 to October 2^{nd} 2012, induced by the excavation. 121
4.35 (a) Geographic location of traditional instrumentations (black markers) with the indication of the selected Permanent Scatterers for comparison; (b) history time series comparison between traditional mon-itoring stations (black lines) and InSAR scatterers (solid lines with circle markers). 123
4.36 Induced settlement trough at six different locations. Comparison between Levelling Points (LP, red markers and solid lines) data and satellite data (InSAR, black circles, fitting blue solid line). 123
4.37 Section A. Location of traditional monitoring stations: over the building roof (T2F04912R020HM322Z) and at the street level (T2F4896L037HN007W). Location of the selected InSAR scatter at street level. 124
4.38 Building displacements. Comparison between Levelling Point (LP, black squared markers) data and satellite data (InSAR, circle markers). . . . 125
4.39 Time series comparison between InSAR scatterer, levelling point and corresponding FEA output. The point selected lies at street level. . . . 126
4.40 Settlement trough: satellite data (InSAR), conventional optical levelling (LP) and FEA results. Section A of Figure 4.36. 126
4.41 Comparison between InSAR, LP and FEA for Block B roof displacement. 127

List of Tables

2.1 Conventional and innovative monitoring techniques for surface and subsurface settlement monitoring (adapted after Möller et al. 2023 and Gutiérrez et al. 2019). 11
2.2 Fibre optic analysers (Kechavarzi et al. 2016). 15
2.3 Characteristics of the main PSI approaches (Crosetto, Monserrat et al. 2016). 31
2.4 Comparison of leveling data and PSInSAR, adapted from Ge et al. 2011 34

3.1 Hostun sand properties (Da Silva Burke and M. Z. E. B. Elshafie 2021). 43
3.2 Centrifuge test properties at prototype scale (Da Silva Burke 2018). . . 47
3.3 Constitutive parameters values used in the HSsmall model for the soil. 53
3.4 Wavelength bands used in satellite remote sensing. 55

4.1 Stratigraphic model for the station of Capodichino (modified after Regione Campania 2013). 104
4.2 Stratigraphic model for the station of Poggioreale 104
4.3 Percentage of monitored scatters that fall within the expected range. . 110
4.4 Soil parameters for the Barcelona metro line 9 case (Török 2021). . . . 118

Chapter 1

Introduction

Scientific progress is radically related to the continuous perfection of the measurement tools. Improving those allow to acquire more accurate data, paving the way for more significant discoveries and a deeper understanding of natural phenomena. Precise measurements are the foundation on which scientific knowledge is built.

1.1 Background

A crucial issue for our planet, as well as for our future, is the safeguarding of the environment. The environment, with which we are inevitably interconnected in our daily actions, presents us with a clear challenge known as " climate change ".

In this perspective, in Italy, the Ministry of the Environment and Energy Security has recently published the new National Plan for Climate Change Adaptation (PNACC), incorporating international agreements (including the Kyoto Protocol, the Paris Agreement and the 2030 Agenda) and European plans and programs (such as the European Climate Change Programme and the European Green Deal). The PNACC highlights that geological and hydro-geological disasters, such as landslides, floods, and erosion, pose a significant threat to the environment and the Italian economy. Consider that, according to the report made by ISPRA (Italian Institute for Environmental Protection and Research) on hydro-geological disasters, 94% of Italian municipalities are at risk of landslides, floods, and/or coastal erosion, and 8 million people live in high-risk areas. While the complexities of hydro-geological disasters are acknowledged, precipitation often plays a decisive role in triggering these events, especially in the context of climate change, which has led to increasingly brief but extremely intense

rainfall.

On one hand, predicting the sudden evolution of phenomena like landslides, floods, and erosion is challenging. On the other hand, it is possible to integrate monitoring techniques for the control and protection of both the territory and the population. Indeed, the PNACC emphasise that 'Adaptation' means anticipating the adverse effects of climate change and adopting appropriate measures to prevent or minimize the damages they can cause.

In support of the decision-making process, in the recent years, advancements in technology have revolutionized the way of monitoring and assessing ground movements, buildings, infrastructures and environmental changes. Several innovative monitoring techniques have emerged, such as but not limited to Interferometric Synthetic Aperture Radar (InSAR), Light Detection an Ranging (LiDAR), Distributed Acoustic Sensing (DAS), Distributed Fibre Optic Sensing (DFOS) and Wireless Sensor Network (WSN), providing more accurate and real-time data for improved decision-making and enhanced safety when compared with traditional monitoring methods (i.e. levelling points, total station, etc.).

The use of monitoring techniques is crucial in civil engineering for several reasons. First, as urbanization continues to accelerate, engineers and city planners face the challenge of constructing infrastructure in densely populated areas. Construction of tunnels, bridges, and other structures beneath or in close proximity to existing buildings and infrastructure can induce ground movements and subsidence, thereby increasing the risk of inducing damage. Such consequences can have a severe impact on public safety and property. Secondly, the importance of sustainable construction practices and the minimization of environmental impacts cannot be underestimated. Monitoring techniques help in identifying and addressing potential problems early in the construction phase, reducing the need for costly and disruptive repairs later on. Additionally, they aid in optimizing construction processes, leading to more efficient resource utilization.

Toward this orientation, nowadays, satellite InSAR technique is emerging as a powerful tool in detecting millimetre displacements on vast areas (i.e. $\geqslant 1.600$ km^2 and up to ≈ 30.000 km^2) with a diversity of spatial resolutions (i.e. from 30×30 m^2 to

1×1 m^2), which are rapidly increasing as result of the entry of private investments in this field. Satellites provide constant information of the Earth changes with a revisit time of a few days up to some week (depending on the satellite constellation), enabling the monitoring of slow movements in time (relative to the satellite revisit time). On the other hand as well, Fiber Optic cables are a versatile and robust monitoring solution when embedded in the ground near construction sites or infrastructures. These cables (which are commonly used in telecommunication systems) are sensitive to mechanical and temperature induced strain. Therefore when ground movement occurs the cables transmit data to an analyser so that information can be retrieved to assess subsidence and other deformation patterns, well before its effects are visible at the surface and detected by satellites. It's worth noting that the time required to derive outputs from satellite data does not allows for real time information. Moreover, Fiber Optic can be deployed for tens of kilometers, allowing the monitoring of long infrastructures with an high sampling frequency (from 1 mHz to 100 Hz) and an extremely high accuracy (up to 10 $\mu\varepsilon$).

Anyway, currently both technologies are facing a period of disillusionment and skepticism according to Soga 2023, as shown in Figure 1.1. This may be due to limitations inherent in the technologies and the analysis procedures associated with

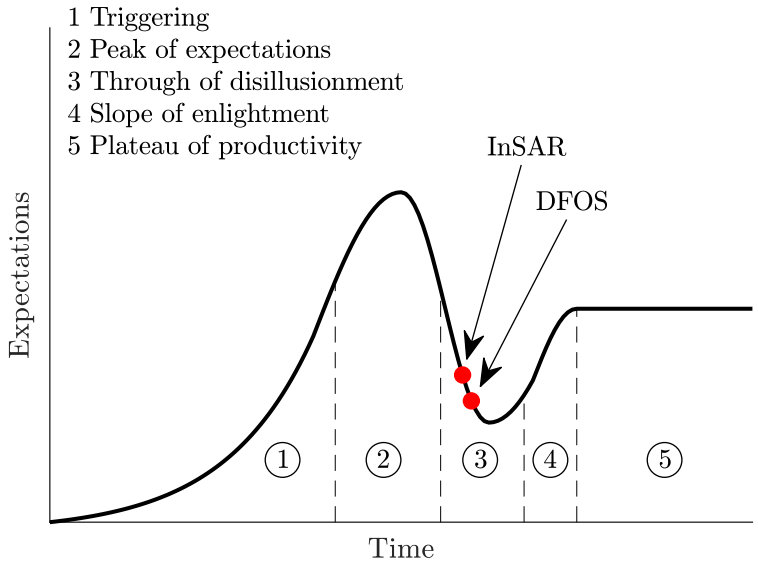


Figure 1.1: Gartner hype cycle, modified after Soga 2023

them. However, there's no doubt about the significant benefits that users can derive from the wealth of information these technologies can provide. Indeed, an intuitive reader may have already grasped the significant potential of what these two monitoring techniques can offer when utilized in conjunction, with wisdom and expertise.

1.2 Application areas

Satellite Interferometric Synthetic Aperture Radar (InSAR) and Distributed Fibre Optic Sensing (DFOS) monitoring techniques can be used for many applications. Since InSAR is able to detect Earth's surface movements of a large area with high precision, its use is directed toward a vast number of application such as, but not limited to:

- volcanic activity: InSAR can detect ground deformation around volcanoes, helping to predict eruptions and mitigate volcanic hazards. Being a remote sensing technique it is possible to monitor active volcanoes as well, where the presence of human surveying activities is difficult and dangerous;
- earthquakes: it can monitor tectonic plate movements (when these are visible at surface), or, after an earthquake, it can be used to assess the extent of permanent ground displacement and damage to infrastructure. This is vital for emergency response and recovery efforts, since data can help prioritize areas in need of immediate attention and resources;
- landslides: InSAR can identify regions at risk of landslides by detecting ground deformations associated with slope instability;
- subsidence: InSAR can monitor land subsidence caused by natural or human activities (e.g. groundwater extraction, underground constructions, consolidation of compressible soils during construction, etc.);
- infrastructure monitoring: InSAR helps assess the structural health of many infrastructures (i.e. bridges, dams, airports, highways, etc.) since it can detect small movements that may indicate stress or damage, allowing for preventative maintenance and safety measures;

- land use: InSAR data can guide land-use decisions in regions susceptible to ground movement, offering valuable insights that help urban planners and policymakers to make well-informed choices regarding the optimal locations for infrastructure development and expansion.

Furthermore, as satellites have been collecting data since the early 1990s, it is possible to conduct historical analysis of specific sites, enabling the retrieval of past information of deformation mechanism that would be otherwise impossible to investigate with alternative monitoring techniques.

While satellite InSAR provides data over an extensive area, Distributed Fibre Optic Sensing provides information on deformations along a fibre optic cable, with a spatial resolution ranging from a few meters up to a few millimeters. This relatively new technology has been used in many fields, including, but not limited to:

- structural health monitoring: DFOS can be used to monitor strain and temperature in infrastructure (e.g. bridges, buildings, pipelines, etc.), providing real-time data on structural integrity, helping to identify potential issues and prevent failures. In these cases, the fibre optic cable is attached onto the surface with special glues (e.g. epoxy resins), which provide a perfect bonding between the sensor and the structure;

- geotechnical monitoring: DFOS can be used to monitor many geotechnical problems (e.g. slopes, subsidence, retaining walls, rockfalls, stability and safety of tunnels and underground structures, etc.). In most of these cases the fibre optic cable is embedded in the soil;

- aerospace: DFOS can be employed to monitor the structural health of aircraft, detecting stress and strain in critical components;

- traffic monitoring: DFOS can monitor traffic flow and road conditions, providing data for traffic management and optimization.

1.3 Aim and objective of research

The aim of this study is to demonstrate the potential and limits of satellite Interferometric Synthetic Aperture Radar (InSAR) and Distributed Fibre Optic Sensing (DFOS) technologies when applied in civil engineering, with particular attention directed toward their application to tunnel excavations monitoring in built environments. Regarding the use of InSAR as monitoring tool for the effect induced by underground excavations, two case studies are presented, namely: Metro Line 1 in the city of Naples, that connects the airport of Capodichino with the Poggioreale station and viceversa, and the Metro Line 9 in the city of Barcelona, with a particular focus on a damaged residential complex. Satellite data are obtained using advanced interferometric algorithm (i.e. Multi-Temporal InSAR, MT-InSAR) and then compared with empirical methods, 3D Finite Element (FE) analysis and traditional monitoring, in pursuance of attesting their robustness and reliability.

In relation to the use of DFOS sensors as monitoring technique for settlements induced by underground excavations, a proof of concept is investigated through 1g experiments in a controlled environment. These experiments aim to replicate the arching mechanism, which is involved during underground excavation. Then, 3D FE analysis are carried out for a twofold reason: firstly, to validate and deeper investigate experimental results; secondly, to scale the results up to more realistic stress levels.

1.4 Overview of thesis

The layout of this thesis is as follows:

Chapter 2 (*Literature review*) presents a review of the relevant literature regarding the use of InSAR and DFOS as monitoring techniques in civil engineering, with a particular focus on tunneling excavations.

Chapter 3 (*Methodology*) presents the key methods used during this research project with details on:

- trapdoor tests setup, involving Particle Image Velocimetry (PIV) and Fibre Optic Sensing;
- advanced interferometry techniques (MT-InSAR);

Chapter 4 (*Applications and results*) describes the main case investigated in this research, presenting the key findings and limitations.

Chapter 5 (*Conclusions*) summarises the key findings of the thesis and proposes future recommendations for the research.

Chapter 2

Literature review

> *I often say that when you can measure what you are speaking about, and express it in numbers, you know something about it; but when you cannot measure it, when you cannot express it in numbers, your knowledge is of a meagre and unsatisfactory kind; it may be the beginning of knowledge, but you have scarcely, in your thoughts, advanced to the stage of science, whatever the matter may be.*
>
> Lord William Thomson, 1883

2.1 Introduction

The need for new infrastructures in densely populated cities due to the increasing global population (Vollset et al. 2020), as well as the increasing migration from rural to urban areas (Young 2013), must be satisfied. Intensive land use in the previous decades has saturated the space for the creation of new superficial infrastructures (i.e., roads, railways, and so on). Thus, the demand for mobility is directed towards the exploration of the still intact underground space, where it can be satisfied through the construction of underground infrastructures, including tunnels. Tunnel excavation in developed areas, while a delicate task to accomplish, may also pose a risk to the surrounding space, because the potential of causing damage to the nearby infrastructures and environment during the construction process. In fact, as urban tunnels are generally shallow, the field of displacements induced in the ground by the excavation propagates up to the ground level. This can be limited by implementing the appropriate engineering solutions, but not completely avoided. The prediction and monitoring of ground movements is thus a critical issue to assess potential damage and to undertake preventative measures

(Burland and Wroth 1975, Boscardin and Cording 1989). The excavation of a tunnel in urban areas can affect buildings in multiple ways, depending on the excavation technique, depth and length of excavation, ground conditions, as well as many other factors. Considering the relatively high number of buildings potentially affected by the excavation in urban areas, it is often impossible to monitor them all with traditional monitoring techniques, owing to the prohibitive cost. Therefore, often only those buildings or infrastructures that have cultural, historical, and public relevance are monitored, or those that have been a priori identified as vulnerable according to the results of empirical or numerical methods.

A number of existing monitoring techniques could be used to monitor effects induced by tunnel excavations, primarily through measuring the progressive surface and subsurface soil settlement. These are summarised and compared in Table 2.1 that offers a comprehensive overview of diverse monitoring techniques, encompassing factors such as temporal frequency, area coverage, resolution, advantages and disadvantages.

Starting from traditional monitoring techniques, High Precision Levelling (HPL) emerges as a method of choice when there is a need to monitor vertical displacements, due to its unparalleled accuracy and straightforward data collection and processing. However, it is noteworthy that this technique yields spatially discontinuous measurements, limiting its applicability to a few points of interest. Total Station (TS), as well, is characterized by high temporal frequency, and excels in detecting both horizontal and vertical displacements with sub-millimetric precision. Nonetheless, similar to HPL, it falls short in providing continuous spatial data, presenting a challenge for applications requiring a comprehensive overview. While the latter two techniques can directly monitor surface displacements, borehole extensometer measures the change in length that takes place with time in a borehole or several boring holes, thus leading to pointwise data.

Moving on to innovative monitoring techniques, these include geophysical surveys such as seismic wave propagation and Ground Penetrating Radar (GPR) (Guan, Jiang and Gao 2013), which are highly manual and have low area coverage and resolution. GPR is a technique that uses low-power electromagnetic waves to produce high-resolution 2D images of the subsurface and can identify variations in subsurface layers, including changes in soil density and moisture content, which may be indicative of soil settlements.

The acquistion and the interpretation of GPR data requires the involvment of an expert. Terrestrial Laser Scanning (TLS) (Shen et al. 2023) distinguishes itself by employing a multitude of laser beams to rapidly scan the target object, resulting in the creation of a dense point cloud, which can then be utilized to construct highly detailed models. TLS offers high-resolution 3D clouds of surface deformations up to sub-millimetric precision, despite the complexity associated with data acquisition and processing that poses a significant drawback. Close-Range Photogrammetry (CRP) is the process of creating a 3D model representation of an object by combining several photographs taken close to each other, and can be used to detect subsidences (L. Meng, Zou and Liu 2020) with millimetric precision. As for TLS, CRP requires complex data collection and processing. Distributed fibre optic sensing (DFOS) (e.g. Brillouin optical time domain reflectometry (BOTDR)) (Guan, Jiang and Gao 2013; Inaudi 2014) is a technology that enables continuous, real-time measurements of strains along the entire length of a fibre optic cable, and is well suited to identify subsidences, especially for monitoring long linear infrastructure, such as roads or railways, as they can be laid in continuous lines. An additional advantage is that they can provide subsurface deformation measurements, which would allow the identification of a subsidence before its effects are evident at the soil surface. However, they rely on sufficient coupling at the interface between the fibre and the soil, as well as an understanding of the logged strain profile at depth. Monitoring settlements and ground deformation using fibre optic cables is a recent technique (Guan, Jiang and Gao 2013; Z. Guan 2015; Klar, Dromy and Linker 2014; C. Zhang, Zhu and Shi 2016; Inaudi 2014) that still requires further understanding and experience of soil-fibre interaction and its effect on the obtained data. Lastly, satellite-based monitoring (InSAR) (Ferretti, Monti-Guarnieri, Prati, Rocca and Massonet 2007) is a technique that uses satellite-based radar data to detect ground deformations with millimeter-scale precision over large areas, but relies on the satellite's repeat-orbit cycle for its temporal frequency, commonly 4-35 days (depending on the satellite constellation). Additionally, in case of low resolution of satellite imagery, this technique is not ideal for the identification of localised depressions.

This chapter is focused on the DFOS and InSAR techniques, providing a comprehensive exploration of their applications in the literature. The discussion unfolds pro-

Table 2.1: Conventional and innovative monitoring techniques for surface and subsurface settlement monitoring (adapted after Möller et al. 2023 and Gutiérrez et al. 2019).

Techniques	Temporal Frequency	Area Coverage	Resolution	Advantages	Disadvantages
High precision levelling	Med.	Low	Low	Most accurate measurements with simplicity of data collection and processing	Provides point data with spatially discontinuous measurements
Total station	High	Low	Low	Horizontal and vertical displacements detection with sub-millimetric precision	Provides point data with spatially discontinuous measurements
Borehole Extensometer	Low	Very Low	Low	Precise measurements of vertical subsurface movements	Provides point data due to economic and logistical limitations
Ground Penetrating Radar (GPR)	Very low	Low	Low	Can accurately retrieve information on subsurface movements	Requires and operative
Terrestrial Laser Scanning	Low	Med.	High	Provide 3D clouds of surface deformations	Complex data acquisition and processing
Close-range photogrammetry	Low	Med.	High	3D digital surface model with analysis of surface spatio-temporal changes	Complex data collection and processing
DFOS	Very High	Med.	Very High	Continuous strain measurements in long distance	Cable deformations may not necessarily correspond to ground deformations
InSAR	Low	Very High	Med.	Movements detection of huge areas with millimetric precision	Temporal and spatial resolution might be insufficient to capture subsidence

gressively, shifting from a broad overview to a detailed examination, particularly emphasizing their roles in the context of subsidence monitoring.

2.2 Review on DFOS monitoring

2.2.1 Background on DFOS technique

Distributed sensing is a technology that enables continuous, real-time measurements along the entire length of a fibre optic cable. A typical distributed fibre-optic sensing system is made of two components: an optical fibre cable and an optical fibre analyser. Unlike traditional sensors that rely on discrete sensors measuring at pre-determined points, distributed sensing utilises the optical fibre as a sensing element. The sensor is simply a standard and inexpensive telecommunications optical fibre with which strain or temperature can be measured at any given time at several thousand points over distances spanning kilometres (Kechavarzi et al. 2016), depending on the commercial optic analyser used (e.g. Neubrescope NBX-7020, Luna ODiSi 6100, Omnisens Vision Dual, etc.). An optical fibre is a cylindrical structure that transmits light along its axis and is essentially made of three parts (Figure 2.1): a core that carries the light is surrounded by cladding with a lower refractive index, the latter surrounded by a buffer coating that protect the brittle fibre. The core is usually made of pure silicon dioxide (SiO_2) and has a slightly higher refractive index compared to the cladding in order to allow the light travelling in the core to be reflected at the core-cladding interface.

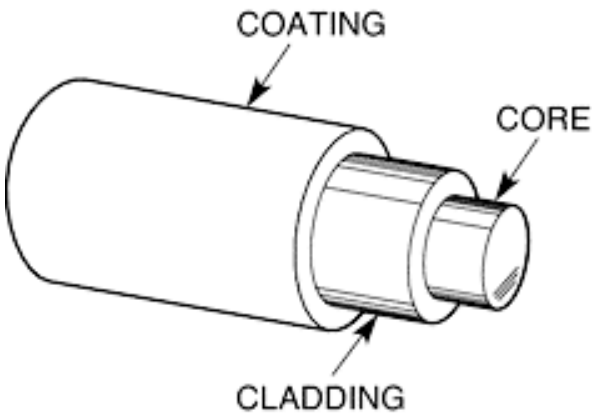


Figure 2.1: General components of a fibre optic cable: core, cladding and buffer coating.

Different types of fibre are commercially available depending on their light transport characteristics:

- stepped-index single mode: is characterized by a core with a diameter ranging from 4 to 10 μm, carefully designed to be sufficiently small compared to the wavelength of the light it carries. This ensures that the light only travel in a single path or mode. These fibres are usually used for long-distance transmission;
- stepped-index multimode: is a fibre which has a core large enough ($\geq 50\mu$m) to support a large number of potential path (modes) that light can take through the core. The core has a uniform refractive index, higher compared to the cladding. These kind of fibres suffer from modal dispersion, causing distortion of both digital and analogue signals when used for long-distance transmission;
- graded-index multimode: is a fibre which has a core made of different layers, with a refractive index that decreases with the distance from the centre. In this manner the light is refracted gradually and there is a reduction of modal dispersion.

When light travels in an optical fibre, it can either propagate in the desired direction or travel in the opposite direction after being reflected, where the latter is called backscattered light. Distributed fibre sensing technique takes advantage of this phenomena because the strain and temperature to which the fibre is subjected, influences the properties of a light signal travelling throughout the fibre. Scattering is caused by the interaction of photons with impurities or density fluctuation within the fibre's core. There are three types of light scattering (Figure 2.2):

- Rayleigh scattering: is an elastic scattering phenomenon that occurs when light interacts with inhomogeneities or imperfections in the core (i.e. microscopic variations in density or composition). Elastic scattering occurs when the frequency (or wavelength) of the transmitted light equals that of the backscattered light (Figure 2.2). Rayleigh scattering is inversely proportional to the fourth power of the wavelength of the light λ (Agrawal 2012):

$$\alpha_R = \frac{A}{\lambda^4}$$

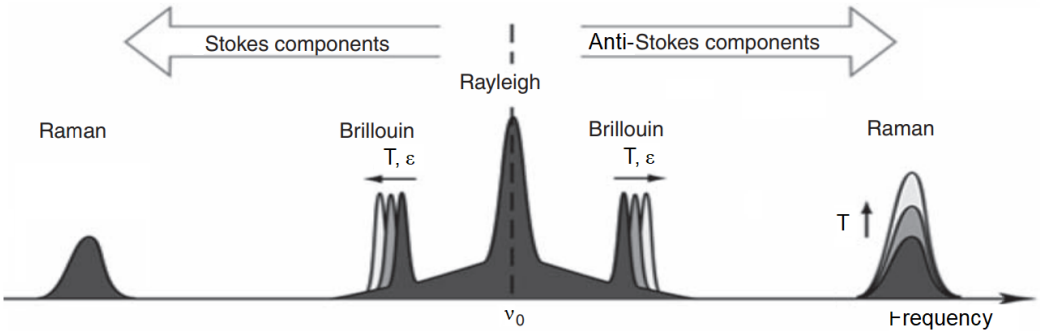


Figure 2.2: Frequencies of the backscattered light (modified afer Güemes, Fernández-López and Soller 2010).

where α_R is the intrinsic loss coefficient of the optical core due to Rayleigh scattering and A is a constant factor ($A \approx 0.7 - 0.9$ dB km^{-1} µm^{-4}). As a result, shorter wavelengths (e.g., blue light) are scattered more than longer wavelengths (e.g., red light). This scattering contributes to signal attenuation and limits the transmission distance of signals in optical fibres. Indeed, fibre optic analyser based on this scatter phenomenon can only provide useful information on a short section of the fibre optic cable (e.g. the first 20-50 meters).

- Brillouin scattering: is a non-linear scattering process with a shift in frequency (or wavelength) between the pulse and the light scattered. This shift is in the order of 23-33 mm (i.e. 13-9 GHz) and is sensitive to mechanical and thermal induced strains. Therefore Brillouin scattering lead to the generation of new frequencies (or wavelengths) (Stokes and anti-Stokes) in the scattered light (Figure 2.2).

- Raman scattering: is a non-linear scattering process that occurs when photons interact with molecular vibrations in the fibre. The frequency (or wavelength) shift is in the order of 30 μm (i.e. 10 THz), and is sensitive only to thermal induced strains.

The frequency (or wavelength) shift is acquired using a fibre optic analyser, which determines the sampling frequency and the spatial resolution along the fibre optic cable, as well as the accuracy. A few types of analysers are reported in Table 2.2, the first of which has been used for this thesis.

DFOS systems are categorized by the way of finding the location of vibration,

Table 2.2: Fibre optic analysers (Kechavarzi et al. 2016).

Name	Type	Strain Range [$\mu\epsilon$]	Strain Resolution [$\mu\epsilon$]	Strain Accuracy [$\mu\epsilon$]	Distance Range [m]	Spatial Resolution [m]	Frequency [sec]
Luna ODiSI 6100, 1-8 Standard Length sensor	Rayleigh	$\pm 12,000$	1	Min ± 30 Max ± 25	10	Min 0.00065 Max 0.0026	Min 0.04 Max 0.004
NeubreScope NBX-7020	Brillouin	$\pm 30,000$	N/A	N/A	25×10^3	Min 0.02 Max 2	Min 300 Max 5
NeubreScope NBX-6065S	Brillouin	N/A	± 40	N/A	70×10^3	Min 0.1 Max 50	N/A
Omnisens Vision Dual	Brillouin	$\pm 50,000$	Min ± 40 Max ± 2	N/A	60×10^3	Min 1 Max 5	Min 900 Max 60

strain, or temperature information. Optical Time Domain Reflectometry (OTDR) is a diagnostic tool used in optical fibre communication systems that employs short pulses of light of known width to analyze reflections along the fibre, providing insights into the location and nature of anomalies or faults. Optical Time Domain Analysis (OTDA) delves into the temporal evolution of light signals within optical fibres, offering a detailed study of how these signals change over time. Optical Frequency Domain Reflectometry (OFDR) focuses on different frequencies of light to assess variations caused by external factors such as strain or temperature along the fibre. A continuous laser source is swept in frequency domain over a period of time, where the spectrum is spatially related to amplitude and phase of the scattered light. Finally, Optical Coherence Domain Reflectometry (OCDR) leverages the coherence properties of light to achieve precise distance measurements within the fibre, functioning as a high-precision mapping tool.

Applications of DFOS systems are constrained by the maximum strain that the analyzer can record or by the maximum tensile strain achievable by the fiber core, typically ranging between 1-2% (Kechavarzi et al. 2016). If attached onto a surface, fiber optics can detect both tensile and compressive strain, whereas in the general scenario, they can only detect tensile strain, specifically in longitudinal direction. To enhance capabilities, more advanced multi-fiber optic cables are equipped with multiple glass cores, enabling strain measurement at various positions across the cable cross section. This facilitates the precise determination of the cable's spatial position. Lastly, the financial effort is governed by the fibre optic analyser which accounts for 90 to 95%

of the total cost, ranging from twenty to over one-hundred thousand euros.

Basic principles of Brillouin scattering

Distributed Fibre Optic Sensing (DFOS) based on Brillouin scattering presents a cutting-edge technology enabling continuous spatial measurements of strain and/or temperature along optical fibres attached to or embedded within structures. This technology holds the potential to replace numerous discrete sensors, offering a more efficient monitoring solution. Strain or temperature measurement are made continuously along a single cable, connected to a fibre optic analyser. This approach not only simplifies the installation of the monitoring system but also facilitates measurements over kilometers using one single sensor. Moreover, fibre optics, by their nature, are passive and immune to electromagnetic interference, chemical agents, water and corrosion resilience.

The Brillouin Optical Time Domain Reflectometry (OTDR) and Optical Time Domain Analysis (OTDA) techniques are based on the principle that when light travels within an optical fibre, a fraction of it is backscattered owing to slight variations in refractive index or density. Brillouin scattering originates from the interaction of light with propagating density waves or acoustic photons. The frequency of the Brillouin peak, denoted as ν_b, is directly proportional to the local thermodynamic properties of the material, including the acoustic velocity (v_a) and refractive index (n). Both of these parameters are function of the local temperature and strain:

$$\nu_b = \frac{2 \cdot n \cdot v_a}{\lambda} \tag{2.1}$$

where λ is the wavelength of the incident light. The Brillouin frequency is shifted by about 9-13 GHz from the incident light wave frequency at a wavelength of 1550 nm. This is called the reference Brillouin frequency ν_{b0}. This Brillouin frequency shifts linearly with changes in longitudinal strain and temperature in the fibre core/cladding so that (Kechavarzi et al. 2016):

$$\Delta\nu_b = C_\varepsilon \cdot \Delta\varepsilon + C_T \cdot \Delta T \tag{2.2}$$

where $\Delta\nu_b$ is the change in Brillouin frequency due to a simultaneous change in strain $\Delta\varepsilon$, and in temperature ΔT. The coefficients C_ε and C_T are referred to as the strain and the temperature coefficients of the Brillouin frequency shift, respectively. These coefficients depend on the properties of the optical fibre only and not on the type of cable. Hence, C_ε and C_T will vary slightly at around values of 500 MHz/% and 1 MHz/°C, respectively, for standard telecommunication single mode fibres and at the operating wavelength of 1550 nm as used with Brillouin OTDR and OTDA. For a given fibre, C_ε can be determined by calibrating strain cables in strain rigs equipped with accurate linear actuators. The evaluation of the frequency ν_b allows the calculation of strain along the optical fibre. The distance z from the point where the laser pulse is emitted to the location where scattered light is generated can be computed using the following equation (Ohno et al. 2001):

$$z = \frac{c \cdot \Delta t}{2 \cdot n} \tag{2.3}$$

where c is the speed of light in vacuum, Δt is the is the time interval between launching the pulsed light and receiving the light scattered at a given position along the optical fibre and n is the refractive index. Hence the strain distribution along the optical fibre can be obtained through a time-domain analysis by measuring the propagation times of the light pulse traveling in the fibre (Soga et al. 2018).

Basic principles of Rayleigh scattering

Rayleigh backscattering is a phenomenon in which light waves or electromagnetic signals encounter particles or scatterers significantly smaller than the wavelength of the incident radiation. Named after Lord Rayleigh, this type of scattering is characterized by its elastic nature, meaning there is no change in the frequency (or wavelength) of the scattered radiation. So differently from Brillouin scattering, where strain and temperature were related to a shift in frequency, in Rayleigh scattering the latters are related to the intensity variation of the backscattered light within the fibre optic core. The backscattered intensity of the received light is a function, among various physical parameters, of the refractive index, which is affected by temperature and strain changes.

In practical applications, where both strain and temperature may vary simultaneously, a comprehensive analysis is necessary.

2.2.2 General applications of DFOS monitoring

A general overview on the uses of Distributed Fibre Optic Sensing in engineering is given in this section.

Crack monitoring for structures

Villalba and Casas 2013 investigated the use of fibre optic cables, analysed with Optical Backscatter Reflectometer (which belongs to OFDR), in detecting multiple cracks in a full scale simply supported concrete slab (5.60 m spam length, 1.60 m width and 0.285 m thickness). The slab was monitored with OBR sensors at the top and bottom surfaces, in the four stretches. The optical fibre used was a single-mode fibre (SMF) type with a 50 m length, but no information was given on the spatial resolution. A coating of a polymer (polyimide) was used to protect the fibre against scratches and environmental attacks. Throughout the test, data measured with optical fibres revealed strain concentrations attributed to cracks, even at low load levels, across multiple locations. Visual inspection independently confirmed the positions of the cracks, aligning with the detections made by the analyser.

Meng, Ansari and Feng 2015, focused their attention on the width of the Brillouin Gain Spectrum to detect and monitor surface micro-cracks in an aluminum plate using Brillouin OTDA (Neubrex NBX-6055). Before experimental validation, a theoretical analysis was conducted to assess the viability of the proposed method for micro-crack detection and monitoring. This involved simulating strain within an optical fibre segment traversing a crack. Experimental strain measurements were found to be lower than numerically simulated values. Nonetheless, the BOTDA technique accurately identified the strain peak, indicating the crack's position. The study specifically addressed the growth of a single crack, leaving room for further exploration into the impact of multiple cracks on the resolution of crack detection and monitoring.

Davis, Hoult and Scott 2017, investigated the use of distributed fibre optic strain sensors to assess the impact of corrosion on reinforced concrete beam behavior. Six

beams, featuring varying levels of corrosion, were instrumented with fibre optic sensors and subjected to three-point bending tests. Nylon and polyimide coated fibres were applied along the top and bottom longitudinal reinforcement using a cyanoacrylate adhesive (Loctite 4851). LUNA OBR4600, which analysed Rayleigh backscatter from a standard single-mode fibre cable to measure strain and temperature, was used throughout the tests. Four of the six beams underwent corrosion through an accelerated corrosion technique, while the remaining two were tested without corrosion. Throughout the tests, the fibre optic cables demonstrated the capability to detect changes in strain within the longitudinal reinforcement, attributable to the loss of bond between the concrete and reinforcement induced by corrosion.

Bridge monitoring

Enckell et al. 2011 used stimulated Brillouin scattering in optical fibres for temperature and mechanical strain sensing aid at monitoring cracks development on the existing Gotaalv Bridge (Gothenburg, Sweden). Polyimide-coated optical fibre was bonded to the structured by embedding it in a thermoplastic tape in the similar manner as the reinforcing fibres are integrated in composite materials, to improve the strain transfer. Some typical, selected I-beams of the bridge were installed with sensors, meanwhile four steel beams were prepared and installed with sensors in the same manner as in reality on the bridge to simulate on-site conditions. Test results on these steel beams demonstrated the ability to detect cracks with a minimum width of approximately 0.5 mm. Additionally, different crack opening behaviors were tested: 1) a fast crack opening of 0.3 mm without delamination was properly detected; 2) a fast crack openings of 1.6 and 3.3 mm with delamination was detected as well; 3) slow crack opening of 0.6 mm in 12 minutes with no delamination, was undetected. For this reason, to establish redundancy and enhance reliability, more tests should be conducted, particularly with a crack detection system to gather statistical data. Additionally, a comparative analysis of different distributed sensory systems is essential to identify optimal procedures for further development.

J. Xu et al. 2016 used Brillouin OTDR and high-resolution Brillouin Differential Pulse with Pair (DPP) OTDR to gain strain distributions along the whole length of

the Haicang Bridge, which is a symmetrical highway suspension bridge with a total length of 1108 m, located in Xiamen, China. Temperature compensation was achieved using a Raman distributed temperature sensing system. A single mode optical fibre with total length of 3000 m was installed at the bottom of the steel box-girder (i.e. the bridge cross section) for the load test. The latter involved the use of 24 trucks, each weighing 300 kN, placed symmetrically in the mid section of the bridge. The initial strain distribution with no vehicle load was measured to have a baseline for subsequent strain measurements. Results after the test showed a symmetrical stain distribution, thus confirming the symmetrical design assumption of the Haicang Bridge.

Webb et al. 2017 used Brillouin OTDR technique to retrieve temperature and mechanical strain from a fibre optic cable installed within six prestressed concrete beams, belonging to the Nine Wells Bridge (Cambridgeshire, U.K.). Fibre optic cables were applied along the top and bottom longitudinal reinforcements. Optical fibres suspended in a gel, which prevented shear transfer between the concrete and the sensing core, were used in order to compensate for temperature induced strains. The main finding indicated that the low-cost fibre-optic cables used led to gradual loss of monitoring capability over time. Nevertheless, it was possible to assess strain induced by creep and shrinkage, which agreed reasonably well with the model proposed in literature.

Pile monitoring

Klar, Bennett et al. 2006 presented two case studies pertaining the use of DFOS as monitoring solution for piles: a load test aiming to establish the load transfer function, and changes in pile-soil interface stress due to nearby tunnelling. The first case pertain the use of a 0.9 mm fibre optic cable analysed with Brillouin OTDR, attached to the reinforcement of a minipile (0.14 m in diameter), needed to improve the existing foundation of a building located in Chattenden, United Kingdom. During the loading, results from fibre optic were compared with data from four strain gauges as well as from theoretical analysis, showing a good agreement. For the second case study, a 25 m in length and 1.2 m in diameter reinforced concrete pile was monitored with a reinforced fibre optic cable, used to prevent rupture during the execution of the pile.

Strain within the cable were recorded before, during and after the execution of a tunnel in proximity of the pile (5 m far from it). An analytical solution was developed for this case as well, and monitored data well agreed with the prediction. Lastly, the authors compared the cost of different techniques for pile monitoring, underlying the benefits of having a distributed system rather than localised sensors.

De Battista, Kechavarzi and Soga 2016 studied the effect of centrally static loading on 0.9 m in diameter and 25 m in length reinforced concrete piles by means of Brillouin OTDR technique. The DFOS instrumentation consisted of two types of single-mode fibre optic cables installed in parallel within the piles, one for temperature and mechanical strain reading and the second for temperature compensation. By measuring the change in strain along a test pile it is possible to estimate pile-soil interface properties and infer site-specific and technology-specific load-transfer curves to be adopted for design. During the tests data from fibre optic cables were in good agreement with the readings taken from retrievable extensometers placed at five levels within the piles. Lastly, whereas traditional sensors can only provide point readings at a small number of locations along a pile, DFOS system is able to measure the complete temperature and strain profiles along the whole pile.

In their study, *Bersan et al. 2018* presented research focused on strain measurements obtained from a distributed sensor installed in a continuous flight auger (CFA) pile during a static load test. The pile, measuring 22 meters in length and 0.64 meters in diameter, was monitored using optical frequency domain reflectometry (OFDR), offering a spatial resolution of 10 mm. To enhance the shear transfer mechanism between the cable and the concrete, a specially designed 3.2 mm diameter fibre optic cable (Brugg BRUsens V9) was utilized. The authors introduced a method for utilising strain measurements to determine resistance-displacement curves for both the pile shaft and pile tip. A notable challenge addressed in the study was the need for knowledge about the effective area of the concrete cross-section along the entire pile. Such information would have proven valuable in distinguishing between strain variations induced by changes in cross-sections and those caused by friction at the pile-soil interface.

Tunnel monitoring

C. Gue et al. 2014 explored the impact of a new Crossrail tunnel excavation at London Liverpool Street Station on the cast iron linings of the existing Royal Mail Tunnel situated above the new excavation (London, U.K.). To gather data, they employed Brillouin OTDR with fibre optics installed along the cast iron lining of the pre-existing tunnel. As the fibre was specifically placed on the inner side of the lining, it was not possible to retrieve information about the stress state within the lining. Despite this limitation, the fibre optic cables effectively identified changes in strain caused by both the pilot and the enlargement excavation, thus indicating the transversal and longitudinal deformation mechanisms.

Di Murro et al. 2016 introduced an innovative approach by incorporating fibre optic monitoring using the Brillouin OTDA technique to oversee the main tunnel at the Centre for European Nuclear Research (CERN). They opted for DFOS due to its resilience to radiation, making it suitable for challenging environments like CERN where various radiation sources may disrupt other instruments. Notably, the cable was not directly attached onto the surface of a tunnel ring. Instead, a system of hooks and pulleys was employed for installation along the ring, providing pre-strain to accommodate compressive strain without cable buckling. The strain profile obtained during readings revealed that the lateral sides of the tunnel experienced more significant strain values compared to those at the crown. This behavior aligned with a load pattern characteristic of over-consolidated soil environments.

Moritz et al. 2021 provided three applications case of railway tunnel pre-cast concrete lining monitoring instrumented with fibre optic cables (namely the Koralm Tunnel, the Granitztal Tunnel and the Semmering Base Tunnel, Austria). Strains were recorded starting from the installation of the lining and for long term monitoring purposes. In some cases, measurements from the fibre optic sensors were compared with results gained from distributed vibrating wire sensors, providing a good agreement. Unfortunately, no information was given on the fibre optic technology and to the installation procedures.

Minardo et al. 2021 described a monitoring system implemented in an artificial tunnel situated in the southern Italian Apennines, which crosses an active landslide zone. Using a distributed optical fiber strain sensor based on stimulated Brillouin

scattering, the study aimed to track the deformations of the tunnel structure in response to landslide movements. Since 2016, the internal deformations of the tunnel have been monitored to detect potentially dangerous strains and analyze their time trend. Results indicate that strain peaks occur at structural joints, intially concentrated around joints affected by localized landslides triggered by river erosion. Over time, the fiber experienced elongation in all joints, with failure occurring in downslope joints as well. The study correlates these findings with GPS measurements of landslide displacements and analyzes the impact of rainfall variations on the movement rates. Acceleration in landslide movements between 2018 and 2020 coincided with fiber failure, highlighting the system's reliability in monitoring strain distribution and tunnel behavior.

Slope and landslide monitoring

Sun et al. 2016 used Brillouin OTDR to retrieve strain from an ad-hoc instrumentation for landslide monitoring located in Guizhou town of Zigui in China. The slope is mainly composed of talus material and residual deposit with loose structure and strong water permeability. The instrumentation consisted of two parts, test tube made in aluminum and strain sensing fibres. Specifically, four optical fibres were installed on the surface of the test tube at four positions orthogonal to each other. This instrumentation was then installed along the landslide, mimicking the installation process of inclinometers in various boreholes. The monitoring system successfully identified two slip surfaces, and the obtained results were compared with those from traditional inclinometers, showing a satisfactory agreement between the data.

Kogure and Okuda 2018 used a similar instrumentation of that used in Sun et al. 2016, but this time only on fibre was attached to the test tube, and it was analysed with a Neubrescope NBX-7020, based on Rayleigh backscattering mechanism. The tube, whose length was 10 m, was installed in a real landslide area, and the distribution of strains was acquired during the summer and autumn seasons to measure strain changes due to rainfall precipitations. Results showed that DFOS data were clearly correlated to the rainfall precipitations.

2.2.3 DFOS for subsidence monitoring

Pioneer full-scale experiments exploring the application of fibre-optic sensors for subsidence detection in sands were conducted by *Villard and Briancon 2008*. The experimental setup involved simulating a void measuring 2 meters in width and 0.5 meters in depth using inflatable balloons. Monitoring of the subsidence process was accomplished using 9 Fibre Bragg Gratings (FBGs), spaced at 1 meter intervals, integrated into a fibre optic cable woven within a geosynthetic sheet. The primary focus of the study was the assessment of the strain developed in the geotextile during the experiment to validate a proposed analytical solution, further investigated by numerical analysis. Remarkably, the study demonstrated that the fibre-optic sensor accurately captured strain from the onset of the balloons deflation, showing a peculiar shape profile, with a central negative (i.e. compression) peak and two positive (i.e. tension) peaks on the side of the void. Furthermore, the results confirmed the accuracy of the numerical and analytical predictions showing a robust agreement between the observed data and the predicted outcomes.

A year later, *Belli et al. 2009* conducted analogous experiments, employing a 0.5 meter wide inflatable balloon. Fibre-optic strains were obtained using Brillouin scattering with a spatial resolution of 1 meter. The experimentation involved the deployment of five distinct fibre optic sensors, both independently and as part of a geogrid, to investigate their sensitivity in detecting soil settlements. The key finding of the study revealed that all sensors effectively detected and accurately localized induced settlements, but with different sensitivity. Specifically, independent fibre optic cables exhibited high sensitivity in the initial stages of the test, up to a surface settlement of 4 mm. Conversely, cables integrated into the geogrid demonstrated increased sensitivity for higher surface settlements, exceeding 10 mm. This observation suggested an enhanced interaction between the integrated sensors and soil for settlements larger than 10 mm.

Lanticq et al. 2009 performed a full-scale test, simulating the formation of two voids 2.1 meters wide and 2 meters deep, sufficiently spaced to avoid interference. A cable 2 mm in diameter containing eight optical fibres was analysed with Brillouin optical time-domain reflectometry (BOTDR) and optical frequency-domain reflectometry (OFDR), to study the efficacy of both technologies in detecting soil strains. The sensor

was buried into a continuous line at two distinct depths (0.5 and 1.25 meters below the surface) and three different offsets from the void center (0, 0.75, and 1.25 meters). This arrangement facilitated an exploration of the monitoring solution's sensitivity in different positions. Additionally, finite-element numerical analysis (FEA) was performed to validate results at small cavity displacements (i.e. 5 mm). Notably, the outcomes were consistent with the monitored data, revealing that, owing to its higher spatial resolution, OFDR technology was to be preferred. It is worth noting that strain data from the most offset cable proved to be useless, given its distance from the cavity. This observation underscored that this technology is most effective in detecting subsidence when deployed in close proximity.

Blairon et al. 2011 obtained comparable findings through a full-scale test, simulating the creation of two voids measuring 1 meter in width and 1.5 meters in depth. The first embankment comprised pure sand, while the second was composed of sandy clay, allowing for an examination of how soil properties influenced sensor sensitivity. The study involved the analysis of eight distinct manufactured fibre optic cables, employing Brillouin OTDR, Rayleigh OFDR, and a Raman analyser for temperature compensation. These cables were installed at depths of 0.5 and 1 meter from the soil surface. The key finding highlighted that all sensors successfully detected changes in strain within the ground for a void displacement of 4 mm. However, the optical frequency-domain reflectometry (OFDR) technology emerged as the preferred choice owing to its superior spatial resolution. Furthermore, it was observed that the maximum induced strain was more pronounced in a less cohesive soil, adding another insight into the relationship between soil composition and sensor response.

In their study *Buchoud et al. 2015*, the researchers moved a step forward in the processing of Distributed Fiber Optic Sensing (DFOS) data by introducing a methodology for estimating maximum soil settlement at depth resulting from void formation. The approach begins with an examination of settlement profiles at depth caused by void formation, utilizing well established empirical relations in tunneling excavations. Subsequently, the study explored the strain transfer mechanism between the external structure of the cable and the fiber optic core. To validate their methodology, the authors conducted small-scale trapdoor tests to simulate void formation. Both Brillouin

OTDR and Rayleigh OCDR techniques were employed to extract information from the cable. The application of this methodology allowed the authors to predict the maximum settlement in the soil body. Remarkably, the obtained values aligned well with those from traditional load displacement sensors located in close proximity to the fiber optic cables.

In field tests, two studies (*Linker and Klar 2017* and *X. Xu, Kechavarzi et al. 2022*) implemented buried fiber optic cables in trenches for sinkhole detection and monitoring. In the first study, a single fiber optic cable, analyzed by both Brillouin OTDR and OTDA, was buried in the Neger Desert, south of Israel, to detect sinkhole formation. To understand the expected signal strain profile, a Finite Element numerical analysis, accompanied by a theoretical analysis based on the method proposed by Sagaseta 1987, was conducted. This approach focused solely on subsidence detection, and the proposed method demonstrated a high detection rate when applied in situ. In contrast, the second study utilized fiber optic woven into geotextile, analysed by Brillouin OTDR, over a 3-meter-wide simulated void. The results highlighted the technology's sensitivity in detecting strain changes within the soil as the void began to form. This dual approach to sinkhole detection showcases the versatility and effectiveness of fiber optic monitoring in different scenarios.

2.3 Review on InSAR monitoring

2.3.1 Overview of SAR satellites for InSAR applications

Satellite Interferometric Synthetic Aperture Radar (InSAR) is a recent technology in remote sensing, offering an unparalleled ability to monitor ground deformation globally with millimetric precision (Ferretti, Prati and Rocca 2001). At its core, InSAR exploits the capabilities of Synthetic Aperture Radar (SAR), a remote sensing technique that employs radar signals to generate high-resolution images of Earth's surface. Satellites SAR systems operate with active microwave radar signals so that they can acquire images independently of weather conditions and illumination, making it a powerful tool for capturing surface changes.

The roots of SAR trace back to the mid 20^{th} century when researchers explored the

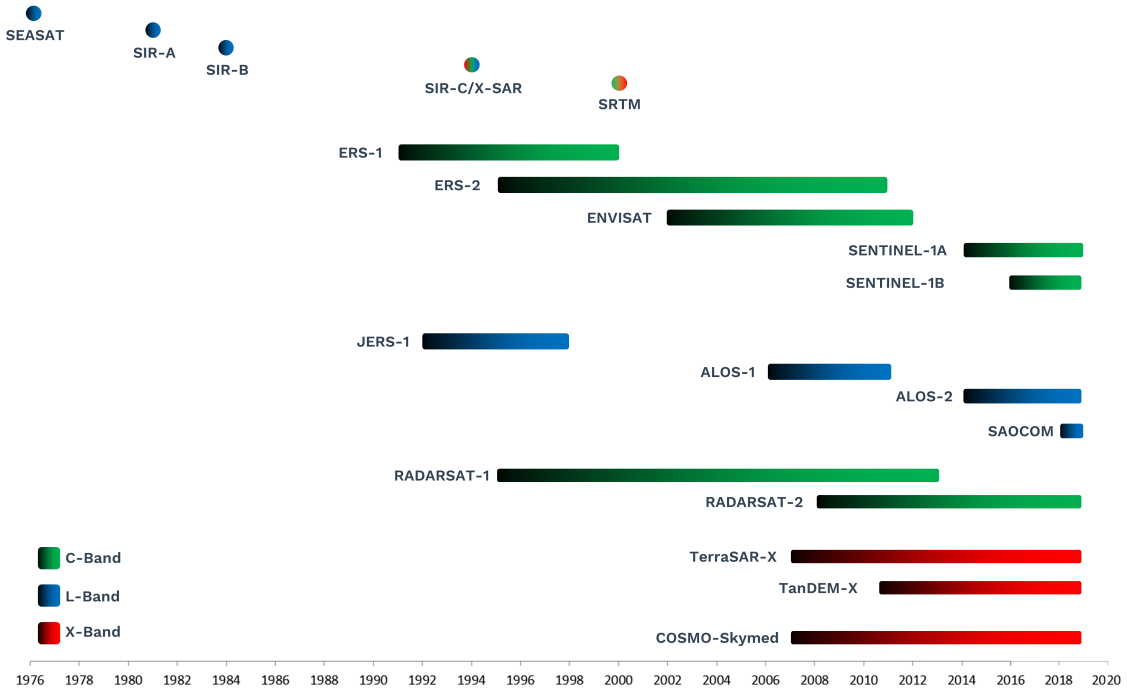


Figure 2.3: Historic and recent radar satellite missions. Figure downloaded from EO College - 2023.

potential of radar for Earth observation. The concept of SAR emerged as a means to enhance the resolution of radar images by synthesizing a larger aperture through the movement of the radar platform. Early experiments with airborne SAR systems laid the foundation for spaceborne SAR missions, ultimately culminating in the launch of SAR-equipped satellites.

Starting with SeaSat in the late 1970's, numerous missions contributed to a vast range of data, improving environmental and Earth system sciences. Since the 1990's and 2000's, very successful satellite missions were launched, for example ERS 1 and 2, ENVISAT and ALOS provided large amounts of data to scientists, commercial users and public authorities. A general overview of satellite missions involving the use of SAR is reported in Figure 2.3.

SeaSat, launched in 1978, marked NASA's (National Areonautics and Space Administration) pioneering Earth observation experimental mission, featuring the first-ever civilian spaceborne Synthetic Aperture Radar (SAR) instrument. Despite its brief 110-day lifetime, cut short due to a malfunction, SeaSat made a significant impact by collecting more oceanographic information than the previous century of shipboard re-

search. This mission played a crucial role in establishing satellite oceanography and validating the viability of imaging radar for Earth observation (ESA 2012c).

In the aftermath of SeaSat, NASA-JPL (Jet Propulsion Laboratory) initiated four SAR technology demonstration missions in the early 1980s and early 1990s, collectively known as the Shuttle Imaging Radar (SIR) missions. These included SIR-A (1981), SIR-B (1984), and two SIR-C/X-SAR missions in 1994. Inspired by the success of SeaSat's L-band SAR mission, these missions leveraged the Shuttle platform for short missions, enabling the progressive development and reuse of radar systems. The SIR-A payload featured an L-band SAR instrument with HH polarization, a fixed antenna look angle of $\theta = 47°$, and a resolution of 40×40 meters (ESA 2012d).

Moving into the European perspective, the European Space Agency (ESA) launched the ERS-1 (European Remote-Sensing Satellite-1) in 1991, marking its first program in Earth observation. ERS-1 aimed to provide environmental monitoring, particularly in the microwave spectrum, enabling regular monitoring of land-surface and ocean-surface processes for change detection. ERS-1's SAR instrumentation operated in C-Band, offering a spatial resolution ranging from 10 to 30 meters, with a fixed antenna look angle of $\theta = 23°$. The success of ERS-1 led to the continuation of the program with ERS-2, launched in 1995, incorporating several enhancements (ESA 2012b). In 2002 ESA launched EnviSat, which carried an Advanced Synthetic Aperture Radar (ASAR) with and improved resolution of 28×28 meters.

The Shuttle Radar Topography Mission (SRTM), a joint international project involving NASA, DoD/NGA (National Geospatial-Intelligence Agency), DLR (German Aerospace Center), and ASI (Italian Space Agency), represents one of the most significant mapping surveys from space. Launched aboard the Shuttle, SRTM aimed to provide high-resolution topographic data for our planet (ESA 2012e).

In the realm of the Copernicus satellite family, the Sentinel-1 mission stands out as the European Radar Observatory. Developed by ESA and funded by the European Commission, Sentinel-1 comprises a constellation of two satellites, Sentinel-1A and Sentinel-1B, launched in 2014 and 2016 respectively. Positioned with a 180° orbital phasing difference, these satellites offer an independent operational capability for continuous radar mapping of the Earth. The mission provides enhanced revisit frequency,

coverage, and reliability for operational services and applications requiring long time series. The C-Band SAR system on Sentinel-1 can acquire data with a spatial resolution ranging from 25×100 meters to 5×5 meters in dual polarization (HH+HV or VV+VH) depending on the operational mode (ESA 2023).

Moving on with the most recent satellites, TerraSAR-X1 (also referred to as TSX or TSX-1) is a German SAR satellite mission for scientific and commercial applications (national project). The project is supported by BMBF (German Ministry of Education and Science) and managed by DLR (German Aerospace Center). TerraSAR-X is equipped with an X-band SAR instrument, which allows for high-resolution imaging of the Earth's surface, up to 1×1 meter, in multiple polarization. The X-band frequency (around 3 cm wavelength) provides fine spatial resolution and is suitable for a variety of applications (ESA 2012f).

Lastly, COSMO-SkyMed (Constellation of Small Satellites for Mediterranean basin Observation) is a 4-spacecraft constellation, conceived by ASI (Italian Space Agency), and funded by the Italian Ministry of Research (MUR) and the Italian Ministry of Defense, Rome, Italy. The program is managed in cooperation of ASI and MoD. Each of the four satellites is equipped with a SAR (Synthetic Aperture Radar) instrument and is capable of operating in all visibility conditions at high resolution and in real time. The overall objective of this program is global Earth observation and the relevant data exploitation for the needs of the military community as well as for the civil (institutional, commercial) community (ESA 2012a).

2.3.2 A review of InSAR techniques

SAR interferometry is a technique that exploits the phase difference between two acquisitions to extract valuable information about topography and surface displacements within a specific area. The main output provides scalar data, which is the displacement component along the satellite line of sight of the three-dimensional displacement, and that data on ascending and descending orbital passage are needed in order to estimate the vertical and East-West (E-W) horizontal displacements. When the focus is on topography, the technique is precisely termed InSAR (Interferometric Synthetic Aperture Radar). The primary outcome of InSAR is the generation of a Digital Elevation Model

(DEM) which provide detailed elevation information of the area of interest. To optimize the accuracy of InSAR, acquisitions are ideally generated from two different viewing geometries, preferably within the same timeframe. This helps mitigate decorrelation effects caused by atmospheric conditions and changes in the area of interest (refer to Section 3.2.3 for more details). On the other hand, when the objective is to capture information about displacements occurring within the area of interest, the technique shifts to Differential InSAR. However, a challenge arises due to variations in atmospheric conditions during the different acquisitions in time, leading to a phase gap in the output. This phase gap can be erroneously associated with displacements, introducing limitations to the application of Differential InSAR.

To avoid this limitation, in the early 2000 scientists developed more robust techniques which were able to mitigate the effect of phase decorrelation and improve the precision. Persistent Scatterers Interferometry (PSI) represents a specific class of DInSAR techniques, which exploits multiple SAR images acquired over the same area, and appropriate data processing and analysis procedures to evaluate the displacements of targets in time, minimising the effect of atmospheric artifacts. The term PSI is used in this work to indicate a number of different techniques including the Permanent Scatterers approach developed by Ferretti, Prati and Rocca 2001, the Small Baseline Subset approach (SBAS) developed by Berardino et al. 2002 and many others present in literature. An overview of different PSI approach is reported in Table 2.3, which is taken from Crosetto, Monserrat et al. 2016.

The distinguishing factor among these approaches lies in the method employed to link SAR images for interferogram generation. Take, for instance, the single master approach where a designated SAR image, termed the Master image, is connected to other images referred to as Slave images. In this scenario, interferograms are formed by pairing the fixed Master image with each i^{th} Slave image. In contrast, the small baseline approach adopts a different strategy. This method involves selecting pairs of SAR images with minimal temporal intervals between them. The goal is to create a sequential chain of interferograms by connecting images that are temporally close. This approach capitalizes on the proximity in time between selected image pairs to enhance coherence and reliability in detecting ground deformation. Basically, the small baseline approach

Table 2.3: Characteristics of the main PSI approaches (Crosetto, Monserrat et al. 2016).

PSI method reference	Baseline configuration	Pixel selection criterion	Deformation model
Ferretti, Prati and Rocca 2001	Single master	Amplitude dispersion	Linear deformation in time
Berardino et al. 2002	Small baselines	Coherence	Spatial smoothness
Mora, Mallorqui and Broquetas 2003	Small baselines	Coherence	Linear deformation in time
D. A. Schmidt and Bürgmann 2003	Small baselines	Coherence	Spatial and temporal smoothness
Werner et al. 2003	Single master	Amplitude dispersion & Spectral phase diversity	Linear deformation in time
Duro et al. 2005 and Crosetto, Biescas et al. 2008	Small baselines	Amplitude dispersion, coherence, spectral coherence	Linear deformation in time
Kampes 2006	Single master	Amplitude dispersion & Signal to clutter ratio	Different types of deformation models
Hooper et al. 2004	Single master	Amplitude and phase criterion	Spatial smoothness
Crosetto, Biescas et al. 2008	Small baselines	Coherence	Stepwise linear function in time
Costantini et al. 2008	Single master	Amplitude dispersion	Linear deformation in time
López-Quiroz et al. 2009	Small baselines	Coherence	Spatial smoothness
Ferretti, Fumagalli et al. 2011	Single master after triangulation	Statistical homogeneity test	Deformation model in time
Perissin, Z. Wang and T. Wang 2011	Target-dependent interferogram subset	Quasi-PS approach	Linear deformation in time
Hetland et al. 2012	Small baselines	Coherence	Different types of deformation models
Van Leijen 2014	Single master	Amplitude dispersion	Different types of deformation models
Goel and Adam 2013	Small baselines	Statistical homogeneity test	Linear deformation in time
Lv et al. 2014	Single master	Statistical homogeneity test	Linear deformation in time
Devanthéry et al. 2014	Small baselines	Amplitude dispersion & Cousin PS	Spatial smoothness

aims to capture deformation signals over shorter time spans, mitigating the impact of temporal decorrelation. Another distinguishing factor among these approaches pertains to the selection of targets involved in interferometric analysis. Some methods rely on the amplitude of the backscattered signal to identify targets exhibiting stability over time. In these approaches, the amplitude of the radar signal from a target is a key criterion for determining its suitability as a persistent scatterer. Conversely, alternative approaches leverage the coherence of the backscattered signal for target selection. Coherence is a measure of the consistency and stability of the phase relationship between the radar signals from two acquisitions. Targets with high coherence values are considered persistent scatterers, indicating that their radar reflections remain stable over time. In essence, the choice between amplitude-based and coherence-based target selection depends on the specific characteristics of the study area and the desired outcome of the interferometric analysis. Each approach has its merits and trade-offs, and the selection criterion plays a crucial role in identifying reliable and consistent targets for monitoring ground deformation using Persistent Scatterer Interferometry (PSI).

2.3.3 Satellite InSAR for tunnelling-induced subsidence monitoring

Amelung et al. 1999 pioneered the application of Differential Interferometric Synthetic Aperture Radar (DInSAR) analysis for subsidence detection in urban areas. They focused on the city of Las Vegas, Nevada, U.S.A., investigating land subsidence resulting from groundwater extraction. The study utilized ERS satellite SAR data and involved the generation of four differential interferograms spanning from April 1992 to December 1997. To assess the accuracy of DInSAR displacements, a cross-section of 10 km across the city was chosen for comparison with leveling measurements. The results revealed a general agreement between DInSAR displacements and the ground-level measurements. However, differences found in this comparison might be attributed to atmospheric artifacts that could not be removed with DInSAR, even though the authors indicated that the arid climate of Las Vegas helped in reducing atmospherics effects.

A year later, *Ferretti, Prati and Rocca 2000* demonstrated the application of

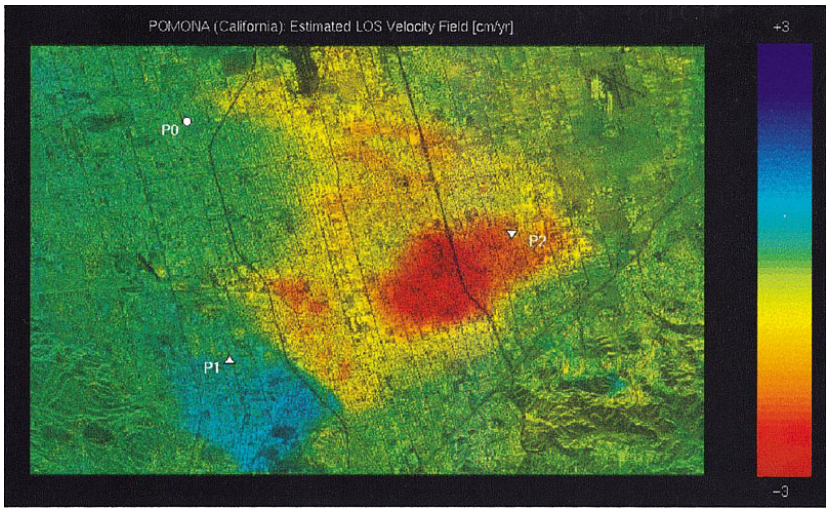


Figure 2.4: Subsidence map of Pomona City detected via PSInSAR analysis (Ferretti, Prati and Rocca 2000).

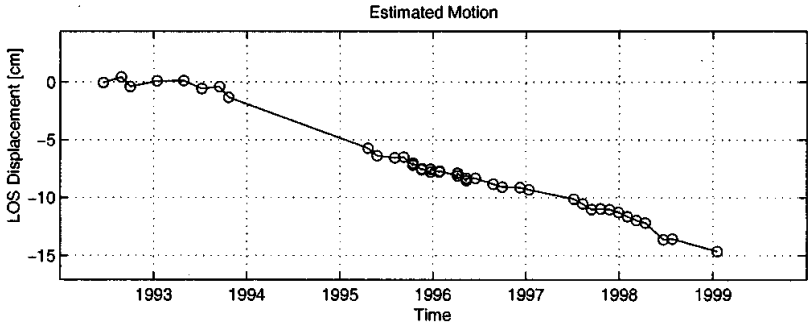


Figure 2.5: Time series relative to one scattered identified as point P2 in the subsiding area (Ferretti, Prati and Rocca 2000).

advanced InSAR algorithms, based on their previous work on the Permanent Scatterers InSAR (PSInSAR) technique (Ferretti, Prati and Rocca 2001). This technique proved highly effective in mitigating atmospheric artifacts and enhancing the accuracy of subsidence detection. Their case study focused on Pomona, California, U.S.A., with the corresponding subsidence map depicted in Figure 2.4. Notably, the PSInSAR analysis enabled the tracking of target displacements over time, a capability not achievable prior to this advanced technique. Figure 2.5 illustrates an example of scatter time series, highlighting the precision of the measurements achieved through this technique. Unfortunately, the accuracy could not be assessed as the authors did not compare the results with robust traditional monitoring methods.

In their study, *Ge et al. 2011* conducted a Persistent Scatter InSAR (PSInSAR) analysis over Beijing, China, using 12 ENVISAT SAR images. Figure 2.6 illustrates

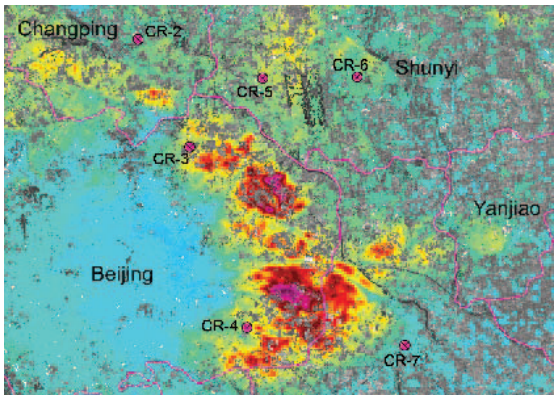


Figure 2.6: Subsidence map of Beijing area in the year of 2009, adapted from Ge et al. 2011

Table 2.4: Comparison of leveling data and PSInSAR, adapted from Ge et al. 2011

ID	Levelling [mm]	PSInSAR [mm]
CR-1	-40.52	-40.0056
CR-2	-26.52	-24.6693
CR-3	-44.52	-48.8844
CR-4	-36.39	-36.3691
CR-5	-44.97	-44.9910
CR-6	-23.17	-24.7429
CR-7	-27.57	-24.9704

the resulting subsidence map. The primary focus was on determining displacements of man-made Corner Reflectors (CR), characterized by three flat metal surfaces meeting at 90-degree angles. CRs were chosen for their consistent and stable target response in both amplitude and phase across different acquisition times (Ge et al. 2011). The comparison in Table 2.4 between leveling data and PSInSAR CR displacements revealed a significant agreement, highlighting the reliability of the PSInSAR analysis.

In *Perissin, Z. Wang and Lin 2012*, the authors used a single Master persistent scatters (PS) analysis carried out on CSK descending SAR images for the detection of surface settlements induced by Shanghai subway tunnels, in China. The velocity map of deformations clearly indicated the subway alignment 2.7. InSAR-monitored velocities were fitted with a standard Gaussian distribution along tunnel cross sections, as can be seen in Figure 2.8, and a comparison with published data in the same area confirmed the extension of the fitted settlement trough.

A similar work was carried out by *Santangelo et al. 2021*. Here, MT-InSAR is applied to the excavation of Metro Line 6 in the city of Naples, using CSK SAR images in ascending direction. The authors reconstructed the vertical displacements from InSAR-monitored data first, and then compared their time series to the traditional surveying method (precise levelling points, PLP), showing a good agreement. Furthermore, in order to analyze the spatial distribution of the settlements, the researchers applied a standard Gaussian curve to fit the InSAR and PLP data. This analysis revealed a strong correlation between the two monitoring techniques, despite the fact that only a

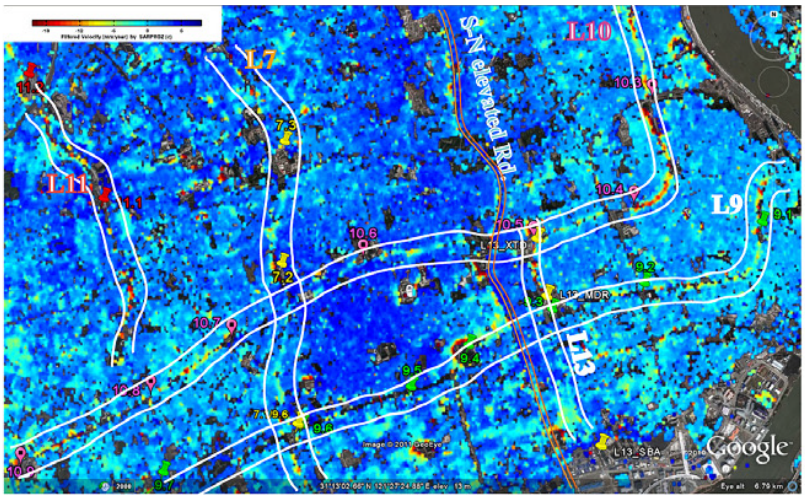
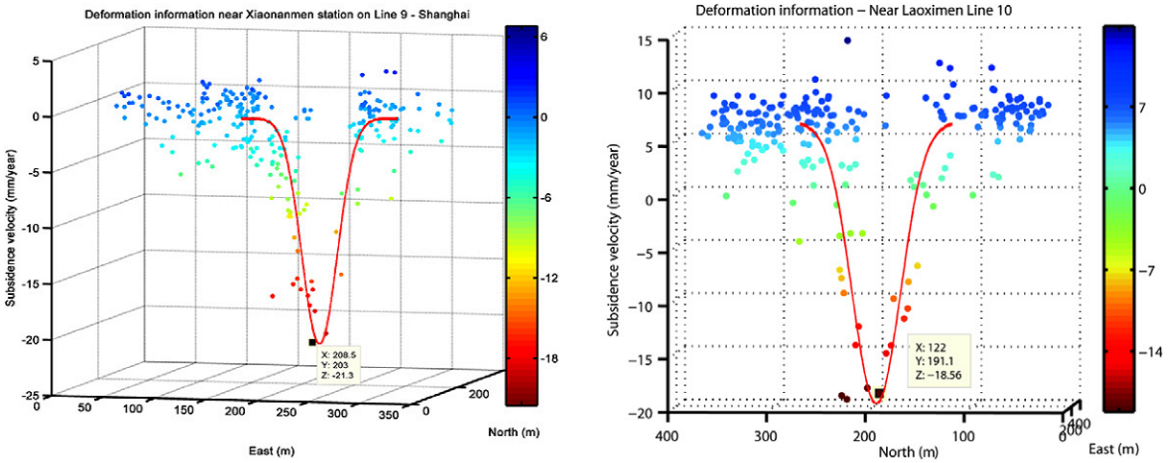


Figure 2.7: Subsidence map around Line 7, 9, 10, 11 and 14 of the Shanghai subway (Perissin, Z. Wang and Lin 2012). Note the settlements detected via PS analysis along the tunnel stretches.



(a) (b)

Figure 2.8: (a) Transverse subsidence profile near Xiaonanmen Station on Line 9 (Perissin, Z. Wang and Lin 2012). (b) Transverse subsidence profile near Laoximen Station on Line 10 (Perissin, Z. Wang and Lin 2012).

small number of scatterers was taken into account.

A different approach was used in *Barla et al. 2016*. Here, the authors carried out an MT-InSAR analysis on CSK SAR images in both the ascending and descending direction. This allowed the separation of vertical and east-west (E-W) horizontal displacement components, induced by the excavation of two motorways tunnels. However, the south-north (S-N) horizontal displacement component remained undetected. This is primarily due to the inherent limitations of the polar sun-synchronous orbit followed by the satellite, which excludes the detection of displacements aligned parallel to its path. The InSAR results agree well with the conventional survey (robotic total station and automatic GPS), confirming the trend and the magnitude of displacements, in both the vertical and E-W horizontal directions.

A collection of interesting works pertaining to the post-tunneling building damage assessment procedure with InSAR data is provided in *Milillo et al. 2018*, *Giardina et al. 2019a*, *Giardina et al. 2019b* and *Macchiarulo et al. 2021*. These latter papers focused on the Crossrail twin tunnels project in London, UK. A single Master MT-InSAR analysis was carried out on CSK descending SAR images. Standard Gaussian distribution or modified Gaussian distribution was used to fit the transverse profile of monitored settlements, in order to take into account the soil-structure interaction. From the traditional survey, an average value of volume loss $V_L = 0.7\%$, with a standard deviation of 0.3%, was observed. The average inflection point distance from the tunnel axis was $0.5 \cdot z_0$, with a standard deviation of $0.1 \cdot z_0$ (with z_0 being the tunnel axis depth). InSAR data fitting with modified Gaussian reported values of volume loss in the range 0.7-1.4% for 12 out of 14 transverse sections considered by the authors, with an average value of 1.1%. The fitted inflection point was located within $1.9 \cdot z_0$ for 12 out of 14 transverse sections, with an average value of $0.75 \cdot z_0$. In *Milillo et al. 2018*, an example of a comparison between the InSAR settlement profile and the traditional survey (PLP) is provided, showing a good agreement. In general, the authors showed how InSAR can be used to detect settlements caused by tunneling, which enabled them to assess the extent of damage to over 800 buildings in London.

2.4 Review on tunnel excavations

2.4.1 Empirical method for vertical displacements

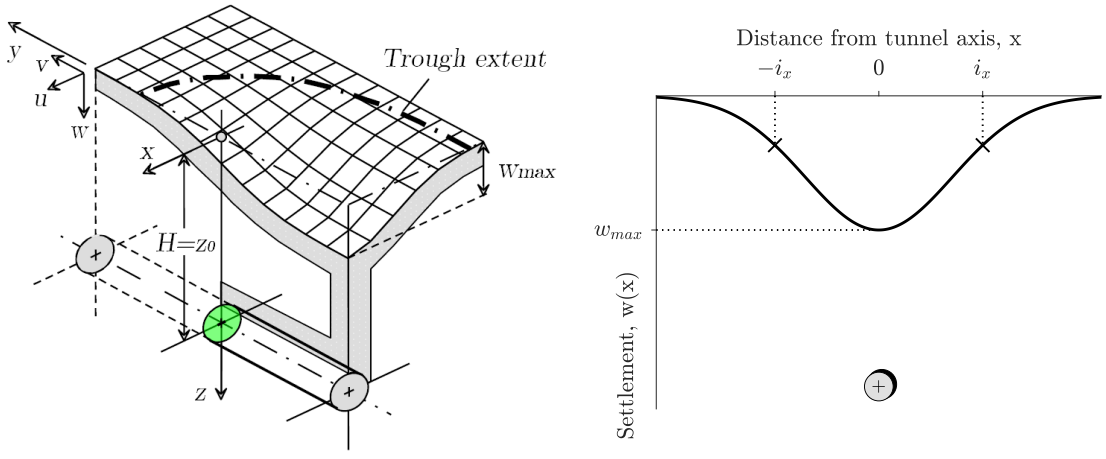
The excavation of tunnels induces a settlement trough at the surface (Figure 2.9 (a)), that can be estimated with the empirical method. The latter can be applied in case of greenfield condition, or free-field (i.e. without buildings at surface). Far from the excavation face, plane strain conditions are assumed, and the transverse section of the greenfield settlement trough is well described by a Gaussian curve as follows (Peck 1969, B. Schmidt 1969):

$$w(x) = w_{max} \cdot e^{-\frac{x^2}{2 \cdot i_x^2}} \tag{2.4}$$

where w_{max} is the maximum settlement and i_x is the distance of the inflecton point location from $x = 0$, as reported in Figure 2.9 (b) for clarification.

Integrating Equation 2.4, the volume of the settlement trough is equal to the following:

$$V_C = \sqrt{2\pi} \cdot i_x \cdot w_{max} \tag{2.5}$$



(a) (b)

Figure 2.9: (a) Settlement trough on the surface resulting from tunnel excavation, adapted from Rankin 1988. (b) Transversal settlement profile with the indication of key elements: the inflection point position denoted as i_x, the maximum settlement marked as w_{max}, and the position of the tunnel.

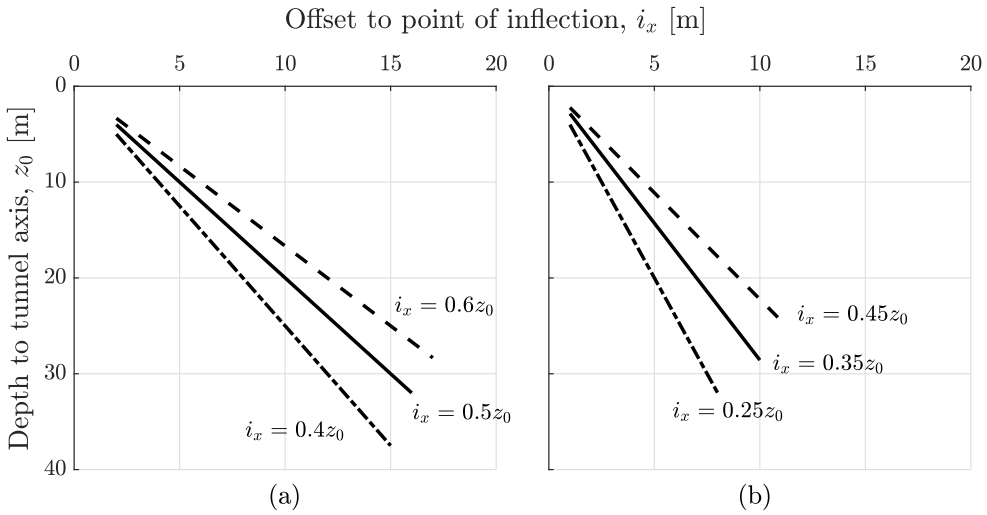


Figure 2.10: (a) Variation of inflection point location i_x with tunnel depth z_0 for tunnels in clays. (b) Variation of inflection point location i_x with tunnel depth z_0 for tunnels in sands and gravels (modified after Mair and Taylor 1997)

In general, it can be assumed that V_C is a fraction of the excavated volume per unit length of advancement and this fraction is called volume loss, V_L. Therefore, the maximum settlement can be expressed as follows:

$$w_{max} = \frac{V_C}{\sqrt{2\pi} \cdot i_x} = \frac{V_L \cdot \pi D^2/4}{i_x} = \frac{V_L \cdot \sqrt{2\pi} \cdot D^2}{8 \cdot i_x} = 0.31 \cdot \frac{V_L \cdot D^2}{i_x} \tag{2.6}$$

Thus, it is evident that a correct prediction of the settlement trough depends on a reliable estimate of the parameter V_L and i_x. In the case of mechanized excavation with a tunnel boring machine (TBM), the volume loss V_L rarely exceeds 1-1.5%, with usual values of 0.5% (Mair and Taylor 1997). For the inflection point distance i_x, it can be seen as a fraction k of the tunnel axis depth z_0 ($i_x = k \cdot z_0$) (O'Reilly and New 1982), with k ranging from 0.25 to 0.45 for sands and gravels and from 0.4 to 0.6 for silt and clay (Mair and Taylor 1997), as reported in Figure 2.10.

Therefore, substituting Equation 2.6 in Equation 2.4 leads to the following:

$$w(x) = 0.31 \cdot \frac{V_L \cdot D^2}{i_x} \cdot e^{-\frac{x^2}{2 \cdot i_x^2}} \tag{2.7}$$

In the case of twin tunnels, the superposition of the effects is often used to obtain the total ground surface settlement profile, as results of its speed and simplicity (2.11 (a) and (b)). The superposition method involves a direct combination of two settlement troughs

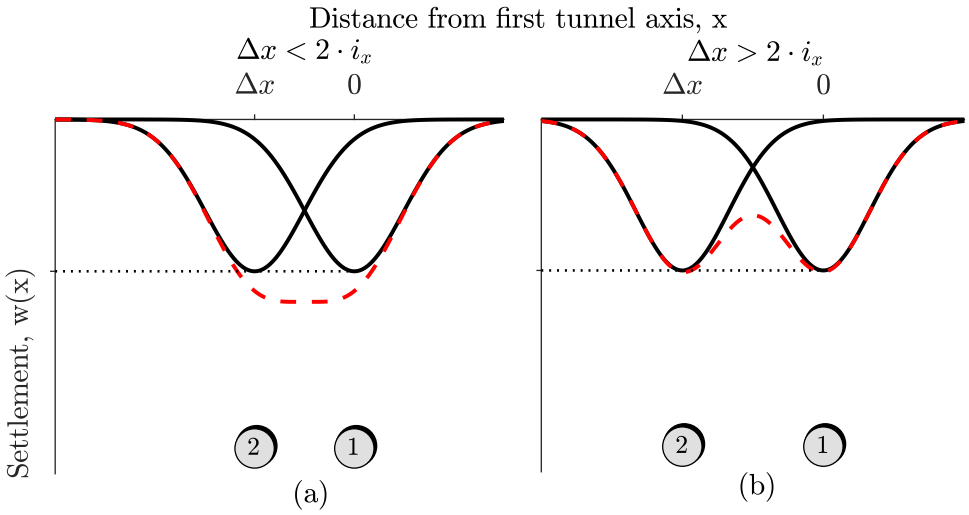


Figure 2.11: (a) Superposition of effects using Equation 2.8 when $\Delta x < 2i_x$. (b) Superposition of effects using Equation 2.8 when $\Delta x > 2i_x$. The black solid lines represent two Gaussian profiles of both tunnels (1 and 2) and the solid red line represents the superposition of effects.

induced by each single tunnel excavated in greenfield conditions, without considering any interference between the two excavations. This can result in a misestimation of the total settlement profile (O'Reilly and New 1982, Zheng et al. 2023). When superimposing the effects of the twin tunnels, it is important to consider the distance Δx between them and the interaction between the two tunnels (Suwansawat and Einstein 2007, Chehade and Shahrour 2008). The distance Δx between two tunnels determines the shape of the total settlement profile. Generally, when $\Delta x < 2 \cdot i_x$, the total settlement profile still preserves a Gaussian shape, as shown in Figure 2.11 (a).

Conversely, when $\Delta x > 2 \cdot i_x$, the total settlement profile exhibits two peaks corresponding to the tunnel axes, as shown in Figure 2.11 (b).

To obtain the total settlement profile, a single value for both the volume loss V_L and the inflection point position i_x can be used, provided that the excavation process is identical and the ground conditions are the same for both tunnels:

$$w_{tot}(x) = 0.31 \cdot \frac{V_L \cdot D^2}{i_x} \cdot \left(e^{-\frac{x^2}{2 \cdot i_x^2}} + e^{-\frac{(x+\Delta x)^2}{2 \cdot i_x^2}} \right) \tag{2.8}$$

Equation 2.8 gives a reliable estimate for the total settlement profile when tunnels are aligned side by side and their axes distance is greater than $2 \cdot D$, such that the

excavation process of the second tunnel does not influence the first one.

2.4.2 Empirical method for horizontal displacements

During the excavation of tunnels, horizontal displacements arise simultaneously with vertical displacements, with lateral movements directed toward the center of the trough. In greenfield conditions, past experience with the observational method (Cording 1975, Attewell 1978), justified the theoretical assumption that considers displacement vectors directed toward the tunnel axis (Figure 2.12 (a)), thus relating the horizontal surface movements $u_x(x)$ to vertical ones $w(x)$ (Rankin 1988, Mair and Taylor 1997), as follows:

$$u_x(x) = \frac{x}{z_0} \cdot w(x) \tag{2.9}$$

From the latter, the maximum horizontal displacement is attained for $x = i_x$, and substituting Equation 2.7 into Equation 2.9, one obtains the following:

$$u_{x,max} = 0.61 \cdot k \cdot w_{max} \tag{2.10}$$

which, for typical values of k in sandy soils or clays, leads to a maximum horizontal

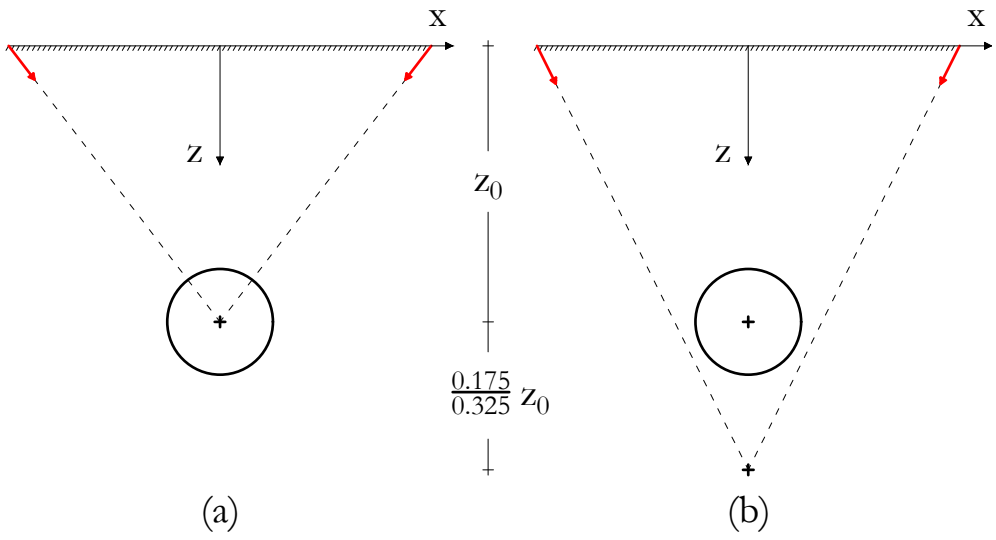


Figure 2.12: Direction of ground displacement vectors above tunnels in clays (modifed after Mair and Taylor 1997). (a) Vectors directed towards tunnel axis (Attewell 1978, O'Reilly and New 1982). (b) Vectors directed below tunnel axis (Taylor 1995).

displacement in the range of $(0.15 - 0.28)w_{wmax}$ and $(0.25 - 0.40)w_{max}$, respectively.

Based on real case measurements Taylor 1995 proposed that the vector of displacement does not point to the tunnel axis but to a point below the tunnel axis (Figure 2.12 (b)), so that the new relation between horizontal and vertical displacement is as follows:

$$u_x(x) = 0.65 \cdot \frac{x}{z_0} \cdot w(x) \tag{2.11}$$

This has the effect of reducing horizontal strains from those that would be predicted using the assumption of displacement vectors directed at the tunnel axis.

Chapter 3

Methodology

3.1 Fibre optics testing

This section builds upon the research carried out by Möller et al. 2023, who explored the potential of using Distributed Fibre Optic Sensing (DFOS) for subsidence monitoring through $1g$ trapdoor experiments. The experimental campaign conducted by the authors revealed an order of magnitude difference in strain between the soil and the fibre optic cable. This disparity, as yet unexplained, introduces a level of uncertainty in both the technology and the experimental methodology.

To address this inconsistency and enhance confidence in the findings, the methodology employed in this research involves the use of three-dimensional Finite Element Analyses (3D-FEA). This numerical approach aims to provide a deeper understanding of the observed strain discrepancy and specifically investigates the the soil-cable interface.

The phenomenon of soil arching around the trapdoor plays a pivotal role in redistributing stresses to bear the overburden load. As the trapdoor initiates movement, there is an initial sharp decrease in load on the trapdoor, reaching a minimum value. Termed the maximum arching phase, this occurs when the trapdoor displacement equals 1-2% of its width (Iglesia, Einstein and Whitman 2014, Da Silva Burke and M. Z. E. B. Elshafie 2021). The experimental findings from Möller et al. 2023 reveal that the fibre optic cables can detect a signal during this early phase of subsidence formation, exhibiting a clear signature of strain. This allows for monitoring subsidence well before any further progressive movement towards the

surface or collapse. The fibre optic data prove capable of detecting the trapdoor position and providing a conservative estimation of its width, as well as the subsidence size.

However, variations in interface conditions between the fibre optic cable and the soil lead to differences in the strains measured by the cable compared to those measured with Particle Image Velocimetry (PIV). Further experimental investigation are not possible, as PIV data correspond to sampled strain against the rig window, significantly distant from the cable located within the body of the soil sample. Additionally, the soil stresses at 1g are considerably lower than those in real world conditions, potentially influencing shear band formation and the coupling between the soil and the fibre optic cable. These complexities are explored in this thesis through FEAs to assess their relevance in potential applications to real cases.

3.1.1 Tests with DFOS cables

Experimental rig

The benchmark experimental study conducted by Möller et al. 2023 used a rectangular rig measuring $790 \times 200 \times 200$ mm. Equipped with a trapdoor of width $B = 100$ mm, this setup mimics the formation of a sinkhole within a single soil layer, as illustrated in Figure 3.1. Dry Hostun sand (Table 3.1) was employed to prepare soil samples, with a model height of $H = 200$ mm, resulting in a height to width ratio of $H/B = 2$. The study used seven models with increasing relative densities ranging from $D_R = 20\%$ to $D_R = 88\%$ (Möller et al. 2023), allowing for a comprehensive exploration of the impact of different sand conditions.

Table 3.1: Hostun sand properties (Da Silva Burke and M. Z. E. B. Elshafie 2021).

Property	Symbol	Value
Average particle size	d_{50}	0.356 mm
Minimum void ratio	e_{min}	0.555
Maximum void ratio	e_{max}	1.010
Specific gravity	G_s	2.65
Critical angle of friction	ϕ'_c	34 °

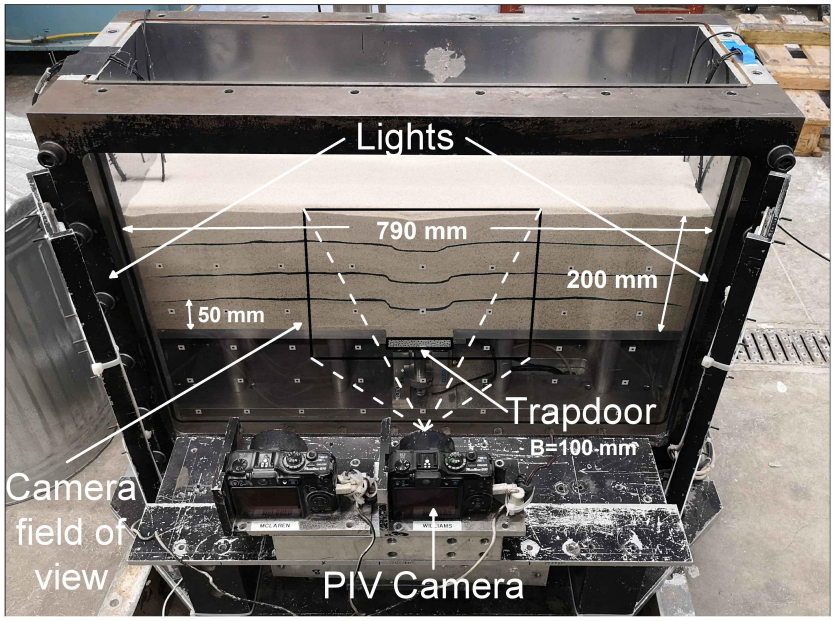


Figure 3.1: Photograph of the experimental set-up for the 1g tests.

Particle Image Velocimetry and LVDTs

Particle Image Velocimetry (PIV) stands as a widely employed technique in fluid mechanics, adept at providing a visual and quantitative understanding of fluid flow. Although not conventionally usend in geotechnical engineering, PIV can be adapted to investigate the behaviour of soils. In this method, colored particles, often referred to as tracers or seeds, are introduced into the medium. A controlled light source illuminates the portion of soil under examination, ensuring even contrast and illumination. Subsequently, a high-speed camera captures images of the illuminated soil region over a span of time. As the experiment starts, these particles come into motion, allowing for the analysis of their displacement across successive images. This displacement analysis yields valuable insights into the velocity of the soil at distinct locations within the studied area, offering a comprehensive understanding of the behaviour of the soil under investigation.

For our case scenario, the image data used for PIV analysis were captured through the use of two Canon Powershot G10 cameras. Subsequent analysis was carried out using GeoPIV RG, as detailed in Stanier et al. 2016. Simultaneously, the displacement of the trapdoor, denoted as δ, was recorded employing two linear variable differential transformers (LVDTs) positioned below the trapdoor. The LVDTs generate a differential

voltage (ΔV) corresponding to a differential displacement (Δx). Prior to usage, the LVDTs were calibrated to establish the linear correlation factor α between voltage and displacement. Once determined, the following linear relation facilitated the computation of the differential displacement from the differential voltage:

$$\Delta x = \frac{\Delta V}{\alpha} \tag{3.1}$$

The experimental setup involved the placement of two LVDTs beneath the rectangular 100 × 200 mm trapdoor, along its 200 mm side. This configuration enabled control over potential trapdoor rotation, with the rotational angle (ϑ) calculated using the following equation:

$$\vartheta = \frac{\Delta x_1 - \Delta x_2}{L} \tag{3.2}$$

Here, Δx_1 and Δx_2 represent the displacements recorded by the first and second LVDTs, respectively, while L denotes the distance between the two LVDTs.

Fibre optic cable and analyser

Fibre optic cables were strategically placed within the soil body at three nominal heights: 50, 100, and 150 mm above the trapdoor, referred to as the bottom, central, and top cables, respectively. The locations were marked using dyed black sand (Figure 3.1). In this study, a 2 mm diameter tight buffed polyurethane coated fibre optic strain sensing cable from Suzhou Nanzee Sensing Co., Ltd, was employed. This cable features a single fibre optic core (refer to Figure 3.2). Notably, it is a common single mode fibre (SMF) extensively used in fibre optic communication and structural health monitoring applications. Specifically chosen for its ability to measure axial strain and compatibility with loose materials like soil, this fibre exhibits a relatively low modulus. With a yield stress of 23.1 MPa and yield strain of 6.7%, it proves well suited for the experiments outlined in this paper. Laboratory calibration tests conducted at the Cambridge Centre for Smart Infrastructure and Construction (CSIC) have validated its effective strain transfer behavior. For instance, the strain transfer coefficient was measured at 20080 $\mu\varepsilon$/GHz using a BOTDR analyser and 6.67 $\mu\varepsilon$/GHz with a Luna OFDRODiSI 6100

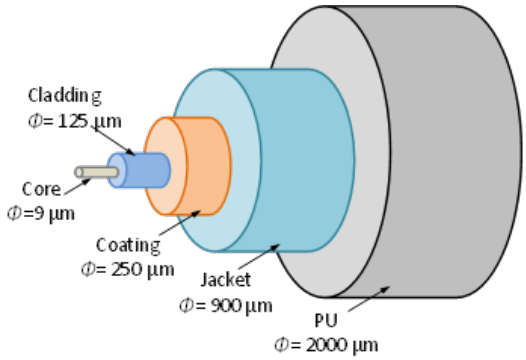


Figure 3.2: Schematic representation of experimental strain sensing cable cross section (courtesy Dr. Xiaomin Xu).

analyser. The cable's satisfactory strain transfer performance in field applications has been affirmed through previous physical model tests and field monitoring projects. To maximise soil cable interface coupling, the 2 mm cables were coated in sand, and they were pinned at the box's edge without any additional slack, allowing strain relief only up to the point of interface friction failure (X. Xu, Abadie et al. 2022). The cables were laid 60-70 mm away from the window, and therefore, are here unlikely to impact the measurement of soil deformation via PIV.

The DFOS analyser employed in this thesis is the Luna ODiSI 6100, representing one of the latest Luna Incorporation's optical distributed sensor interrogator. Table 2.2 provides a comprehensive overview of its characteristics. Functioning on the principle of acquiring and measuring Rayleigh backscattered light in optical fibres, the Luna ODiSI 6100 is particularly well suited for small scale experiments in laboratory settings, owing to its compact spatial resolution and gage length (ranging from 0.65 mm to 2.6 mm). The critical aspect lies in the number of sampling points within a specified interval length, ensuring a sufficient quantity of points to accurately measure the true strain experienced by the cable section. With a trapdoor width of B =100 mm and a gage length spanning 0.65 to 2.6 mm, this results in a range of sampling points between 154 and 38 in the fibre optic cable above the trapdoor. This configuration achieves a desirable level of discretization for capturing the strain profile effectively.

In contrast, using an alternative analyser like the NeubreScope NBX-6065S, with a gage length spanning 0.1 m to 50 m (refer to Table 2.2), would result in only one sampling point above the trapdoor. Consequently, achieving a discretization of the

Table 3.2: Centrifuge test properties at prototype scale (Da Silva Burke 2018).

Property	Symbol	Value
Trapdoor width	B	2 m
Sample height	H	4 m
Relative density	D_R	87.5%
g-level	–	40 g

strain profile above the trapdoor becomes unattainable with this setup. Furthermore, the Luna ODiSI 6100 offers flexibility in sampling frequency, ranging from 25 to 250 Hz. This variability depends on factors such as the number of fibre optic cables connected to the analyser and the Rayleigh accelerator, as detailed in the Innovations 2020. This adaptability enables the acquisition of strain data for dynamic applications, enhancing the versatility of the DFOS analysis.

Full scale validation

To enable robust scaling of the 1g test 3D FE model, a centrifuge test from the published literature was selected for validation purposes. This test was performed with the same rig as in Figure 3.1, but with a trapdoor width of 50 mm instead of 100 mm (Da Silva Burke 2018). The test was conducted at $40g$ on the centrifuge at the Schofield Centre, University of Cambridge, UK and is thus representative of a 2 m wide void, 4 m below the ground surface. Fibre optic sensing cables were not included in this test but soil deformations were monitored using PIV. The main geometrical characteristics of the test are summarised in Table 3.2.

3.1.2 Numerical model

Geometry and meshing

The experimental tests by Möller et al. 2023 were back-analysed by means of 3D FE calculations using the software platform Plaxis 3D (Brinkgreve, Engin and Swolfs 2015). The numerical model is shown in Figure 3.3, representing half the specimen, as per the symmetry at the trapdoor centre. The mesh consists of 305 000 tetrahedral elements with 425 000 nodes. The mesh is denser around the trapdoor and around the cables, where larger deformations are expected (Figure 3.3). Three dimensional analysis

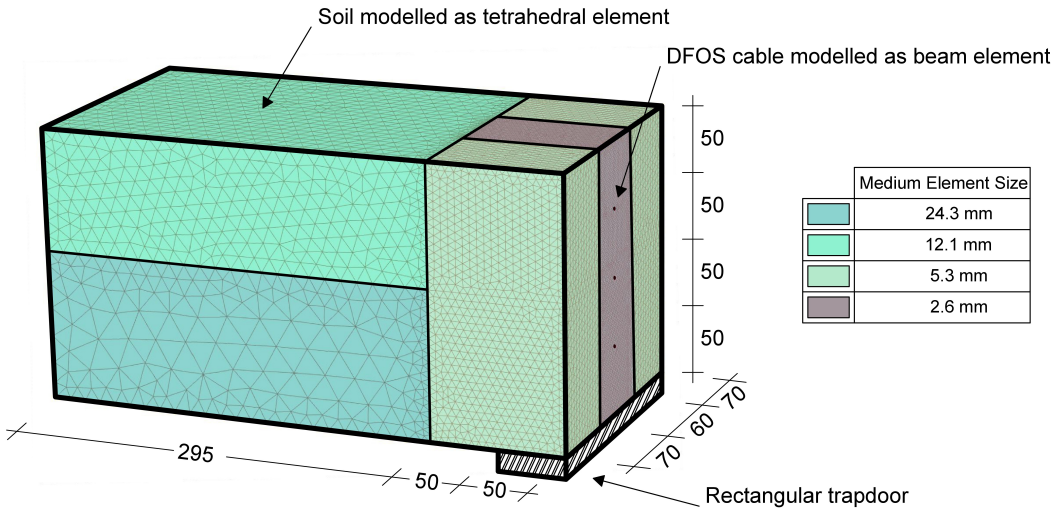


Figure 3.3: Plaxis 3D numerical model representing half of the plane-strain problem with soil modelled as tetrahedral element and fibre-optic cable modelled as an embedded beam element ($395 \times 200 \times 200mm$). Dimensions in mm.

permitted the investigation of the role of interface conditions between the soil and the cable by looking at soil stress and strain fields in proximity of the cable that could not be measured in testing.

Trapdoor tests comparing the response of fibre-optic cables to fine and coarse grained material were carried out by Blairon et al. 2011, showing that the sensitivity of the cable reduces in fine-grained materials, because maximal induced strain is larger in granular material due to arching. In addition, the experiments carried out by Möller et al. 2023 and replicated here involve a cable diameter over mean particle size (D/d_{50}) ratio of 5.6, a fairly low value at which the soil should be regarded as a granular media (Taylor 2018). Nevertheless, this limitation will not apply to cables used in the field, where D/d_{50} will typically be greater than 20 and the soil can be treated as a continuum (Taylor 2018). Hence, this limitation was ignored in the following, and the soil was considered using continuum mechanics.

The material model selected in this paper for the sand is the hardening soil model with small-strain stiffness (HSsmall) (Schanz, P. A. Vermeer and Bonnier 1999, T. Benz, Schwab and P. Vermeer 2009). It is an elastic-plastic hardening model, which accounts for soil stiffness decay with shear strain and dependence on the stress level. This model was selected because it offers a good compromise, capturing the behaviour of sands at

low confining pressure relatively accurately, while also being able to capture full-scale behaviour, providing a judicious choice of parameter values. At low confining pressures, three conditions of loose (i.e. $D_R = 20\%$), medium dense (i.e. $D_R = 52\%$) and dense sand (i.e. $D_R = 88\%$) were analysed to replicate the $1g$ tests from Möller et al. 2023. At larger stress levels (40g), a relative density of $D_R = 87.5\%$ was considered for both analyses (2D and 3D) described in this paper to compare with Da Silva Burke 2018 test results.

For the $1g$ experiment, the trapdoor tests were performed on a sand layer of rather low thickness, and the maximum average soil stress at trapdoor level (i.e. 200 mm deep) was very low and approximately equal to 2 kPa. This is a challenge for numerical modelling, as sand at such small confining stresses exhibits higher dilatancy angles and lower compressibility, which is generally ignored in constitutive models. The influence of such a low confining stress on soil dilatancy and on the shear stiffness decay is examined in the following discussion.

The dilatant behaviour is commonly described by the dilatancy angle ψ (Bolton 1986):

$$\phi'_p - \phi'_c = 0.8 \cdot \psi_{max} \tag{3.3}$$

where ϕ'_p and ϕ'_c are the effective peak angle and critical angle of shear resistance, respectively. The dependency of the dilatancy of sand on the mean effective stress p' and the relative density D_R of the soil is taken into account through the relative dilatancy index I_R (Bolton 1986):

$$I_R = D_R \cdot (Q - \ln p') - R \tag{3.4}$$

where Q and R are two fitting parameters, which are a function of the soil material (Chakraborty and Salgado 2010). These are commonly set equal to 10 and 1, respectively, to offer a unique relationship for the dilatancy behaviour of the sands considered by Bolton 1986. The difficulty in using this framework, however, is that it was originally validated against data from triaxial compression tests, and therefore even low confining stresses are commonly an order of magnitude above the confining pressure of interest in

this paper (typically > 20 kPa). Lancelot, Shahrour and Al Mahmoud 2006 performed tests on Hostun sand at relatively low confining stresses (20-50 kPa) and showed that the dilatancy angle at such low stresses is indeed stress dependent. Chakraborty and Salgado 2010 also explored low confining stresses (10-50 kPa and above) with Toyoura sand and showed that Equation 3.4 provides a reasonable fit, even at these low confining stresses, with $R = 1$ and $Q = 8$ for confining stresses ranging from 10 to 26 kPa. Decreasing the value of Q has the effect of reducing the tendency of the soil to dilate. For the numerical modelling of the $1g$ tests the aim was to replicate the mechanisms of the soil-cable behaviour and observe if the trends observed experimentally are repeatable in a numerical simulation, most notably considering the order of magnitude strain reduction in the cable compared to the soil and shape of the strain profile. The aim was not to provide exact predictions at these low stresses, which are not representative of full-scale behaviour. For this reason, it was decided to use Equation 3.4 with the original values of $Q = 10$ and $R = 1$ to provide a reasonable estimate of I_R.

The angle of maximum dilation can be estimated according with the following expression (Schanz and P. A. Vermeer 1996):

$$\psi_{max} = \arcsin\left(\frac{I_{R,f}}{I_{R_f} + 6.7}\right) \tag{3.5}$$

where I_{R_f} is the dilatancy index evaluated at failure (i.e. when $p' = p'_f$). The angle of maximum dilation, ψ_{max}, is a key constitutive parameter in the model selected for this research, which needs to be assessed independently for each relative density selected for modelling. To this aim, an average value of the mean effective stress p' along the layer thickness was assumed for each of the three cases and the value of the peak friction angle ϕ'_p (equation (1)) was selected in order to keep the same value of the critical friction angle, $\phi'_c = 34°$ (Thomas Benz 2007).

Stiffness decay with strain level at low confining stress

The HSsmall model accounts for the decay of shear stiffness with the shear strain through two parameters: (a) the initial shear stiffness modulus G_0 and (b) the shear strain level at which the reduction of stiffness modulus is $G/G_0 \approx 0.7$, also called $\gamma_{0.7}$,

which uniquely defines the stiffness decay curve (T. Benz, Schwab and P. Vermeer 2009). The initial shear stiffness modulus G_0 of Hostun sand was evaluated according to (Oztoprak and Bolton 2011):

$$G_0 = \frac{5760 \cdot p_{atm}}{(1+e)^3} \cdot \left(\frac{p'}{p_{atm}}\right)^{0.5} \tag{3.6}$$

where p_{atm} is the atmospheric pressure (i.e. 100 kPa); e is the void ratio, assumed to be constant through the depth of the sand layer; and p' is the target mean stress level.

The material model takes into account the dependency of shear stiffness modulus G_0 on the confining pressure through the following equation:

$$G_0 = G_0^{ref} \cdot \left(\frac{\sigma'_3}{p_{ref}}\right)^m \tag{3.7}$$

where G_0^{ref} is the shear stiffness at the reference pressure and can be computed by substituting Equation 3.7 into Equation 3.6, assuming that $p' = \sigma'_3 = p_{ref} = p_{atm} = 100$ kPa.

Experimental evidence has shown that the shear strain level $\gamma_{0.7}$ is also a function of the stress level (Darendeli 2001, Wichtmann and Triantafyllidis 2004). Unfortunately, the material model does not take this dependence into account. In order to correct for this, the following equation was used to scale the shear strain level $\gamma_{0.7}$ to the appropriate stress level (Darendeli 2001):

$$\gamma_{0.7} = (\gamma_{0.7})_{ref} \cdot \left(\frac{p'}{p_{ref}}\right)^{0.5} \tag{3.8}$$

where p' is the target stress level; p_{ref} is the reference confining stress level (usually taken as equal to 100 kPa, i.e. atmospheric pressure); and $(\gamma_{0.7})_{ref}$ is the shear strain level at the reference confining stress level.

Dependency of the stiffness on stress at medium to large strain level

HSsmall incorporates power laws to define the dependency of the stiffness parameter at medium to large strains on the confining stress. The soil stiffness is defined through

three moduli: (a) the secant stiffness modulus at 50% of the peak deviatoric stress in a standard drained triaxial test, E_{50}; (b) the one-dimensional compression tangent modulus, E_{oed}; and (c) the unloading-reloading modulus, E_{ur}. They are obtained using the following equations:

$$E_{50} = E_{50}^{ref} \cdot \left(\frac{\sigma_3'}{p_{ref}} \right)^m \tag{3.9}$$

$$E_{oed} = E_{oed}^{ref} \cdot \left(\frac{\sigma_1'}{p_{ref}} \right)^m \tag{3.10}$$

$$E_{ur} = E_{ur}^{ref} \cdot \left(\frac{\sigma_3'}{p_{ref}} \right)^m \tag{3.11}$$

where E_{50}^{ref}, E_{oed}^{ref} and E_{ur}^{ref} are the values at the reference confining stress level (see Table 3); σ_1' and σ_3' are the principal confining stresses and m is a power that defines the stress-level dependency of the stiffness. The reference values for the stresses were taken from Thomas Benz 2007 for loose (D_R =20-35%) and dense sand (D_R =72-84%), based on drained triaxial and biaxial tests on Hostun sand. For the intermediate value of relative density, a linear interpolation was used. Table 3.3 shows the set of model parameters adopted in this paper.

The soil model's parameters chosen for the analyses at large confining stresses are the same as for the same relative density at low confining stresses (Table 3.3), with the exception of $\psi = 20.8°$, $\phi_p' = 49.8°$ and $\gamma_{0.7} = 0.0002$, modified to account for the different stress level at the trapdoor depth.

Strain transfer within the cable could potentially be affected by the composite structure of the cable and a lack of shear transfer between each composite layer (i.e. buffer, cladding and glass core), which all have different mechanical properties. Ansari and Libo 1998 have shown that the internal structure of some fibre optic cables can influence the strain reading by 30-50% of its real value if the gauge length is shorter than 60 mm. For longer gauge length, the attenuation maybe be reduced by a factor of 10%. This research applied to Michelson interferometric sensors, which are different cables from the cable selected for this study, with high internal shear transfer loss. The cable used for this research was calibrated by uniaxial tensile tests at different

Table 3.3: Constitutive parameters values used in the HSsmall model for the soil.

Parameter	Symbol	Units		$1g$		$40g$
			$D_R = 20\%$	$D_R = 20\%$	$D_R = 52\%$	$D_R = 87.5\%$
Cohesion	c	kPa	0	0	0	0
Angle of internal friction (peak)	ϕ'_p	°	34	49.6	55.1	49.8
Angle of dilatancy	ψ_{max}	°	0	20.6	28.8	20.8
Secant stiffness in standard drained triaxial test	E_{50}^{ref}	kPa	12000	21470	30000	30000
Tangent stiffness for primary oedometer loading	E_{oed}^{ref}	kPa	16000	23360	30000	30000
Unloading/reloading stiffness	E_{ur}^{ref}	kPa	60000	75780	90000	90000
Shear stiffness modulus	G_0^{ref}	kPa	81500	88650	138000	138000
Power for stress-level dependency of stiffness	m	–	0.75	0.55	0.55	0.55
Poisson's ratio for unloading-reloading	ν_{ur}	–	0.25	0.25	0.25	0.25
Reference stress for stiffness	p'_{ref}	kPa	100	100	100	100
k_0 value for normal consolidation	k_0	–	0.44	0.44	0.40	0.40
Shear strain level at which $G_s/G_{0,0.7}$	$\gamma_{0.7}$	–	0.000022	0.000034	0.00004	0.0002

strain levels, showing very minimal loss caused by internal shear transfer (Kechavarzi et al. 2016). Consequently, this phenomenon was ignored in modelling going forward, and efforts were concentrated on understanding the effects of shear strain loss at the soil cable interface, an acknowledged key limitation of the use of DFOS for this type of application (Gutiérrez et al. 2019), and an even stronger limitation of the work from Möller et al. 2023 at $1g$ (X. Xu, Abadie et al. 2022). The 2 mm diameter DFOS cable was modelled as an embedded beam element (Sadek and Shahrour 2004), with a three-noded line element that can cross a ten-noded tetrahedral element meshing the soil. A built-in interface element was used to model the cable surface properties to best represent the soil cable interaction. The beam element was assumed as an indefinitely elastic element, with an equivalent elastic modulus of $E = 200$ MPa. The embedded interface was elastic perfectly plastic. The elastic stiffness of the element is assigned not to alter the elastic response of the cable soil system, while the plastic behaviour is attained when a limiting shear force acts along the element skin, t_s, that is defined per unit length of the cable, according to:

$$|t_s| = \sigma_n^{avg} \cdot R_{inter} \cdot \tan(\phi') \cdot \pi D \tag{3.12}$$

where σ_n^{avg} is the average soil normal stress on the cable skin surface evaluated at each step during the analysis, ϕ' is the soil's mobilised angle of friction and D is the

cable diameter. This means that the embedded beam interface reaches failure when the soil reaches its maximum shear stress (i.e. when the mobilised angle of friction is equal to the peak angle of friction $\phi' = \phi'_p$). R_inter is a strength reduction factor that allows the modelling of a smooth interface ($R_{inter} = 0.01$) or a rough interface ($R_{inter} = 1$). The latter behaviour is used to approximate the cable behaviour when coated with glued sand. The embedded beam elements were fully fixed at the lateral boundaries of the model, far from the trapdoor, although such a level of constraint may not have developed in the tests at low relative densities, and was only observed at higher relative densities (Möller et al. 2023). This modelling choice was used to verify that this boundary constraint does not affect the cable deformation in the proximity of the trapdoor.

3.2 Interferometric SAR technique

This section describes the methodology applied by the author in the generation of the results of Section 4.2.

The fundamental reason of using microwaves for satellite remote sensing is that they have the capability to penetrate clouds and can even get trough the top layer of canopies, dry soils or sands (depending on the wavelength by as much as a few meters in some cases) (Figure 3.4). Moreover some physical parameters, such as the water content, can be directly related to the back-scattered energy of the signal.

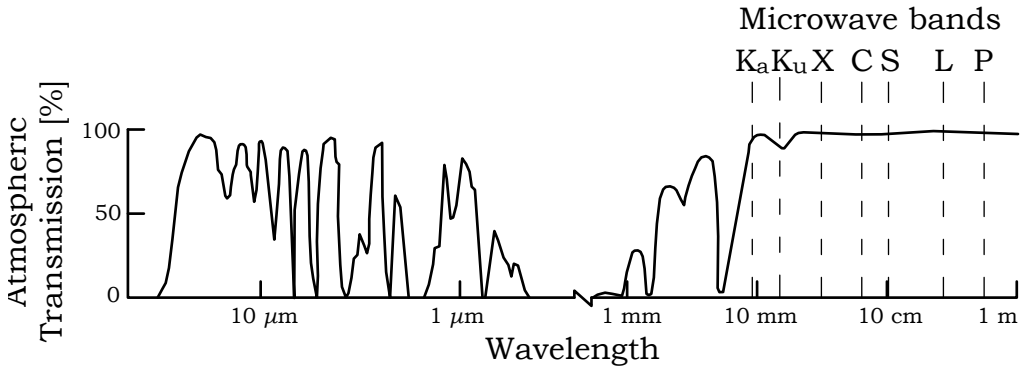


Figure 3.4: Atmospheric signal transmission (adapted from Henderson and Lewis 1998), with the indication of the main bands used in satellite remote sensing.

Satellite remote sensing is an active system, meaning that it provide its own *illumination* to the target. Therefore it is possible to monitor the Earth's surface in whatever weather condition during day or night.

Various wavelengths employed in satellite remote sensing are correspondingly linked to distinct letters of the alphabet, uniquely identifying each band. In Figure 3.4 are shown the main seven bands used in this field, which are detailed reported in Table 3.4 as well.

3.2.1 Background on electromagnetic waves

Fundamentals of electromagnetic waves

A full description of current theories of electromagnetic (EM) radiation is well beyond the scope of this section, but in general there are two common ways to describe EM radiation: that of the wave and that of the particle. In case of microwave remote sensing most of the phenomenon are best described with the wave theory. Therefore quantities such as the frequency, wavelength, interference, polarisation and scattering must be well understood.

Let us consider a wave travelling in time along the z-axis, that can be described by the following equation (it is possible to use any harmonic function, but for simplicity let us assume a sine function):

$$\psi(z,t) = A \cdot \sin\left(k \cdot z - \omega \cdot t + \phi_0\right) \tag{3.13}$$

where A is the Amplitude of the wave, k is the *wavenumber*, ω is the *angular*

Table 3.4: Wavelength bands used in satellite remote sensing.

Band	K_a	K_u	X	C	S	L	P
Wavelength λ [cm]	0.8-1.1	1.7-2.4	2.4-3.75	3.75-7.5	7.5-15	15-30	30-100
Frequency f [GHz]	26.5-40	12.5-18	8-12.5	4-8	2-4	1-2	0.3-1

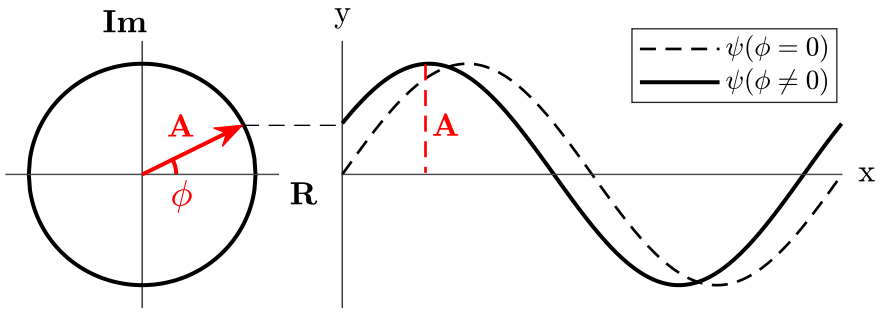


Figure 3.5: Equation 3.15 with the indication of the phase ϕ and amplitude A of the wave function.

frequency and ϕ_0 is the *initial phase*, defined as follows:

$$(a) \quad k = \frac{2\pi}{\lambda} \qquad (b) \quad \omega = 2\pi \cdot f \qquad (c) \quad c = \lambda \cdot f \tag{3.14}$$

where λ is the *wavelength*, f is the *frequency* and c is the speed of light (in case of EM in the vacuum).

Of course, Equation 3.13 is not the only one able to mathematically represents a wave. Indeed there is another way which is far more easy to use when dealing with EM waves, and uses the properties of complex numbers (Euler's formula):

$$\psi(z,t) = A \cdot e^{i \cdot \phi} = A \cdot e^{i(k \cdot z - \omega \cdot t + \phi_0)} \tag{3.15}$$

Using Equation 3.15 the complex wave can be represented as a point moving in the complex plane, where the distance from the origin corresponds to the amplitude, and the angle with the positive real axis represents the phase angle as shown in Figure 3.5.

Electromagnetic waves in radar systems

In case of satellite microwave remote sensing, the wave function used to describe the EM wave is the so called *cardinal sine* (Figure 3.6), described as follows:

$$sinc = \begin{cases} \frac{sin(x)}{x}, & x \neq 0 \\ 1, & x = 0 \end{cases} \tag{3.16}$$

The reason behind the use of this particular function is that the presence of the main

peak, and the side lobes, helps in understanding and analyzing the range resolution capabilities of Synthetic Aperture Radar (SAR). A radar (i.e. *radio detection and ranging*) is a device that transmits EM waves through an antenna, listening then for echoes reflected back by targets. The time Δt taken by the pulse to travel from the antenna to the target and back is used to estimate the distance R_T between them. Assuming that the signal is traveling in vacuum (at the speed of light c), and considering the two-way path, the distance can be calculated as:

$$R_T = \frac{c \cdot \Delta t}{2} \tag{3.17}$$

The capacity to distinguish between two close targets is called range resolution ρ_{rg}, that with the adoption of modulated signals like chirps (i.e. a waveform whose frequency changes as a function of time, sweeping a given bandwidth B around the carrier frequency f) can be expressed as:

$$\rho_{rg} = \frac{c}{2B} \tag{3.18}$$

So, with the use of the *cardinal sine* and modulated signal, the mathematical description of wave equation used in SAR applications is as follows (Perissin 2018):

$$\psi(t) = A \cdot e^{i \cdot 2\pi \cdot f \cdot \Delta t} \cdot sinc[B(t - \Delta t)] \qquad in\ time\ domain \tag{3.19}$$

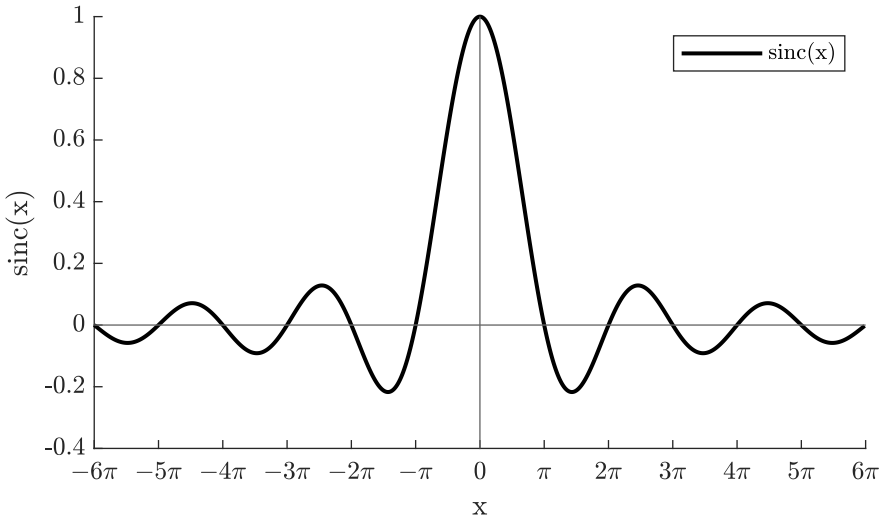


Figure 3.6: Plot of *cardinal sine*

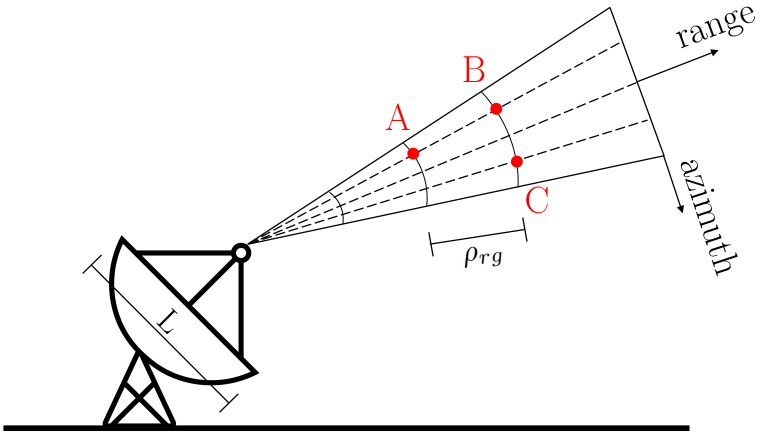


Figure 3.7: Radar resolution in azimuth direction. Point A and B (or A and C) have different range and can be uniquely identified. Point B and C fall within the same resolution cell in azimuth direction and cannot be uniquely identified.

$$\psi(r) = A \cdot e^{i \cdot \frac{4\pi}{\lambda} \cdot R_T} \cdot sinc \left[\frac{2B}{c}(r - R_T) \right] \qquad in\ space\ domain \tag{3.20}$$

where all the quantities have been previously described. Basic radar systems have limitations in accurately determining the position of a target in the direction perpendicular to the range. This constraint is due to the directional nature of the antenna, defined by its limited angular aperture θ, which is defined as the ratio between the wavelength λ and the antenna length L. Therefore the radar azimuth resolution ρ_{az} can be expressed as follows (see Figure 3.7):

$$\rho_{az} = \sin\theta \cdot R_T \approx \frac{\lambda}{L} \cdot R_T \tag{3.21}$$

From this Equation is clear that in case of satellite microwave remote sensing, with a sensor positioned 600 to 800 km from the target and operating with a wavelength in the order of centimeters, huge physical antennas are needed in order to achieve meter-scale resolution in azimuth direction. To overcome this issue, during the 1950s engineers realised that by exploiting the *Doppler effect* (i.e. s the change in the frequency of a wave in relation to an observer who is moving relative to the source of the wave) it is possible to drastically increase the resolution of the system, hence the concept of synthetic aperture. A Synthetic Aperture Radar (SAR) is a side-looking, imaging radar

system that uses the motion of the sensor to synthesize a much larger aperture, and hence improve azimuth resolution to a useful degree. Basically, multiple acquisitions of the same target are registered from the moving antenna at discrete time intervals Δt, and then opportunely combined together to mimic the behaviour of a larger antenna. Therefore the virtual length in Equation 3.21 becomes the distance traveled by the radar from the beginning to the end of the signal transmission.

3.2.2 Radar image characteristics

The amplitude of radar images

A radar image serves as a visual representation of data acquired by radar systems. The latter can be separated in a real component (the amplitude) and a complex component (which contains information about the phase), as can be noted in Equation 3.15. Starting from the real component, the radar image is a raster structured with rectangular (or square) pixels, often referred to as resolution cells. The aspect ratio of these pixels is function of the sensor's range and azimuth resolution. Each pixel in the image encapsulates the amplitude A of the back-scattered signal received from its corresponding resolution cell.

Typically presented in greyscale, the radar image utilizes a color spectrum where black identifies low back-scattering, and white denotes intense back-scattering. This coloration scheme effectively conveys the strength of signals returned from different regions within the image, offering a visual insight into the reflective characteristics of the observed surfaces or objects. Usually good scatterers are buildings and man made structures, rocks and rough surfaces, while poor scatterers are vegetations, shadow areas (see the following Figure 3.9) and smooth surfaces. Note that the classification of surfaces into smooth and rough actually depends on the wavelength of the signal, and that the intensity of the back-scattered signal is influenced by the material properties of the target.

In a radar image the horizontal axis typically represents the azimuth (i.e the direction in which the radar is moving), while the vertical axis usually represents the range (i.e. distance or range from the radar antenna).

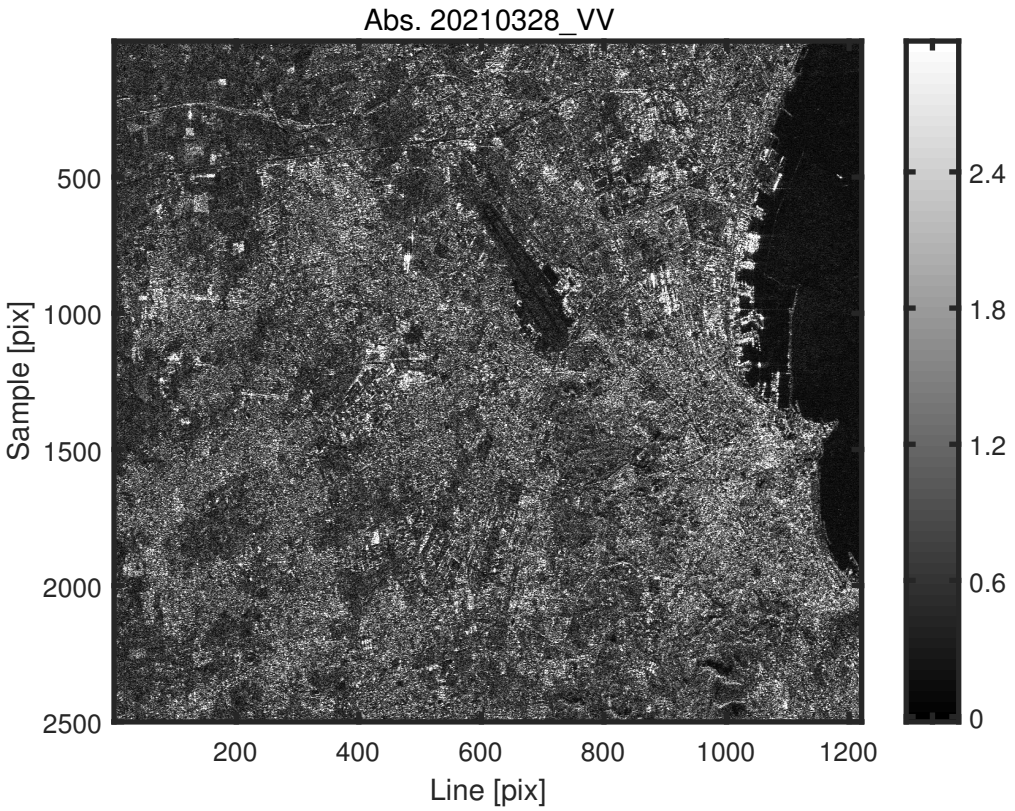


Figure 3.8: Amplitude of an acquisition in descending orbit made by Sentinel 1 on March 28^{th} 2021 over the city of Naples, Italy. Notice the presence of strong scatters in the urban area while the sea and the vegetations show poor scattering. Figure obtained using the software SARproZ (Perissin, Z. Wang and T. Wang 2011).

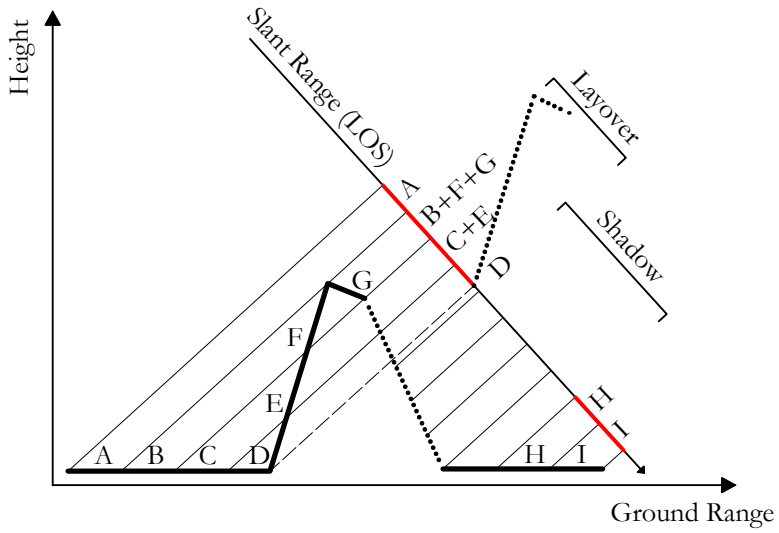


Figure 3.9: Layover and shadow effects. In red the detected scatters.

Radar images in the range direction are essentially the projection of scatterers (reflective points or objects) on the ground onto the slant range direction (i.e. line of sight (LOS)). In other words, the radar image represents how objects at ground level are distributed along the line of sight from the radar. Owing to this peculiar viewing geometry, radar images are affected by two types of distorsions, namely layover and foreshortening, along with the presence of a shadow effect. Depending on the terrain slope (Figure 3.9), scatterers that are located at increasing ground range positions can be imaged in reverse order by the SAR system (points D, E, F and G in Figure 3.9). Moreover they are imaged in the same SAR resolution cells as scatterers B and C, which belong to a different area on the ground (layover). On the other side of the elevation profile, scatterers located between G and H cannot be illuminated by the radar since they are in shadow. As a consequence, SAR resolution cells from G to H do not contain any signal from the ground and they generate a dark gap on the detected image (shadow). In other cases, when the slope is moderately inclined, scatterers that are positioned on it are affected by foreshortening, so that the apparent length of the objects along the radar beam is compressed, making them appear shorter than their true dimensions (Figure 3.10).

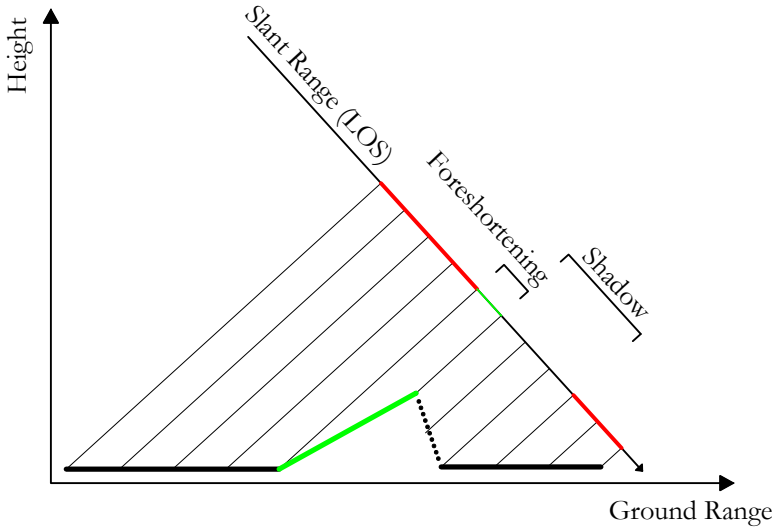


Figure 3.10: Foreshortening and shadow. In green the cells affected by foreshortening.

The phase of radar images

Moving on to the complex component of the acquired data, in Figure 3.11 is shown the phase of the SAR image depicted in Figure 3.8.

The figure of the phase looks simply noisy. This is due to the independency of the phase of nearby resolution cells. In fact, each resolution cell is plotted with a color showing the corresponding phase value ϕ. Assuming that a single target is present in a resolution cell, the phase can be expressed as a function of its distance R_T from the sensor according to the following equation:

$$\phi = \frac{4\pi}{\lambda} \cdot R_T \tag{3.22}$$

This phase quantity is ambiguous and it is expressed in radiants (Figure 3.5). Since the target could be located anywere within the resolution cell, it is clear that there is no correlation between the phases of adjacent resolution cell. In case of more targets falling within the same resolution cell, an interaction occurs whereby each scatter contributes to the radar signal detected by that single resolution cell. If the interaction is constructive it means that the contributions from different scattering elements within the same resolution cell add up, resulting in a stronger and more pronounced radar signal (see Figure 3.12(a)). On the other hand, destructive interaction happens when

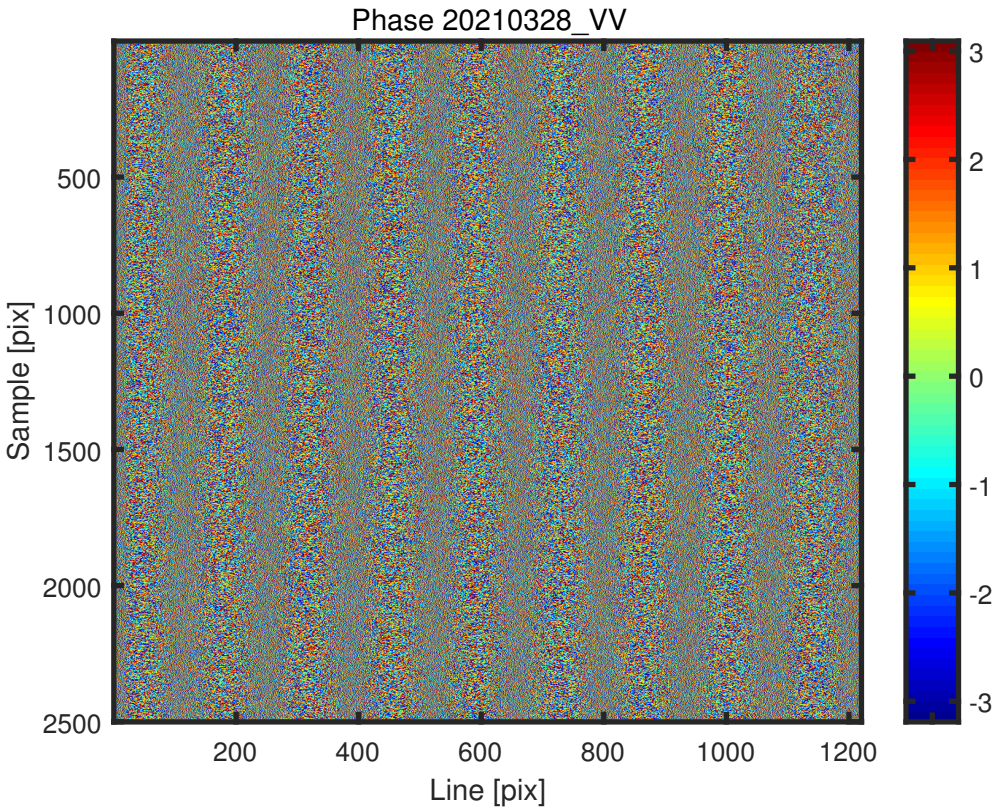


Figure 3.11: Phase of an acquisition in descending orbit made by Sentinel 1 on March 28^{th} 2021 over the city of Naples, Italy. The phase illustrated here refers to the same image shown in Figure 3.8. Figure obtained using the software SARproZ (Perissin, Z. Wang and T. Wang 2011).

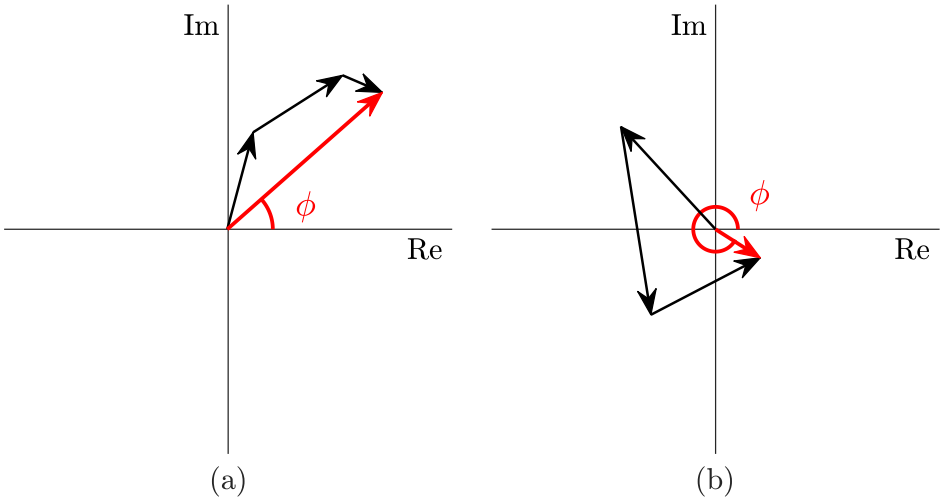


Figure 3.12: Interaction between targets within the same resolution cell. (a) Constructive interaction, (b) destructive interaction.

the individual signals or waves weaken or cancel each other out (see Figure 3.12(b)).

3.2.3 SAR interferometry

In the previous section we have seen that due to the physical differences between resolution cells and the random distribution of the elementary scatterers corresponding to each pixel, each having a certain distance from the sensor, phase values, even from neighbouring pixels within a single SAR image, are unrelated, random, and of no practical use. It is only when corresponding pixels from two SAR images of the same place acquired at different times (and/or from slightly different angles) are compared that the phase values can provide useful information.

Synthetic Aperture Radar Interferometry (InSAR) involves the use of two SAR images acquired over the same area at different times from slightly different acquisition geometries to make an interferogram (Figure 3.13), where the phase of each corresponding pixel is differenced to highlight any possible changes.

An interferogram between two SAR images (j and k) can be expressed as:

$$INT_{j,k}(r,a) = \psi_j(r,a) \cdot \psi_k^*(r,a) = A(r,a) \cdot e^{i \cdot \Delta\phi(r,a)} \tag{3.23}$$

where $A(r,a)$ is the amplitude coming from the product of A_j and A_k and $\Delta\phi$ is the phase difference between ϕ_j and phi_k. In the latter equation the product is applied

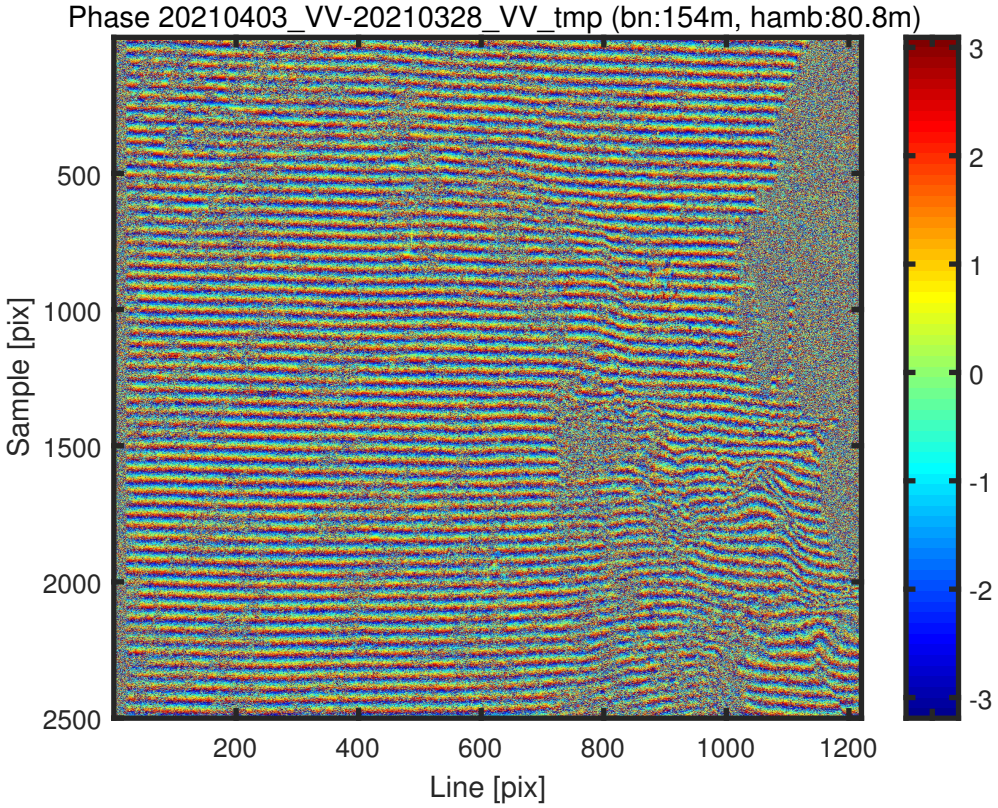


Figure 3.13: Interferogram between Sentinel 1 images acquired in descending orbits respectively on March 28^{th} 2021 (Master Image) and April 3^{rd} 2021 (Slave Image). Figure obtained using the software SARproZ (Perissin, Z. Wang and T. Wang 2011).

pixel to pixel (r and a are the range and azimuth coordinate respectively) and the sign * indicates the complex conjugate. The most important term is the phase variation $\Delta\phi$, and exploiting Equation 3.22 it can be expressed as:

$$\Delta\phi(r,a) = \frac{4\pi}{\lambda} \cdot (R_j(r,a) - R_k(r,a)) \tag{3.24}$$

As can be noted from the latter equation, phase variations $\Delta\phi$ are due to changes in the sensor-to-target distance. This can happen for several several reasons such as:

- changes in the acquisition geometry of the sensor (i.e. SAR images acquired from different positions);
- changes in the radar signature of the object on ground;
- target movement along the sensor-to-target direction (i.e. Line of Sight direction, LoS);
- different atmospheric conditions at the time of acquisition (atmospheric artifacts) that delays the signal (i.e. change of the speed v at which the waves propagate).

Indeed the phase variation between two satellite SAR acquisitions is generally expressed with the following equation, which represents the base of the understanding the InSAR application:

$$\Delta\phi = \Delta\phi_{flat} + \Delta\phi_{topo} + \Delta\phi_{topo,res} + \Delta\phi_{displ} + \Delta\phi_{atmo} + \Delta\phi_{noise} \tag{3.25}$$

where:

- $\Delta\phi_{flat}$ accounts for the phase variation resulting from changes in slant range, arising from the distinct viewing geometries when satellites acquire SAR images;
- $\Delta\phi_{topo}$ and $\Delta\phi_{topo,res}$ are phase variations due to the topography;
- $\Delta\phi_{displ}$ is the phase variation induced by displacements along the line of sight of the satellite;
- $\Delta\phi_{atmo}$ is the phase variation induced by the presence of atmospheric artifacts that delays the radar signal;
- $\Delta\phi_{noise}$ is the phase variation that represents the instrumental error of the monitoring technique, associated to inevitable noise.

The focus of the Interferometric SAR (InSAR) technique is on the detection of

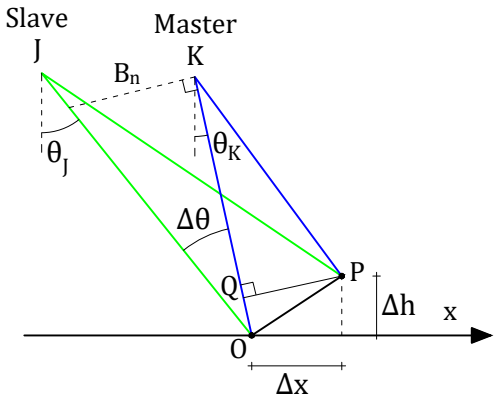


Figure 3.14: Acquistion geometry for interferogram formation.

$\Delta\phi_{displ}$ phase component, in order to retrieve information on the displacements. Each of this term will be briefly described in the following sections.

Flat terrain phase component

In the previous section we have seen that the phase variation calculated from Equation 3.23 can be separated in multiple components, the first of which is the $\Delta\phi_{flat}$ that account for the phase variation resulting from a two distinct viewing geometries. Let's consider the geometry scheme shown in Figure 3.14, where the satellite acquires the back-scattered signal of two points on the Earth's surface (namely O and P) from the position K (called Master acquisition) and after a certain period of time from the position J (called Slave acquisition).

In Figure 3.14, θ_K is the incidence angle of the first acquisition, θ_J is the that of the second one and $\Delta\theta$ is the difference of these values, Δx is the distance in x direction of point P from the origin O and Δh is the height of point P with reference to the origin O, B_n is the so called normal baseline which is the projection of the interferometric baseline (i.e. the distance between the two satellite positions) onto the slant range direction of the Master satellite. Via trigonometry is it possible to demonstrate that the phase variation induced by the Δx component only (hence the term 'flat terrain') can be expressed as follows:

$$\Delta\phi_{flat} = \frac{4\pi}{\lambda} \cdot \frac{B_n}{\overline{KO}} \cdot \frac{\overline{OQ}}{\tan\theta_K} \tag{3.26}$$

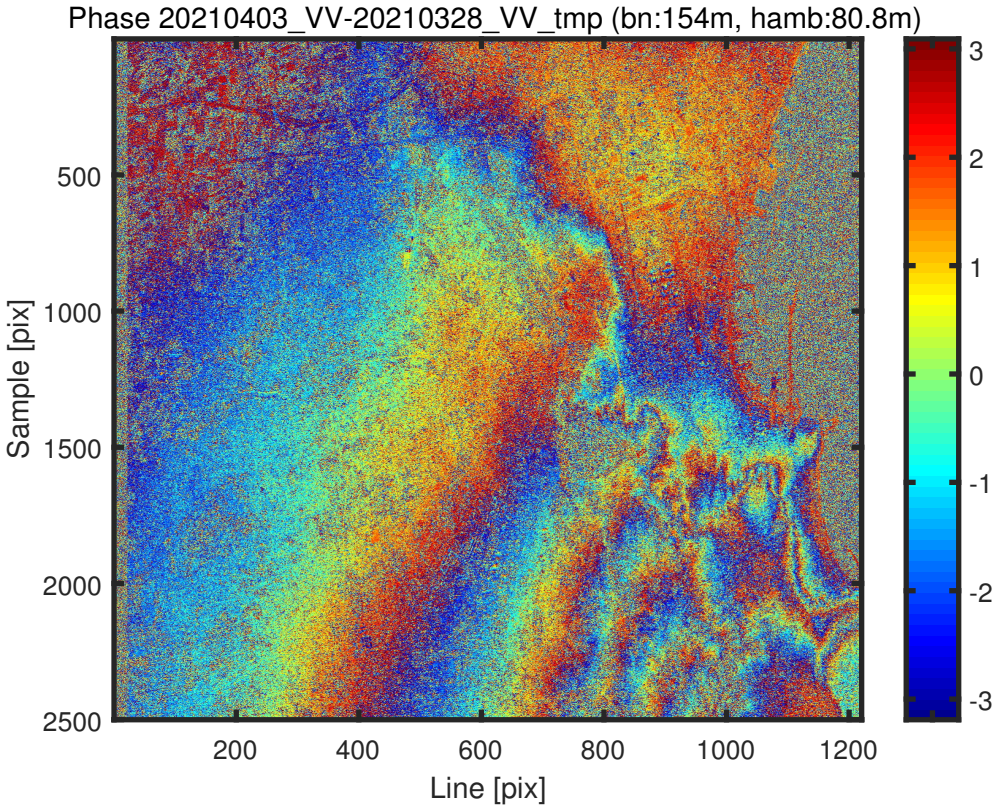


Figure 3.15: Interferogram of Figure 3.13 after removing the flat phase component using Equation 3.26. Figure obtained using the software SARproZ (Perissin, Z. Wang and T. Wang 2011).

This equation represents the phase variation of point P with respect to the origin O. It can be noted that the flat terrain phase component is directly proportional to the normal baseline B_n and can be computed once is known the exact relative position of the satellites and their positions relative to the acquired area of interest (i.e. orbit paths). This phase component does not bring any useful information and therefore it can be removed from the interferogram, thus obtaining a new interferogram as shown in Figure 3.15 that represents the other five components of Equation 3.25. This first step, aimed at removing the flat phase component, belongs to the Interferometric Synthetic Aperture Radar (InSAR) technique, which is used to reconstruct the Digital Elevation Model (DEM) of the area under investigation.

Topographic phase component

The second phase component appearing in Equation 3.25 is that induced by the Δh component only, thus representing the phase variation of point P with respect to the origin O due to the morphology of the area. Again, using the same geometry pictured in Figure 3.14, it is possible to demonstrate via trigonometry that the topographic phase variation can be expressed as follows:

$$\Delta\phi_{topo} = \frac{4\pi}{\lambda} \cdot \frac{B_n}{\overline{KO}} \cdot \frac{\Delta h}{\sin\theta} \tag{3.27}$$

In the latter the height of point P with respect to the origin O (i.e. Δh) appears directly in the equation. Therefore, to calculate the phase component $\Delta\phi_{topo}$, and be able to remove it from the overall phase, it is necessary to know the topography of the area of interest. This is achieved using a Digital Elevation Model (DEM), such as that retrieved by the Shuttle Radar Topography Mission (SRTM). The latter is a space shuttle mission conducted by NASA (National Aeronautics and Space Administration) aimed at obtaining high-resolution DEM, in particular two main output have been produced, namelu SRTM 3 Arc-Second with a spatial resolution of 90×90 meters and SRTM 1 Arc-Second with a spatial resolution of 30×30 meters.

Actually, the interferogram of Figure 3.15 reprsents the DEM of the area under investigation, assuming that no displacements have occurred between March 28^{th} 2021 and April 3^{rd} 2021 and that both SAR images were acquired in similar atmospheric conditions. Each phase jump displayed in Figure 3.15 represents a height variation of about 80 meters. Indeed, reversing Equation 3.27 it is possible to calculate the height of ambiguity Δh_a assuming a full cycle (i.e. 2π) for the $\Delta\phi_{topo}$:

$$\Delta h_a = \frac{\lambda \cdot \overline{KO} \cdot \sin\theta}{2 \cdot B_n} \tag{3.28}$$

For the specific area, Sentinel 1 acquired data at a distance of $\overline{KO} = 800$ km with an incidence angle of $\theta = 34°$ having a wavelenght of $\lambda = 5.6$ cm. For the two acquistions used to generate the interferogram in Figure 3.15 the normal baseline is equal to $B_n = 154$ meters, thus leading to an height of ambiguity of about 80 meters. The height of ambiguity is an estimate of the interferometry sensitivity to topography.

For B_n approaching zero SAR interferometery can not be used for the DEM generation. However, in this particular situation, assuming no temporal change in the atmospheric conditions, removing the flat phase component, the interferometric phase depends only on the diplacement phase component.

Using a DEM, such as the SRTM 1 arcsec shown in Figure 3.16, it is possible to remove the topographic phase component using Equation 3.27 from the interferogram shown in Figure 3.15. The new interferogram is shown in Figure 3.17, which represents the remaining four component of the fundamental phase in Equation 3.25. This second step, aimed at removing the topographic phase component from the fundamental phase belong to the Differential Interferometric SAR (DInSAR) technique, which is a powerful tool for detecting surface movements when one can assume no change in atmospheric conditions (i.e. $\Delta\phi_{atmo} = 0$) and no residual topographic phase componet is remained after removing the DEM (i.e. $\Delta\phi_{topo,res} = 0$).

Displacement phase component

The third phase component introduced in Equation 3.25 is denoted as $\Delta\phi_{displ}$ and arises from the displacement of targets along the line of sight. Considering a generic vector displacement $\vec{d}$ it can be decomposed in $\overrightarrow{d_h}$ and $\overrightarrow{d_v}$, respectively its component in the (x, z) plane. Via trigonometry it is easy to demonstrate that the line of sight displacement $\overrightarrow{d_{LOS}}$ detected by the satellite can be expressed as:

$$|\overrightarrow{d_{LOS}}| = |\overrightarrow{d_h}| \cdot \sin\theta + |\overrightarrow{d_v}| \cdot \cos\theta \tag{3.29}$$

The signal emitted by the Synthetic Aperture Radar (SAR) aboard the satellite undergoes a round trip to the target, so a full cycle in the phase variation corresponds to a displacement equal to half wavelength of the signal. Therefore the phase variation associated to displacement can be expressed by the following equation:

$$\Delta\phi_{displ} = \frac{4\pi}{\lambda} \cdot d_{LOS} \tag{3.30}$$

This equation shows the sensitivity of this technique in detecting displacements along the line of sight (LOS) of the satellite. This means that given a single acquisition

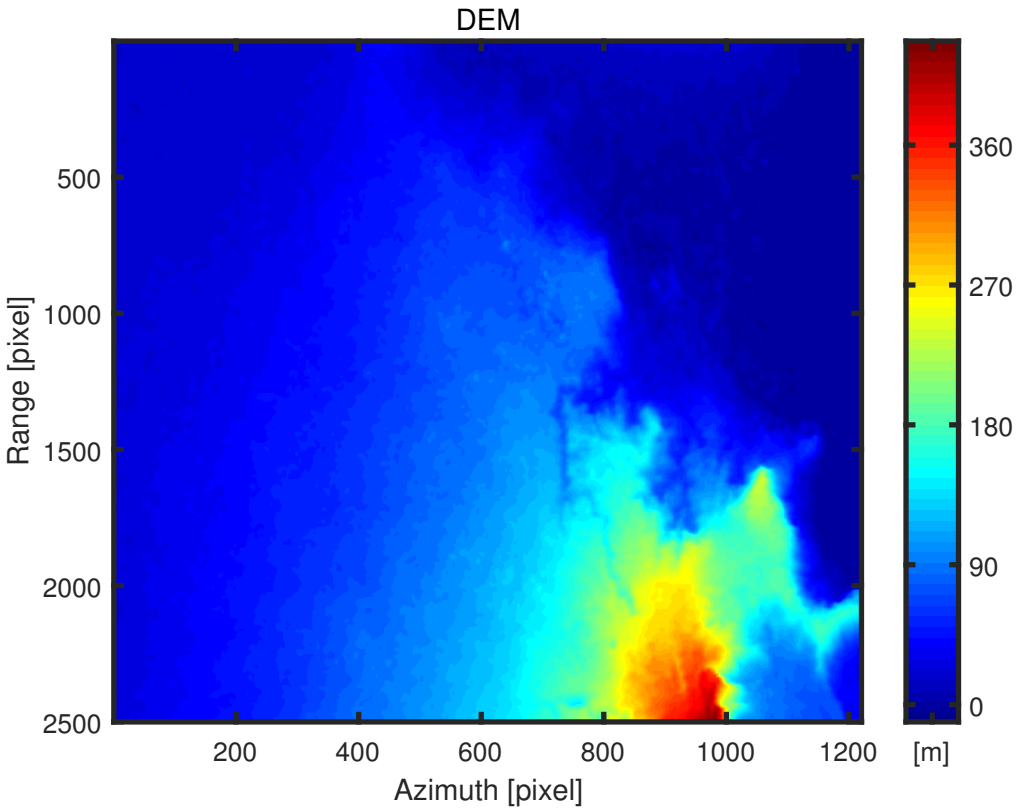


Figure 3.16: Digital Elevation Model (DEM) from the Shuttle Radar Topography Mission (SRTM) 1 Arc-Second. DEM obtained from the U.S. Geological Survey database. Figure obtained using the software SARproZ (Perissin, Z. Wang and T. Wang 2011).

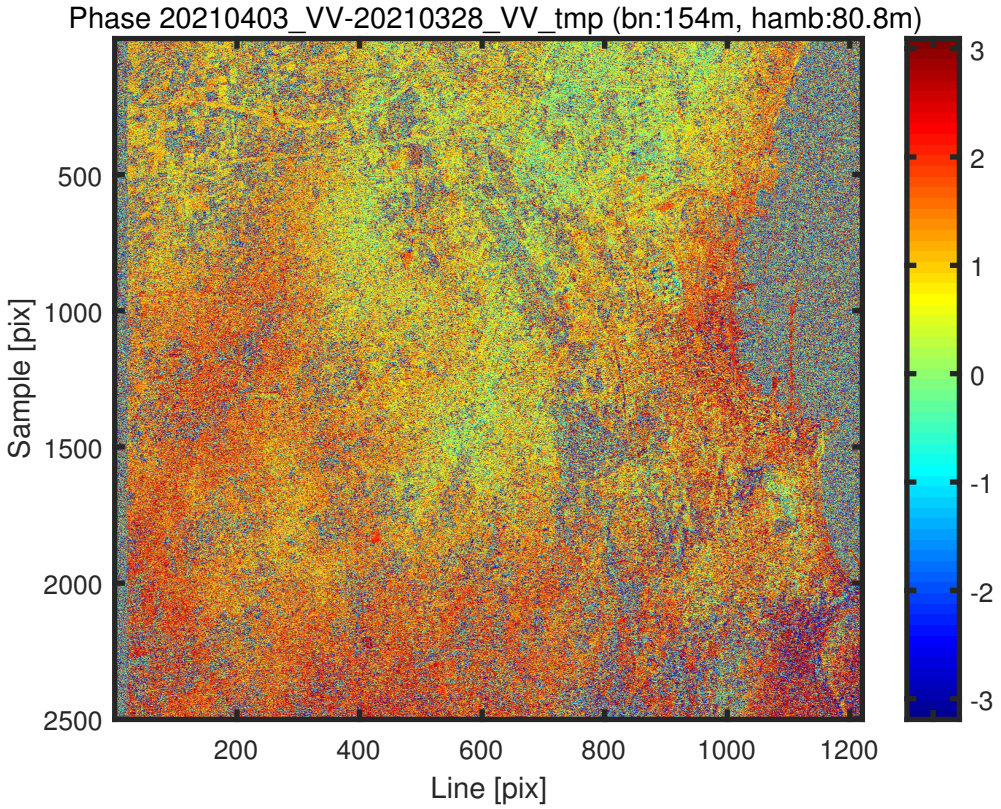


Figure 3.17: Interferogram of Figure 3.15 after removing the topographic phase component using Equation 3.27. Figure obtained using the software SARproZ (Perissin, Z. Wang and T. Wang 2011).

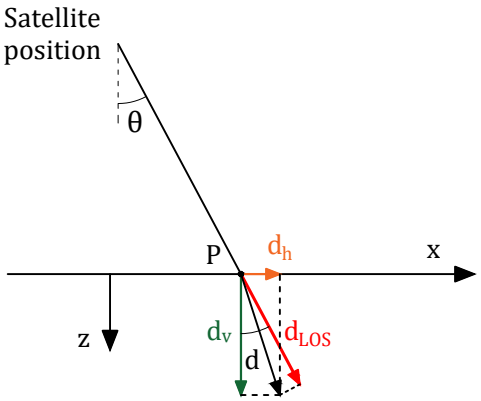


Figure 3.18: Conversion of a generic displacement $\vec{d}$ in a displacement along the line of sight of the satellite $\overrightarrow{d_{LOS}}$.

geometry (i.e. ascending or descending) is not possible to reconstruct the direction of the displacement. Furthermore, a displacement occurring orthogonal to the (x, z) plane would go undetected by the satellite.

Atmospheric phase component

When two interferometric SAR images are not simultaneous, the signal for each can be affected differently by the atmosphere. In particular, different atmospheric humidity, temperature and pressure between the two acquisitions have a visible consequence on the interferometric phase. This effect is usually confined within a 2π full loop phase change along the image with a smooth spatial variability (from a few hundred metres to a few kilometres, depending on the satellite resolution and wavelength, notice for example Figure 3.17). The effect of such a contribution impacts on both altitude (especially in the case of small baselines) and terrain deformation measurements. Therefore, the expected millimeter precision of displacement measurements turns into centimeters accuracy, while the metric precision in height estimation can quickly become tens of meters (Perissin 2016).

Evaluating the atmospheric phase component presents a challenge in DInSAR techniques, but this obstacle can be overcome using advanced methods such as Multi-Temporal InSAR (MT-InSAR), that will be described in section ABC.

3.2.4 Persistent Scatterers Interferometry

In the preceding section, we provided an overview of SAR interferometry fundamentals, elucidating the InSAR and DInSAR methodologies. These techniques enable the estimation of both the elevation and displacements within the specified area of interest. Nonetheless, SAR interferometry presents us several significant challenges. Firstly, interferograms encounter decorrelation issues, manifesting as temporal and/or geometrical decorrelation. Secondly, the interferometric phase is wrapped (as illustrated in Figure 3.15 or Figure 3.17, where phase changes fluctuate between $-\pi$ to $+\pi$). Unwrapping this phase accurately with a single interferogram can be a challenging task, if feasible at all. Additionally, in cases where the topography of the area lacks precise information (e.g. in urban areas, an outdated DEM may lack information about newly structures),

distinguishing between residual topography and terrain displacement becomes exceptionally challenging. Even after resolving these challenges, atmospheric artifacts pose a persistent threat, potentially undermining all corrective efforts and significantly biasing the detected signals.

In Section 2.3.2, we explored the evolution of interferometric techniques in the early 2000s, leading to the development of a novel method known as Persistent Scatterers Interferometry (PSI) or Permanent Scatterers Interferometry. This method exploits the stability of scatterers amplitude or phase to accurately estimate residual topography errors and surface displacements. The approach involves a multi-temporal strategy for interferogram generation.

A crucial aspect of this technique is the selection of stable pixels, typically achieved through the evaluation of the Amplitude Stability Index (ASI), computed using the following formula:

$$ASI = 1 - \frac{\sigma_A}{\mu_A} \tag{3.31}$$

Here, μ_A denotes the average amplitude of the pixel considered across the N SAR images, while σ_A represents the standard deviation of the amplitudes. The calculations for μ_A and σ_A are defined as follows:

$$\mu_A = \frac{1}{N} \sum_{i=1}^{N} A_i \tag{3.32}$$

$$\sigma_A = \sqrt{\frac{\sum_{i=1}^{N} (A_i - \mu)^2}{N}} \tag{3.33}$$

A scatterer exhibiting high stability will have a low variance ($\sigma \approx 0$), resulting in an ASI close to 1. Conversely, a scatterer with low stability may yield values of the ASI approaching zero or even negative values. The Amplitude Stability Index serves as a crucial criterion for identifying and selecting persistent scatterers, facilitating more accurate and reliable measurements in Persistent Scatterers Interferometry. Note that the artificial SAR image obtained by averaging the amplitude of the signal pixel by pixel is referred as Reflectivity Map (RM).

Another parameter suitable for pixels selection is the interferometric coherence (γ), that is a measure of the correlation between the complex radar backscatter values obtained from N SAR images for the selected pixel. It is defined by the following equation (Ferretti, Monti-Guarnieri, Prati, Rocca and Massonnet 2007):

$$\gamma = \frac{\left|\sum_{i=1}^{N} SAR_{i1} \cdot SAR_{i2}^{*}\right|}{\sqrt{\left|\sum_{i=1}^{N} SAR_{i1} \cdot SAR_{i1}^{*}\right| \cdot \left|\sum_{i=1}^{N} SAR_{i2} \cdot SAR_{i2}^{*}\right|}} \tag{3.34}$$

Here SAR_{i1} and SAR_{i2} represent the complex radar backscatter values for the pixel from the i^{th} SAR image and * denotes the complex conjugate. The numerator of the fraction represents the sum of the cross-products of complex values between corresponding pixels in the two SAR images over the N images. The denominator involves the square root of the product of the sums of the squared complex values for each SAR image. Interferometric coherence ranges from 0 to 1, where 0 indicates no correlation (random phase differences) between the SAR images, and 1 indicates perfect correlation (consistent phase relationships) over the N images. High coherence values suggest stable and coherent scattering behavior, making interferometric processing more reliable for applications such as terrain mapping and displacement monitoring.

After pixel selection using the chosen method, the subsequent step involves generating interferograms across the N Synthetic Aperture Radar (SAR) images. Generally, three methods are employed, as illustrated in Figure 3.19:

- star graph (or single master): in this approach, a single SAR image is designated as the Master image. The remaining images are then connected to the Master, resulting in the generation of $N-1$ interferograms, all linked to the chosen Master image (Figure 3.19 (a));
- small baseline graph (or Minimum Spanning Tree, MST): the small baseline graph strategy involves connecting the N SAR images with $N-1$ interferograms, emphasizing the reduction of temporal and spatial baselines. This method is particularly useful in scenarios where minimizing baseline effects is a priority (Figure 3.19 (b));
- full graph: in this case each SAR image is connected with the remaining $N-1$ images, leading to the generation of $N \cdot (N-1)/2$ interferograms. This approach

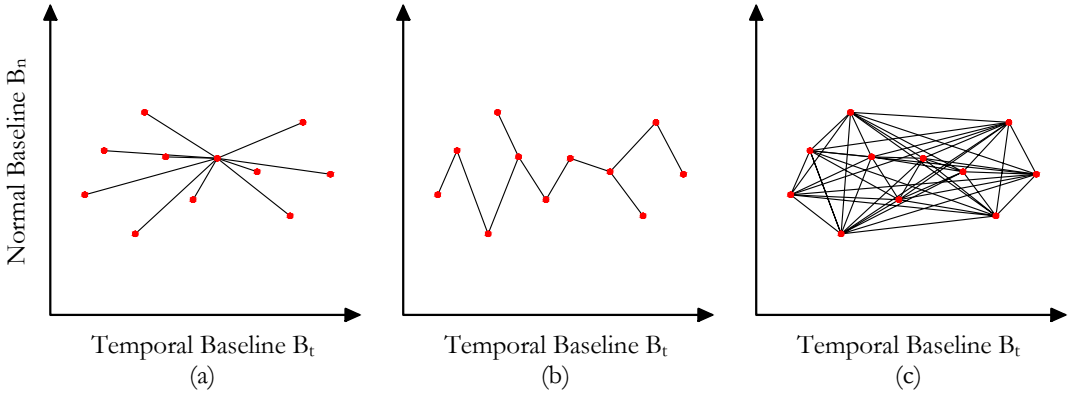


Figure 3.19: Types of connection graphs for interferograms generation.

represents the most exhaustive situation, involving a higher number of interferograms (Figure 3.19 (c)).

Interferogram generation usually comprehend the removing of the flat terrain phase component (see Section 3.2.3) and the topographic phase component (see Section 3.2.3), so that for the selected pixel the phase variation is expressed as follows (see Equation 3.25):

$$\Delta\phi_{PSI} = \Delta\phi - \Delta\phi_{flat} - \Delta\phi_{topo} = \Delta\phi_{displ} + \Delta\phi_{topo,res} + \Delta\phi_{atmo} + \Delta\phi_{noise} \tag{3.35}$$

Since we have generated M interferograms from N SAR images, in function of the connection graph used, we have for each pixel M phase variations. The PSI approach usually estimate the target motion with a linear function. Assuming a linear model for the target displacement, such as $d = \Delta v \cdot B_t$, the displacement phase component can be expressed as follows (see Equation 3.30):

$$\Delta\phi_{displ} = \frac{4\pi}{\lambda} \cdot B_t \cdot \Delta v = k_v \cdot B_t \cdot \Delta v \tag{3.36}$$

where k_v is a constant for the model, B_t is the independent variable (i.e. the temporal baseline) and Δv is the unknown of our problem. On the same logic, the residual topographic phase component can be expressed as follows (see Equation 3.27):

$$\Delta\phi_{topo,res} = \frac{4\pi}{\lambda \cdot \overline{KO} \cdot \sin\theta} \cdot B_n \cdot \Delta h_{res} = k_h \cdot B_n \cdot \Delta h_{res} \tag{3.37}$$

where k_h is a constant for the model, B_n is the independent variable (i.e. the normal baseline) and Δh_{res} is the unknown of the problem. With the last two equation is possible to retrieve the value of the two unknown, exploiting the periodogram function:

$$\gamma_u = \frac{1}{M} \cdot \sum_{j=1}^{M} e^{i\cdot(\Delta\phi_{PSI} - k_v \cdot B_t \cdot \Delta v - k_h \cdot B_n \cdot \Delta h_{res})} \tag{3.38}$$

here the value of γ_u can oscillate between the values of 0 and 1 based on the variables Δv and Δh_{res}. Here the goal is to maximise the value of γ_u, so that the values of Δv^* and Δh^*_{res} represent the best fit and therefore the solution of the problem:

$$[\Delta v^*, \Delta h^*_{res}] = argmax(\gamma_u) \tag{3.39}$$

The maximum absolute value of the periodogram is called temporal coherence γ_t (Perissin 2016):

$$\gamma_t = |\gamma_u(\Delta v^*, \Delta h^*_{res})| \tag{3.40}$$

Pixels that show high values of temporal coherence (e.g. higher that 0.8) indicate a strong fit with a linear variation of displacements. Conversely, pixels characterized by low temporal coherence should be disregarded, indicating either complete phase instability or a deviation from a linear displacement trend.

Nevertheless, the potential of this technique is not confined to these considerations. Some authors have pioneered the development of new algorithms capable of estimating atmospheric phase variations $\Delta\phi_{atmo}$ and effectively eliminating them from individual interferograms through the application of Atmospheric Phase Screens (APS) (Ding et al. 2008, Perissin, Rocca et al. 2011), thus improving the capability of PSI in detecting linear and non linear displacements.

3.2.5 Synthetic InSAR displacements from tunnelling

In Section 3.2.3, we discussed the displacement phase component $\Delta\phi_{displ}$ and highlighted its dependence on the displacement component d_{LOS} in the satellite line of sight (LOS) direction. Consequently, with a single acquistion geometry (i.e. ascending or descending) InSAR can provide information on displacements only along the LOS direction. Without knowledge of the actual direction of displacements, determining the true vertical and horizontal components from the LOS displacement is impossible.

In case of tunnelling, the interest is often directed toward the determination of ground vertical displacements (i.e. settlements). Under the assumption that ground displacements are predominantly vertical, the results of InSAR (d_{LOS}) can be converted in vertical displacements (Milillo et al. 2018, Giardina et al. 2019a, Macchiarulo et al. 2021), using the following equation:

$$d_v = \frac{d_{LOS}}{\cos\vartheta'} \tag{3.41}$$

Here, ϑ' represents the local incidence angle, which is the angle between the satellite line of sight direction and the vertical at the location of the target. Note that this differes from ϑ which denotes the satellite look angle (i.e. the angle between the satellite line of sight and the vertical at the location of the satellite).

It's worth noting that this assumption completely neglects the presence of horizontal displacements, while it is known that tunneling induces horizontal displacements as well. Consequently, it becomes important to carefully assess the implications of this assumption.

Considering the geometrical scheme of Figure 3.20 (a), where the tunnel cross section lies in the line of sight plane and the satellite is acquiring in ascending geometry, we can compute the intensity $p(x)$ and the direction $\alpha(x)$ (to the vertical, positive if anticlockwise) of the actual (theoretical) displacement vector $\overrightarrow{p}(x)$ using the following expressions:

$$|\overrightarrow{p}(x)| = p(x) = [w(x)^2 + u(x)^2]^{0.5} \tag{3.42}$$

$$\alpha(x) = \arctan\left(\frac{u(x)}{w(x)}\right) = \arctan\left(\frac{x}{z_0}\right) \tag{3.43}$$

Next, the intensity of the monitored displacements along the line of sight can be computed as:

$$d_{LOS}(x) = p(x) \cdot \cos\beta(x) = p(x) \cdot \cos(\vartheta' + \alpha(x)) \tag{3.44}$$

with $\beta(x)$ being the angle formed by the vectors $\overrightarrow{p}(x)$ and $\overrightarrow{d_{LOS}}(x)$. Finally, substituting Equation 3.44 into Equation 3.41, the converted displacement in the vertical direction is obtained as a function of the actual displacement intensity $p(x)$:

$$d_v(x) = p(x) \cdot \frac{\cos(\vartheta' + \alpha(x))}{\cos(\vartheta')} \tag{3.45}$$

By taking the ratio with $w(x)$, it is possible to assess the error $\psi(x)$ implied in the assumption of pure vertical displacements:

$$\psi(x) = \frac{d_v(x)}{w(x)} = 1 - \frac{x}{z_0} \cdot \tan\vartheta' \tag{3.46}$$

For a full demonstration on Equation 3.46, please consult Appendix A. From Figure 3.20, it becomes evident that for negative values of x (i.e., left side of tunnel axis), the error is $\psi(x < 0) > 1$, while for positive values of x, the error lies in the range $0 < \psi(x < 0) < 1$. In Figure 9a, a comparison between $w(x)$ and $d_v(x)$ is presented. It can be noted that, in the case of tunneling monitoring, the conversion of line of sight displacements to the vertical direction preserves the shape of the settlement profile (i.e. a Gaussian distribution). However, there is an overall increase in magnitude and a shift toward the satellite of the settlement trough.

The quantification of the maximum settlement's increment is explicated through the expression $\psi|_{max} = \max d_v(x) / \max w(x)$. Its determination relies exclusively on the local angle of incidence ϑ' and the geotechnical parameter k, as shown in Figure 3.21 (a). The shift of the maximum settlement Δx_v depends on the local incidence angle, the geotechnical parameter k and the tunnel axis depth z_0, as shown in Figure 3.21 (b). The shift is determined using the following equation:

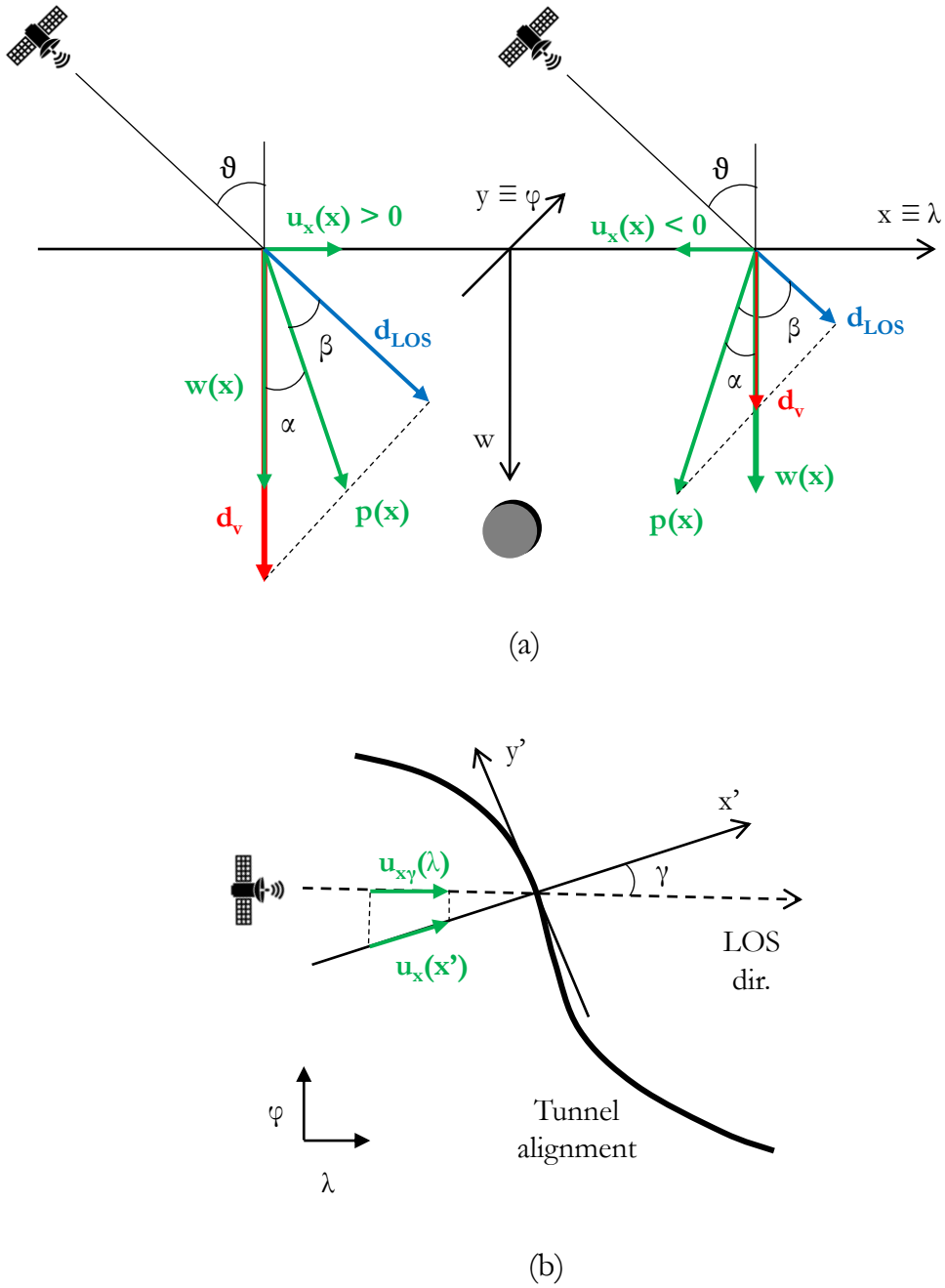


Figure 3.20: (a) Influence of horizontal displacements on the assumption inherent in Equation 3.41, under the assumption that the cross section is contained in the LOS plane. (b) Effect of the angular deviation γ between the cross-sectional plane and the line-of-sight plane on the magnitude of horizontal monitored displacements.

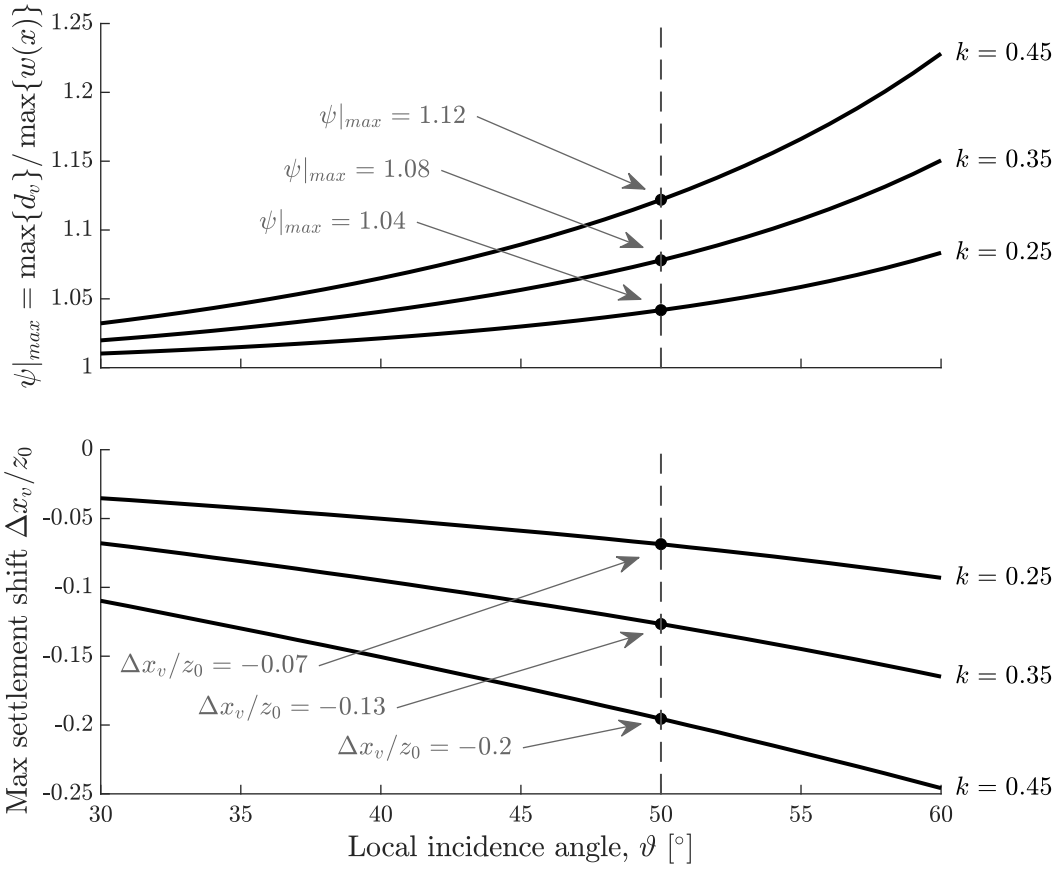


Figure 3.21: (a) Amplification factor of settlement peaks as a function of the local incidence angle ϑ' and the geotechnical parameter k. (b) Maximum settlement shift as a function of the local incidence angle ϑ' and the geotechnical parameter k.

$$\Delta x_v = 0.5 \cdot \cot \vartheta' \cdot z_0 \cdot (-1 - \sqrt{1 + 4 \cdot \tan^2 \vartheta' \cdot k^2}) \tag{3.47}$$

For a full demonstration on Equation 3.47, please refer to Appendix A.

Thus, when converting the LOS monitored displacements into vertical settlements, the presence of horizontal displacements modifies the expected settlement profile shape according to the following equation, keeping in mind Equation 3.46 and Equation 2.7:

$$d_v(x) = \psi(x) \cdot w(x) = \left(1 - \frac{x}{z_0} \cdot \tan \vartheta'\right) \frac{0.31 \cdot V_L \cdot D^2}{i_x} \cdot e^{-x^2/(2 \cdot i_x^2)} \tag{3.48}$$

Hence, $\psi(x)$ can be seen as a modification function to be applied to the classic Gaussian curve, and Equation 3.48 will be used in Section 4 to predict the settlement profile. It is possible to demonstrate that the volume loss obtained from the function in

Equation 3.48 is equal to the actual volume loss V_L in Equation 2.7 (see Appendix A). Consequently, for tunneling applications, the assumption of pure vertical displacements does not have any influence on the detection of volume loss via SAR remote sensing, but it has an influence on the location and magnitude of the settlement profile.

If the cross section is not contained in the LOS plane (Figure 3.20 (b)), then it is necessary to use the horizontal displacement component in the LOS direction $u_{x\gamma}(\lambda)$, so that:

$$u_{x\gamma}(\lambda) = u_x(x') \cdot \cos\gamma \tag{3.49}$$

where λ is the abscissa parallel to the LOS direction, x' is the local abscissa, and γ is the angle formed by the tunnel cross section and the LOS direction. The presence of angle γ reduces the magnitude of $\psi|_{max}$ and Δx_v.

Chapter 4

Applications and results

4.1 Fibre optic sensing

4.1.1 Validation of numerical results

The main results from PIV analyses consist in the displacement fields above the trapdoor. In Figure 4.1(c) and (d) are shown the experimental and numerical contour plots of displacements, together with the deformed shape of the experimental and numerical soil body in (a) and (b) respectively, for a relative density of D_R=52% and a trapdoor displacement of δ=2 mm. This comparison is needed to validate the numerical model in Figure 4.1(b). The observed trends show good agreement in the development of the mechanism, confirming the adequateness of the numerical model in capturing the soil behaviour.

Moreover individual layers are analysed more closely. The settlement profiles $S_v(x)$ is fitted using a modified Gaussian distribution following recommendations by Da Silva Burke 2018 and Möller et al. 2023. Horizontal soil displacements $S_h(x)$ from PIV are interpolated using a double Gaussian distribution to obtain the displacement profiles from PIV shown in Figure 4.2. Detail on the processing method is provided in depth in Möller et al. 2023. The experimental data are compared with the numerical results, showing good agreement and thus validating the numerical model. It is important to note the difference in magnitude between horizontal and vertical displacements obtained in both the experimental and numerical cases.

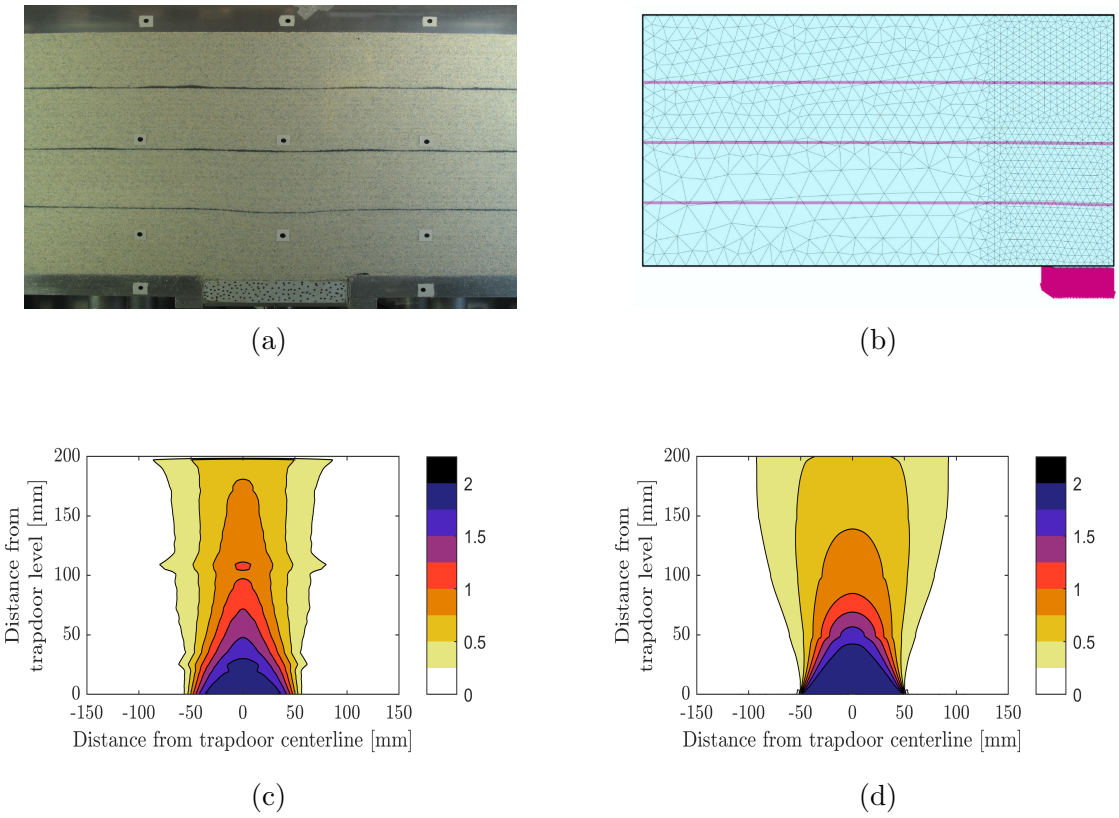


Figure 4.1: (a) Image acquired from the Canon Powershot G10, used for PIV analysis. (b) Numerical half-space deformed mesh. (c) Experimental contour plot of vertical displacements from PIV. (d) Numerical contour plot of vertical displacements (D_R=52% δ=2 mm).

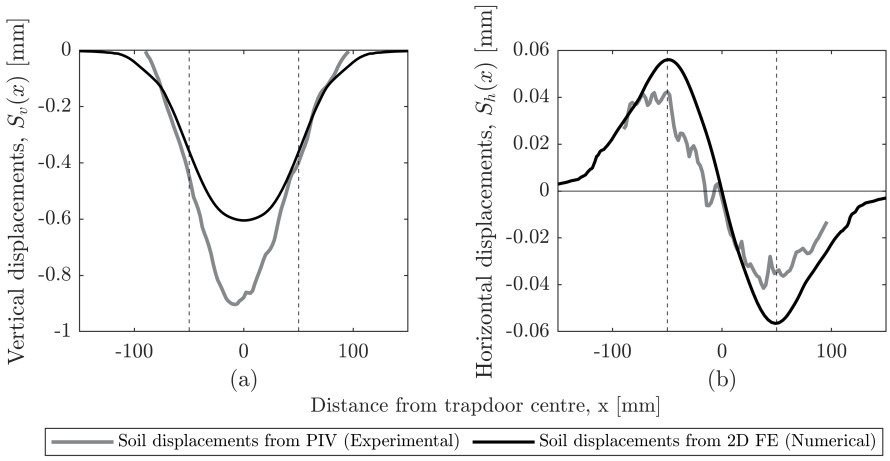


Figure 4.2: (a) Vertical displacements from PIV and numerical results. (b) Horizontal displacements from PIV and numerical results. (D_R=52% δ= 2 mm and z=150 mm).

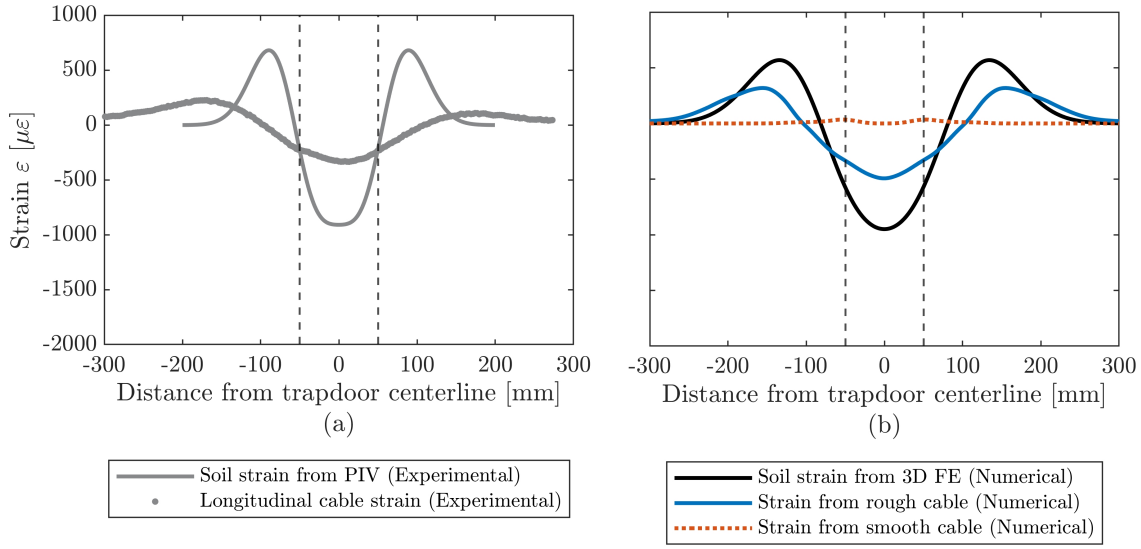


Figure 4.3: (a) Soil strain from PIV and strain within the fibre optic cable. (b) Numerical horizontal soil strain, rough and smooth cables numerical strain. (1g test, D_R=52%, δ=2 mm and z=150 mm).

To deepen this observation, the numerical analyses were validated against the experimental measurements of soil deformation and fibre optic strain profiles for small trapdoor displacements (Figure 4.3), representative of the stable arching phase, and equal to a trapdoor displacement of 1-2% of its width (i.e. $\delta = 1 - 2$ mm, since B=100 mm). Any deformation beyond δ =2 mm is numerically costly and hence was not considered here.

In the Figure 4.3 it is evident that both the experimental results and the numerical model indicate that the fiber optic cable undergoes less deformation than the surrounding soil. Furthermore, the use of numerical 3D Finite Element Analysis (FEA) enables an exploration of the behavior at the soil-cable interface. This analysis reveals that the deformation profile observed in the experimental fibre optic cable closely aligns with that of the simulated rough cable rather than the smooth one.

For consistency with the procedure adopted in the experiments (Möller et al. 2023), the strain profiles for the soil and the modelled cable in Figure 4.3 were obtained according to the following equation and schematised in Figure 4.4:

$$\varepsilon_{u,tot} = \frac{\sqrt{(\Delta X_i + u_{x,i+1} - u_{x,i})^2 + (u_{y,i+1} - u_{y,i})^2}}{\Delta X_i} - 1 \tag{4.1}$$

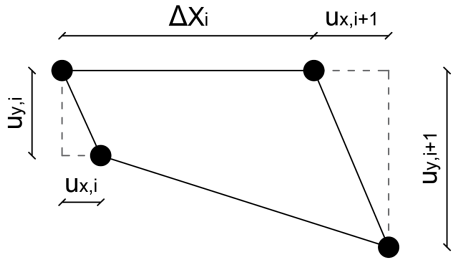


Figure 4.4: Geometry for strain calculation

Here, $\varepsilon_{u,tot}$ represents the strain resulting from both vertical u_y and horizontal u_x movements, with ΔX denoting the distance between the two ends of the segment over which the strain is to be computed.

4.1.2 Results of small scale tests

The numerical analysis offers the advantage of isolating the strain components induced within the cable by exclusively horizontal or vertical movements, a capability not achievable through the experiments, since the output from the fibre optic interrogator can only be converted in logitudinal strain (i.e. those corresponding to Equation 4.1). The strain components induced solely by horizontal or vertical components can be computed as follows:

$$\varepsilon_{u,y} = \frac{\sqrt{\Delta X_i^2 + (u_{y,i+1} - u_{y,i})^2}}{\Delta X_i} - 1 \tag{4.2}$$

$$\varepsilon_{u,x} = \frac{u_{x,i+1} - u_{x,i}}{\Delta X_i} \tag{4.3}$$

Therefore, while Equation 4.1 evaluates the strains induced by both vertical and horizontal movements, Equations 4.2 and 4.3 identify the strains induced by vertical and horizontal movements, respectively. This distinction aids in determining which displacement component has a more pronounced impact on the strain within the cable induced by subsidence.

In Figure 4.5 a comparison of the experimental soil strain profiles with the corresponding numerical results is provided for test D_R=20%, and strains are evaluated with Equations 4.1, 4.2 and 4.3 (in Figure 4.5 (c), (b) and (a) respectively). The scatter

points are the raw experimental results from PIV data processing. These data have been interpolated (black line) using a modified Gaussian for vertical movements (Möller et al. 2023) and a double standard Gaussian for horizontal movements. The convention chosen in the figure is such that a dashed line represents the experimental results from Möller et al. 2023, while a solid line represents the numerical data. The shape and magnitude of the strain profile between the experimental and numerical results shows good agreement, particularly for strains induced by vertical movement. For the strains induced by horizontal movement, the general shape is similar, although the magnitudes of the numerical results are approximately half the experimental results. The y-axes show that the strain induced by the vertical soil movements are more than one order of magnitude lower compared to those induced by horizontal movements. Horizontal movements induced by the trapdoor vertical movement thus played a major role in the measured horizontal strain profile.

On the fibre optic cable side, the numerical strain profiles computed from cable movements using Equations 4.1, 4.2 and 4.3 are plotted in Figure 4.6 (c), (b) and (a) respectively, and are compared with the experimental data, directly measured by the fibre optic interrogator (i.e. Luna analyser). The results are consistent with what has been observed for the soil strains. The comparison shows that for small trapdoor displacements (i.e. δ =1 mm), strains within the cable far above the trapdoor (i.e. z=150 mm) are induced by horizontal movements mainly.

Therefore, it can be assumed that during a subsidence event, the horizontal movements governs the strain within the cable. The horizontal strain profile induced in the soil and in the cable by horizontal movements (the contribution of vertical strains is negligible in comparison to the horizontal strains) is shown in Figure 4.7 and Figure 4.8, respectively, for a trapdoor displacement of δ =1 mm, for three different relative densities of soil and at three different distances above the trapdoor level. The comparison between experimental and numerical soil strains in Figure 4.7 shows a good agreement in terms of strain magnitude, with both results indicating that the magnitude reduces with increasing relative densities and distance from trapdoor level. This also provides a good validation of the soil model employed here for low confining stresses. Figure 4.8 shows a reasonable agreement between the profile and magnitude of the nu-

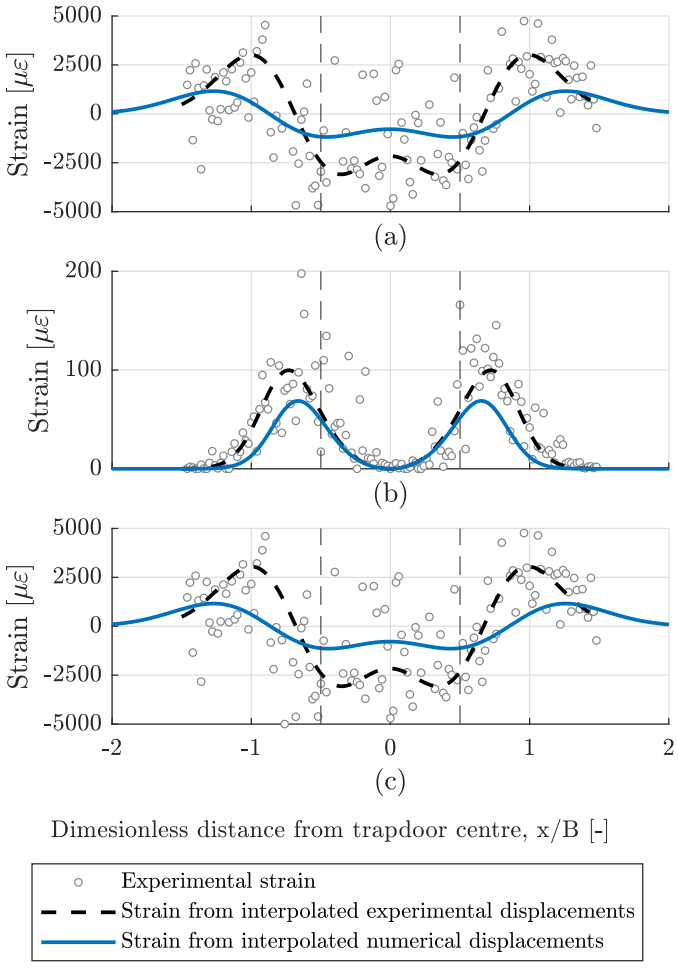


Figure 4.5: Comparison between soil strains induced by (a) horizontal, (b) vertical and (c) total displacement in the $1g$ experimental results and numerical analysis of the laboratory test, far from the cables (D_R=20%, δ=1 mm, z=150 mm).

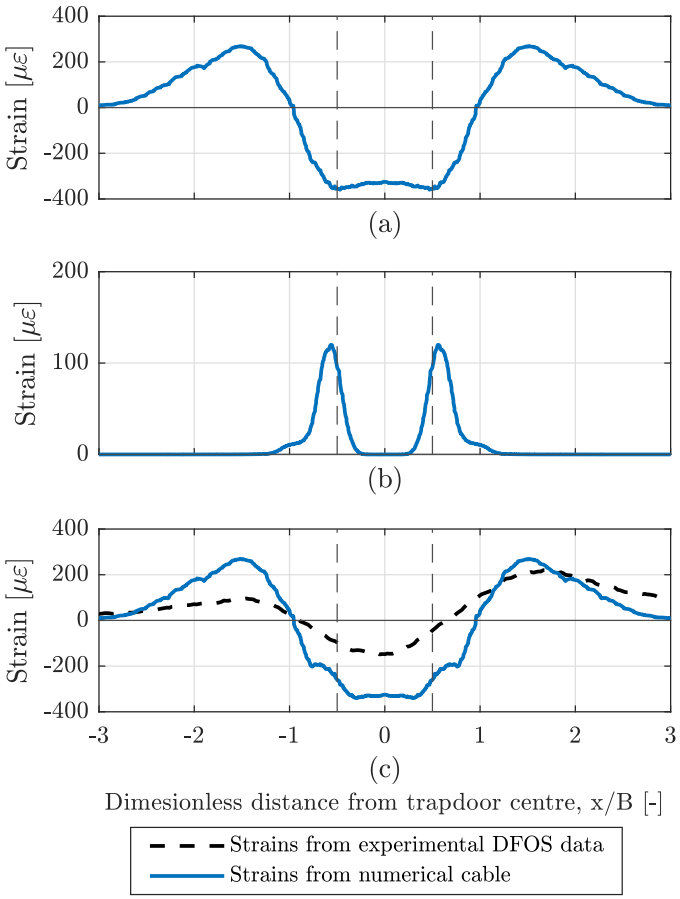


Figure 4.6: Comparison between cable strains induced by (a) horizontal, (b) vertical and (c) total displacements in the 1g experimental results and numerical analysis of the laboratory test (D_R=20%, δ=1 mm, z=150 mm, rough cable).

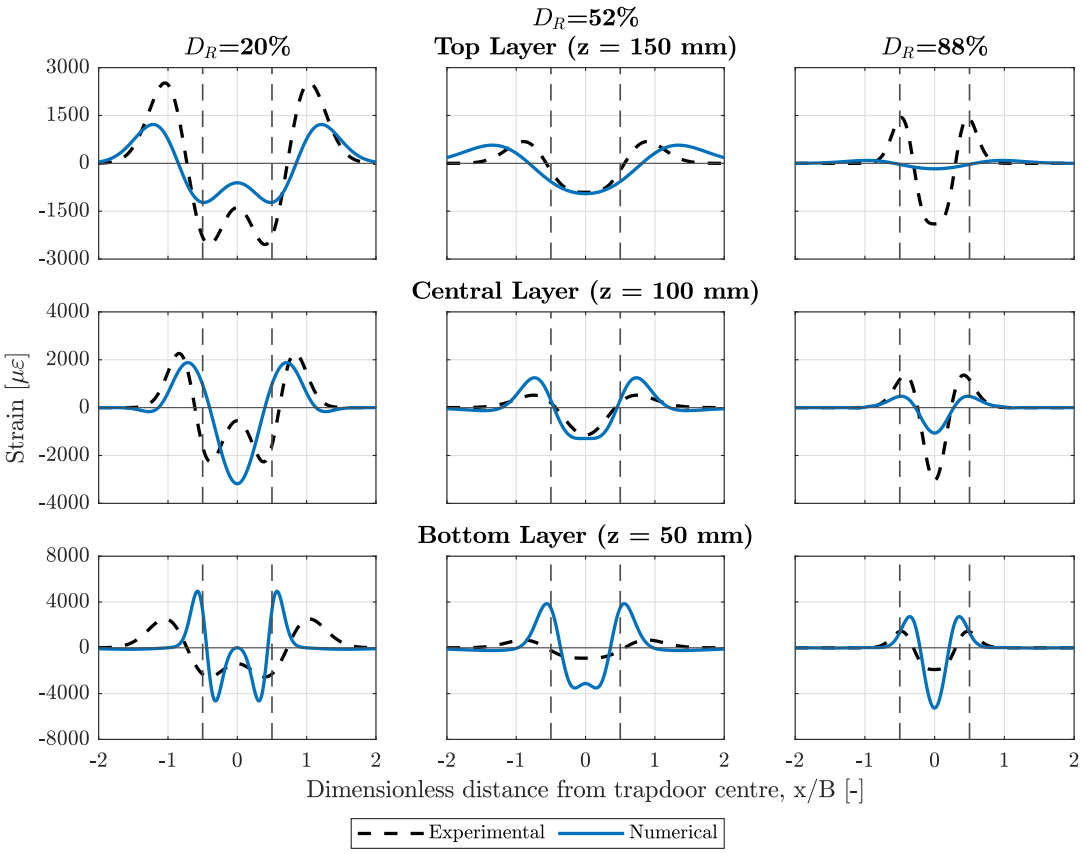


Figure 4.7: Comparison between soil strains from horizontal movements at different densities and at three heights in the soil body in the $1g$ experimental results and numerical analysis of the laboratory test, far from the cables (δ=1 mm).

merical and experimental cable strain for all distances from the trapdoor and all relative densities. This confirms the significant difference in strain magnitude between the cable and the soil noted by Möller et al. 2023, where it was observed that DFOS cable strain was approximately an order of magnitude lower than the corresponding soil strain determined from PIV. In particular, the shape, location of the peaks and magnitude matches well. This provides confidence that the model can be used to further analyse and understand the experimental tests performed by Möller et al. 2023, and potentially shed some light on the soil cable interface to further explain this difference in strain magnitude.

The soil-cable interface was investigated through modelling of two conditions: a smooth cable with $R_{inter} = 0.01$, and a rough cable with $R_{inter} = 1$ (Equation 3.12). Figure 4.9 illustrates the horizontal and vertical movements of both a smooth and a

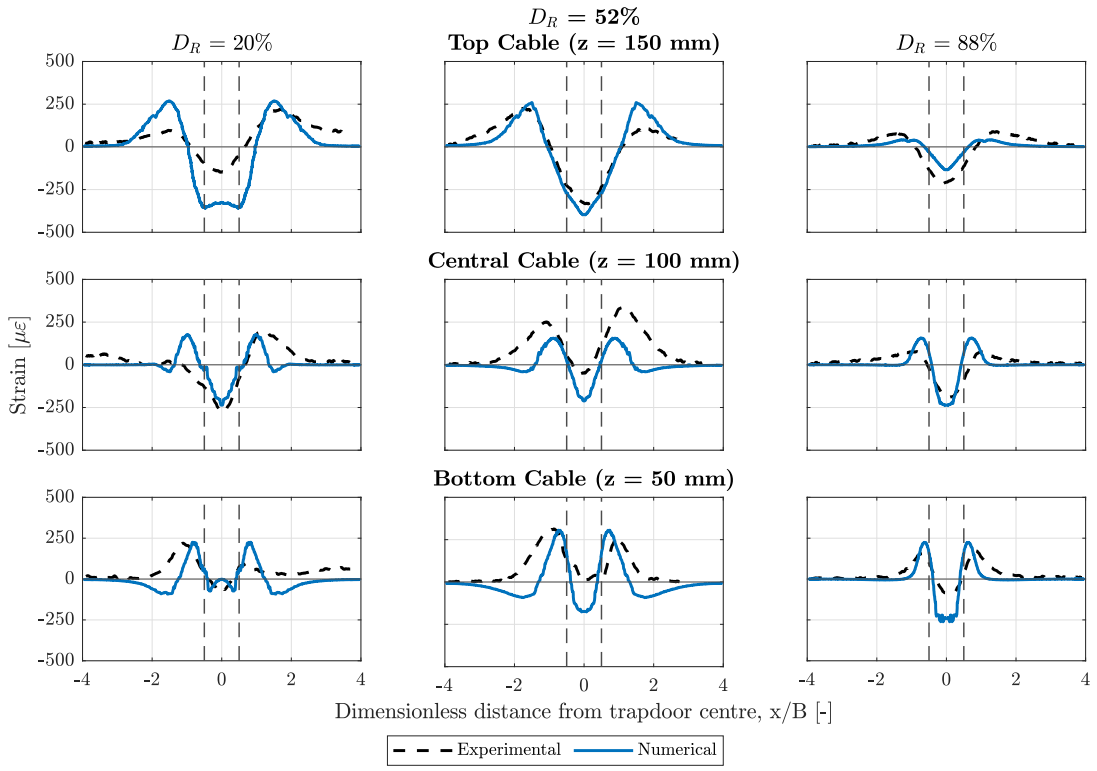


Figure 4.8: Comparison between horizontal cable strains at different densities and at three heights in the soil body in the $1g$ experimental results and numerical analysis of the laboratory test, rough cables (δ=1 mm).

rough cable for D_R=52% and δ=1 mm. The results reveal that the interface primarily affects horizontal displacements, having minimal impact on vertical displacements. This suggests that, for a smooth cable, one should anticipate very small strains, as horizontal movements predominantly drive most of the deformation (see Figure 4.6).

Further analysis of the numerical model, particularly the soil strain field around the cable, indicates that the simulated soil-rough cable interface allows only limited relative displacement between the soil near the cable and the cable itself, particularly for the top cable (Figure 4.10 (a)). This capability enables the replication of experimental cable strain profiles. However, in the central and bottom layers, the magnitude of the cable's strain profile is significantly lower than that of the surrounding soil (Figure 4.10 (b) and (c)). It's noteworthy that PIV records soil strain data away from the cables, so that they can be virtually compared with the strains in Figure 4.10 indicated using a solid blue line. These strains are higher than those experienced by the soil near the cable, indicating that the stiffness of the cable influences the surrounding soil at these low confining pressures.

Therefore, the numerical results retrieve the difference of an order of magnitude observed experimentally between DFOS cable strains and PIV soil strains by Möller et al. 2023.

The observed magnitude disparity between the strain experienced by the fibre optic cable and that within the soil poses a potential challenge in utilizing this technology for detecting strain induced by tunnel excavation. It's noteworthy, however, that in these small-scale experiments, the confining pressure around the cables is lower than 2 kPa. This lower confining pressure significantly diminishes the effectiveness of the shear transfer mechanism, and it is evident that these conditions may not fully represent the real-world scenario. To gain a more comprehensive and realistic understanding of the application of this technology in field-scale scenarios, a full-scale numerical analysis is needed. Such an analysis can provide insights into how the technology performs under conditions more representative of actual subsidence scenario.

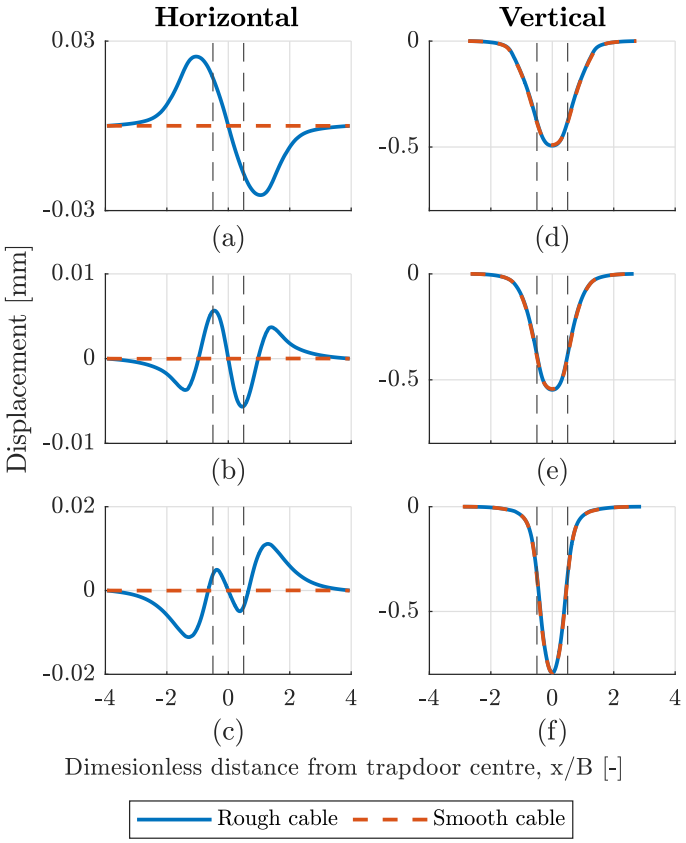


Figure 4.9: Horizontal and vertical displacement of numerical cables for D_R=52% and δ=1 mm, comparison between rough and smooth cables. (a), (d) Top cable; (b), (e) central cable; (c), (f) bottom cable.

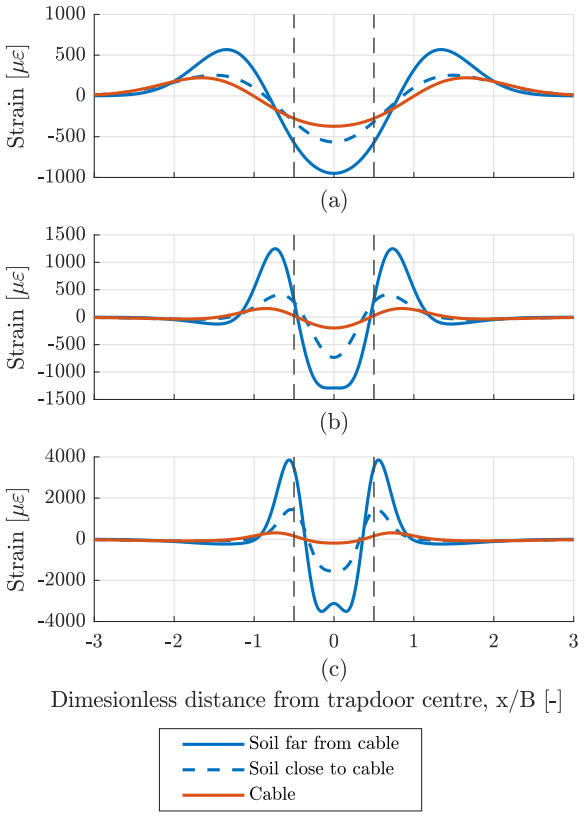


Figure 4.10: Strain induced by horizontal movements for D_R=52% and δ=1 mm, comparison between soil's strain (far from and close to the cable) and the rough cable for: (a) top layer and top cable; (b) central layer and central cable; (c) bottom layer and bottom cable.

4.1.3 Large scale application

Plane strain conditions

Despite providing valuable insight regarding the DFOS behaviour, the low stress level in the experiments conducted by Möller et al. 2023 is actually one of the key limitations of the work. Although careful consideration was given to the scaling laws, the results cannot be used to directly predict the behaviour at full scale, in particular the quantitative response. For this, tests at enhanced gravity in the centrifuge would be needed. However, as mentioned by Möller et al. 2023 and Eichhorn 2023, it is not currently possible to use the fibre optic analyser needed in the geotechnical centrifuge. To verify the robustness of the methodology at realistic stress levels, a 3D FE model of the centrifuge test from Da Silva Burke 2018 was performed, adding embedded fibre optic cables for analyses.

The numerical model was created at prototype scale, reproducing a 2 m trapdoor width in plane-strain conditions, located 4 m below the ground level in a cohesionless sand at D_R=87.5%. Using the framework established by Möller et al. 2023, the early stage of the subsidence formation corresponds to a trapdoor displacement of δ=40 mm, that is, 2% of the trapdoor width. The material model used is the HSSmall model, and its parameters are indicated in Table 3.3. Figure 4.11 shows the comparison between the experimental and numerical ground surface settlement profiles. The shape of the ground settlement profile is well captured, with an overestimation of the magnitude of about 25%. This is because the material model does not enable a variation of dilation angle within the model and a constant dilation angle had to be used, evaluated here at the trapdoor level. In the centrifuge model, however, this dilation angle reduces with overburden pressure, and therefore the numerical model has a lower dilatancy compared to the centrifuge test at the soil surface, which leads to larger settlements. However, this is sufficient here to have a good estimate of the expected subsidence behaviour at realistic stress levels.

Figure 4.12 shows the cable strain profiles obtained for this model, as well as the strain caused by horizontal and vertical movements. Figure 4.12 only displays the results for the top cable, as it is the location of practical interest for this study. The cases of rough and smooth cables are considered, showing similar results to those observed

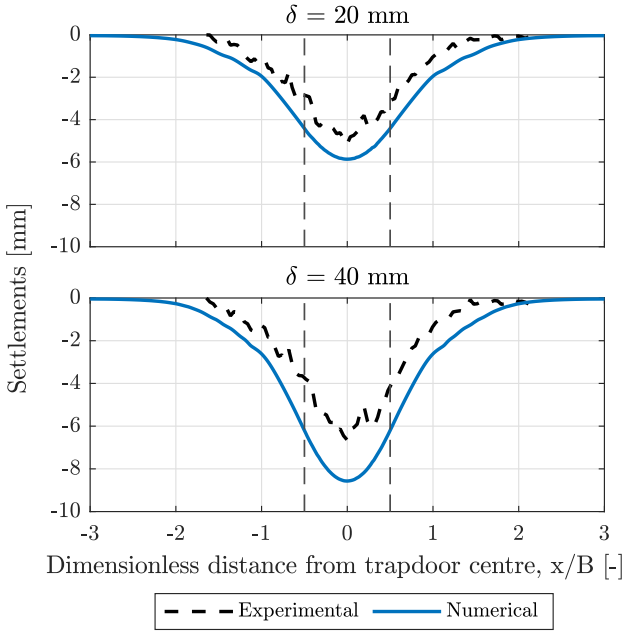


Figure 4.11: Comparison between centrifuge experimental and numerical surface soil settlement profiles.

previously for the 1g tests for the rough cable. Horizontal displacements are governing the strains within the cable. This figure also shows that the strains generated by the horizontal movements are not equal to zero for the smooth cable, confirming that at higher confining stresses, enhanced coupling between the soil and the cable enables the cable to move horizontally with the soil better.

The results from the 3D FE analyses at both $1g$ and $40g$, as well as the experimental data, demonstrate the importance of the horizontal soil movements in the ability of the DFOS to identify the presence of an active subsidence at depth. These results indicate that the better the soil cable coupling, the more precise the results, because the cable is then more able to deform horizontally with the soil. These results confirm that improving the soil cable coupling increases the ability of the cable to deform horizontally with the soil. Therefore, it is important to use in practice elements that can be horizontally deployed and have higher surface area, in order to increase the amount of shear transferred at the interface. This would, however, constrain the cable horizontally and therefore prevent this movement.

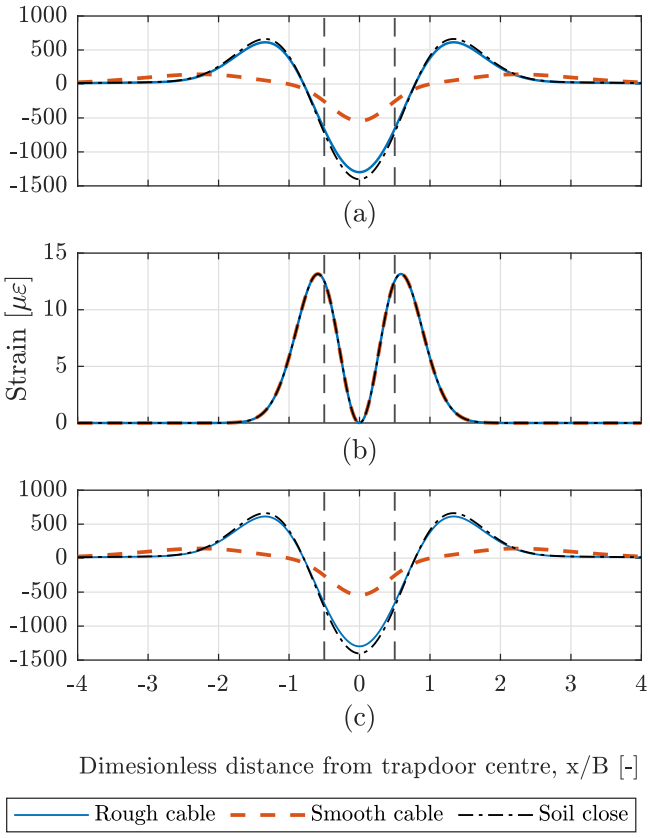


Figure 4.12: Comparison between rough and smooth cable, top cable δ=40 mm: (a) strains induced by horizontal displacements; (b) strains induced by vertical settlements; (c) total strains induced by horizontal and vertical displacements.

Axialsymmetric conditions

This subsection serves as a natural extension of the primary investigation, aiming to address and expand upon certain limitations. Initially, a rectangular trapdoor was employed to simulate plane strain conditions, which are effective at a specific distance from the excavation face. However, it's recognized that in cases of localized subsidence, such as that induced by the softening of a tunnel section over its lifetime, plane strain conditions become less effective. To account for this, axially symmetric conditions were assumed, acknowledging the limitations of plane strain conditions.

One crucial limitation of the previous work is the 2D nature of the plane strain conditions, which naturally enforces the cable to be directly above the centre of the trapdoor/subsidence. The uncertainty arises when considering scenarios where the cable is positioned eccentrically compared to the center of subsidence or even beyond the width of the trapdoor. To explore these scenarios, the calibrated numerical model from the preceding section was extended to incorporate a 3D circular trapdoor, as illustrated in Figure 4.13.

In this expanded model, a series of cables were strategically placed for analysis. Initially, cables were positioned directly above the trapdoor center (y/D=0) for comparison with the 2D experiments. Subsequent configurations involved eccentric placements, such as at y/D=0.25 from the center, at y/D=0.50 on the edge of the trapdoor, and at y/D=0.75, 1.00, 1.50, and 2.00 outside the trapdoor (Figure 4.13).

The test very much corresponds to one of the centrifuge tests performed by Da Silva Burke 2018, but is here extended to a 3D circular trapdoor, schematised in axisymmetric conditions, so for the material model parameters one can refers to Table 3.3. Figure 4.14 (a) shows the settlement profile obtained for a soil layer located 1 m below the soil surface. This is compared with the settlement profile derived from the grid of fibre optic cables, shown in Figure 4.14 (c), for a trapdoor displacement of δ=40 mm.

The strain profiles recorded within the cables for $\delta = 40$ mm are depicted in Figure 17. In this set of plots, the strain profiles from the bottom cable for $y/D = 1.00, 1.50$, and 2.00 (Figure 17 (f), (g), and (h)) essentially register values close to zero, with magnitudes less than 1 microstrain. Therefore a 0 horizontal line was used for clarity. The results show a clear drop of strain magnitude at y/D=0.50, and an even larger drop

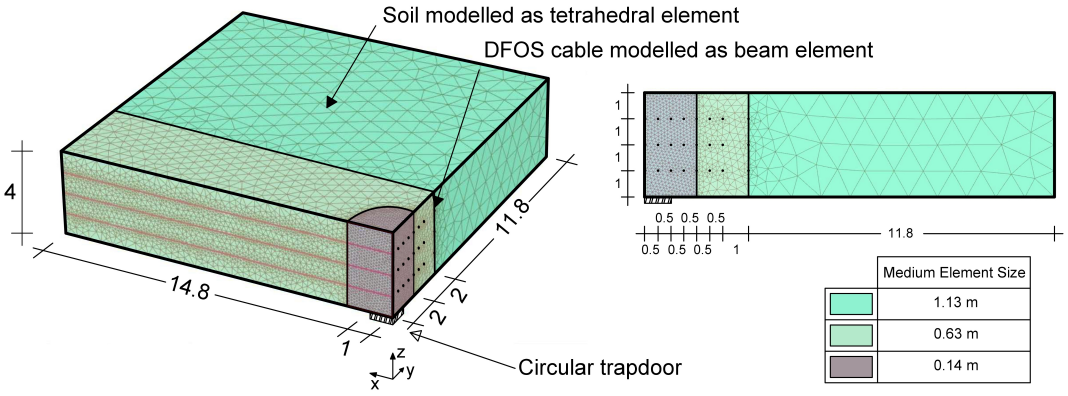
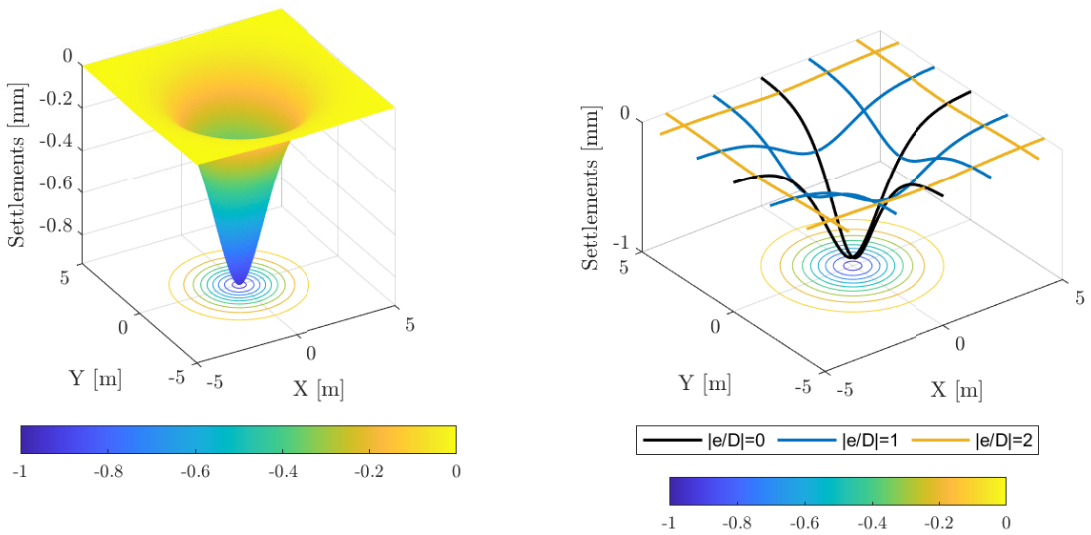


Figure 4.13: Plaxis 3D numerical model representing a quarter of the axisymmetric problem with soil modelled as tetrahedral element and fibre optic cable modelled as an embedded beam element ($15.8 \times 15.8 \times 4$ m). Dimensions in meters.



(a) (b)

Figure 4.14: (a) Soil settlements at z=3 m above circular trapdoor. (b) Rough cables settlements at z=3 m above circular trapdoor. (δ=40 mm).

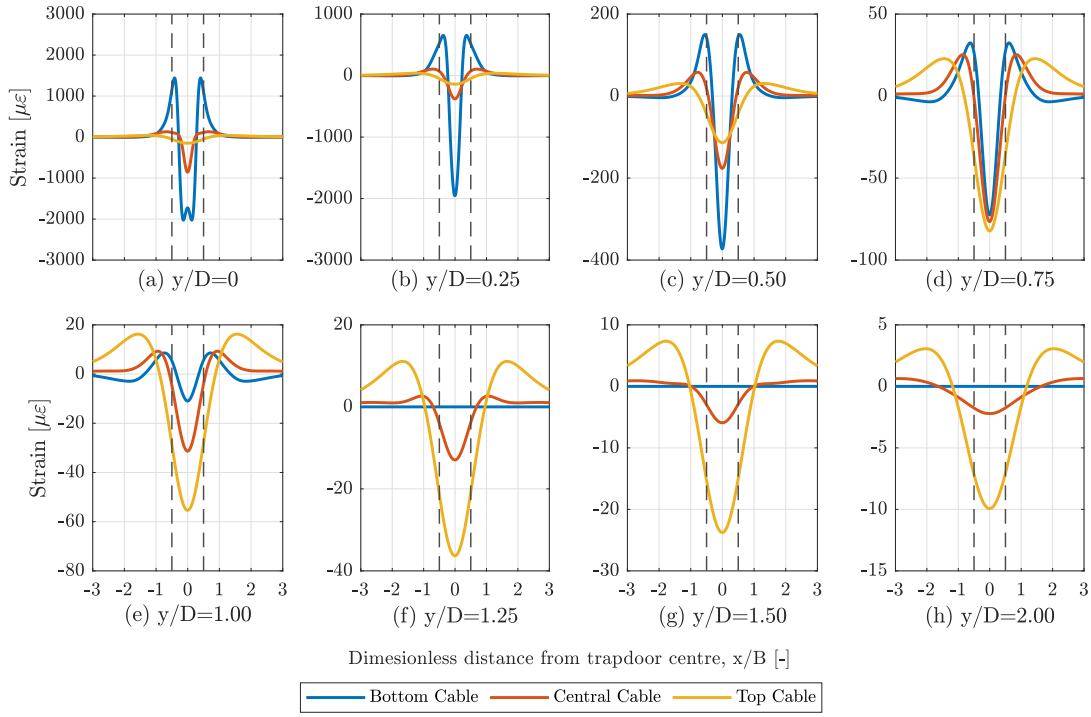


Figure 4.15: Horizontal strain profiles within the cable in axial symmetric conditions for δ=40 mm: (a) $y/D = 0$; (b) y/D=0.25; (c) y/D=0.50; (d) y/D=0.75; (e) y/D=1.00; (f) y/D=1.25; (g) y/D=1.50; (h) y/D=2.00.

for y/D=0.75, which might not be measurable in practice. The results also illustrate that cables located close to the soil surface, but away from the immediate zone above the subsidence formation, benefit from the funnel shape of the deformation mechanism. Clearly, if the cable is located anywhere directly above the trapdoor (here, y/D=0.00, 0.25, 0.50, 0.75), the lower the cable is, the more clearly it senses the displacement induced by the trapdoor. However, cables located horizontally away from the trapdoor footprint (y/D=0.75) will be able to sense ground deformation when placed relatively close to the soil surface if they are within the funnel mechanism generated by the subsidence expansion, and therefore are deformed by the horizontal soil movement within that zone.

4.2 MT-InSAR - Naples

4.2.1 Introduction

The city of Naples lies on the west coast of the Italian peninsula, about 200 km south-east of Rome. With a population of almost a million, it is the third largest city in Italy after Rome and Milan. Its prominent position on the coast of the Mediterranean Sea, flanked by natural and historical beauties and a warm climate, make it one of the most attractive destinations for tourists during the summer season, with peaks reaching 3.7 million tourists (ISTAT 2022). Many arriving by air transportation must connect through the only airport in the city, named as Capodichino Airport. The latter is located in the north-east area of the city (see Figure 4.16), about 4 km away from the city center, and currently it is connected only by road transport to the urban center.

Commuters are limited to road transport and are subjected to daily heavy traffic. Therefore, to increase mobility between the airport and the city center, the City Council of Naples decided to contract out the extension of the existing Line 1 (Figure 4.17 (a)) of the metro system, thus connecting the main train station to Capodichino Airport. Two tunnels, one for each direction, were designed along the stretch between the two

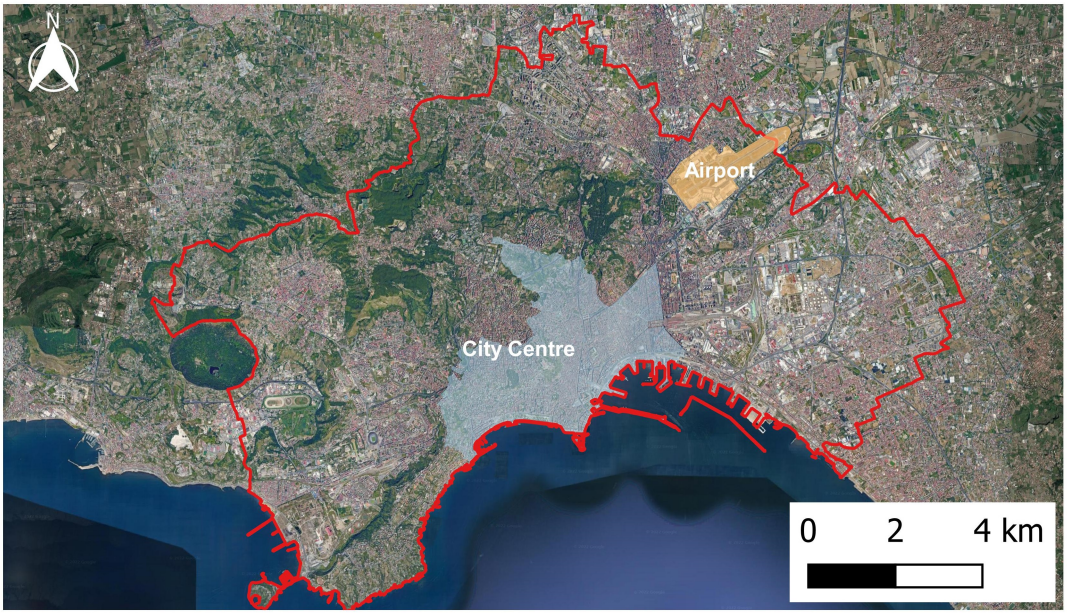
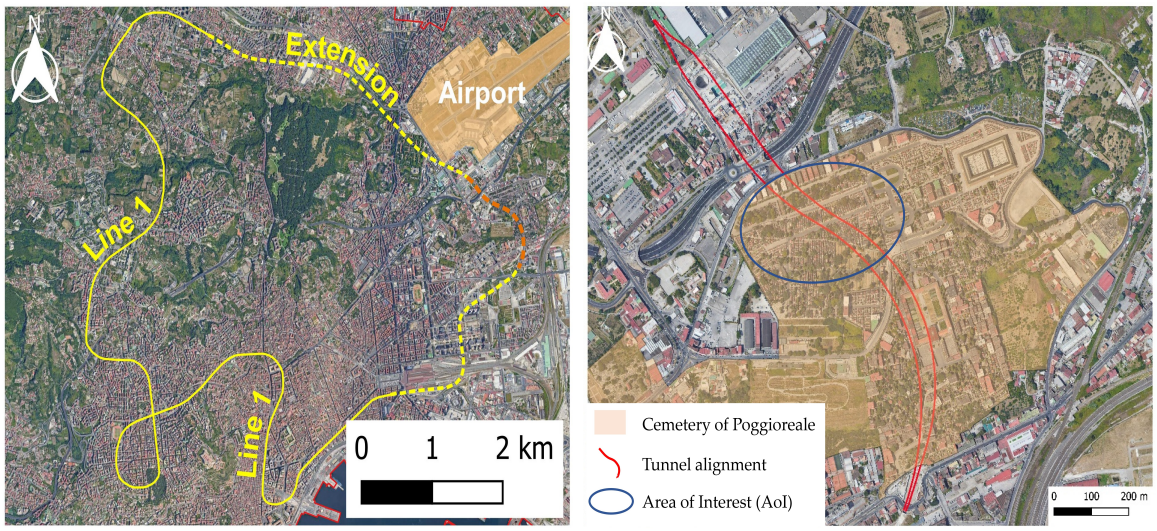


Figure 4.16: City of Naples, Italy. Highlighted in blue is the city center and in orange is the airport of Capodichino. The red solid line represents the city bounds. (Image modified after Google Earth©, Google)



(a) (b)

Figure 4.17: (a) Metro Line 1 of the city of Naples. The existing line is represented with a continuous line, while the extension is represented with a dashed line. In dashed orange the segment Capodichino-Poggioreale. (b) Google Earth map of the Area of Interest (in blue). Red lines represent the longitudinal axes of the excavated tunnels (after [24]). In orange the cemetery of Poggioreale. (Image modified after Google Earth©, Google)

upcoming metro stations of Capodichino and Poggioreale (Figure 4.17 (b)).

4.2.2 Excavation details and geological conditions

Along the stretch between Capodichino and Poggioreale, two tunnels were designed, one for each way, between the two upcoming metro stations of Capodichino and Poggioreale (Figure 4.17 (b)). The excavation of the first tunnel started from the shaft at Capodichino in July 2020 (MN 2020) and ended on March 30th 2021 (MN 2021). The length of the excavation is roughly 1.000 m per tunnel and it was performed using a Tunnel Boring Machine (TBM) with a cutterhead of 7 m in diameter, mainly in soft rock layer (*Campanian Ignimbrite*) covered by sandy and silty sand deposits (*Pozzolana*) (Di Pace, Cocchi and De Gugliemo 2021). The excavation of the first tunnel started 40 m below ground level from the shaft made for Capodichino station and arrived at Poggioreale station at 10 m below ground level (MN 2020, MN 2021). The TBM was then disassembled and moved back to the Capodichino shaft, and used for the excavation of the second tunnel.

As one might expect, both tunnels are excavated within the *Campanian Ignimbrite* formation (developed during the Campanian Ignimbrite eruption, attributed to the caldera of the Phlegraean Fields 40.000 years ago) which is a highly variable soft rock. In Figure 4.18 is reported the geological section interested by the twin tunnels excavation.

Starting from Capodichino station and descending towards the base of Poggioreale hill, the different materials encountered at the excavation level of the tunnel include *Campanian ignimbrite* with varying degrees of cementation, subjected to a covering that can be attributed to subsequent eruptions, ultimately reaching the period of the *Neapolitan yellow tuff* (i.e., 35.000 to 12.000 BC). The stratigraphic sequence is concluded by loose materials such as pyroclastic deposits, which, in some vertical sections, can assume significant thicknesses and occupy the first 5/10 meters. Overall, above the *Campanian Ignimbrite*, there is a covering of pyroclastic material, with thicknesses on the order of several tens of meters, often in loose conditions or with modest cementation bonds. Throughout this initial stretch, the tunnels are well above the water table, ensuring dry excavation. The stratigraphic model at Capodichino

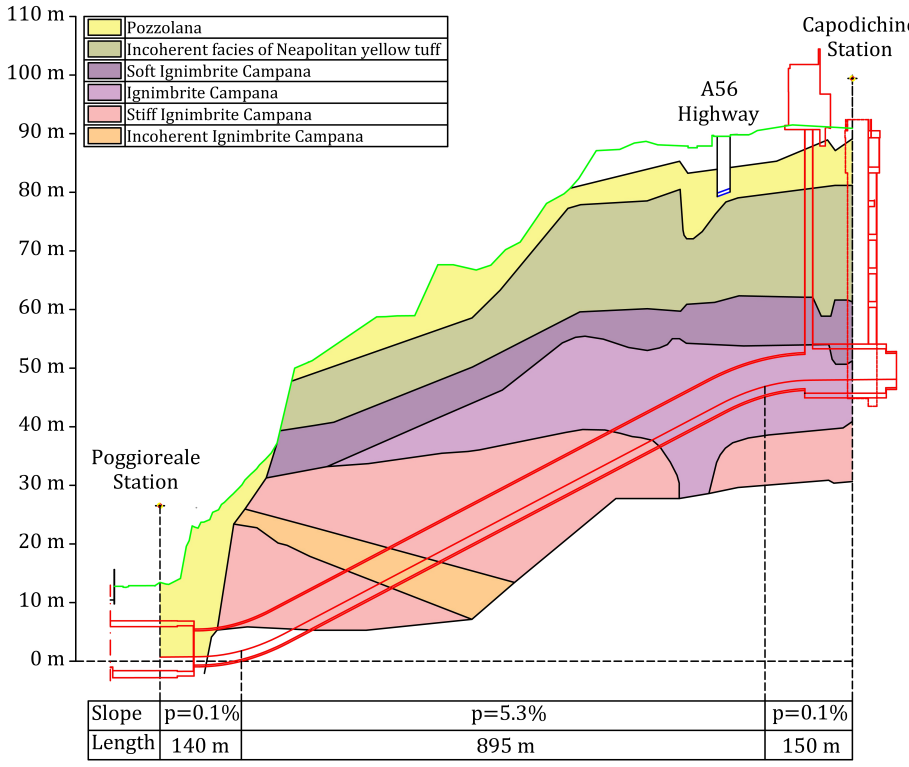


Figure 4.18: Geological section between Poggioreale and Capodichino stations

Table 4.1: Stratigraphic model for the station of Capodichino (modified after Regione Campania 2013).

Layer	Depth [m]	E_0 [MPa]	c [kPa]	ϕ [°]	γ [kN m^{-3}]
Backfill, pumices and ashes	0-9	150	15	32	16
Pozzolana and Neapolitan yellow tuff	9-27	300	16	32	16
Soft Ignimbrite Campana	27-36	400	16	35	16
Ignimbrite Campana	36-60	1000	21	35	16

station is reported in Table 4.1.

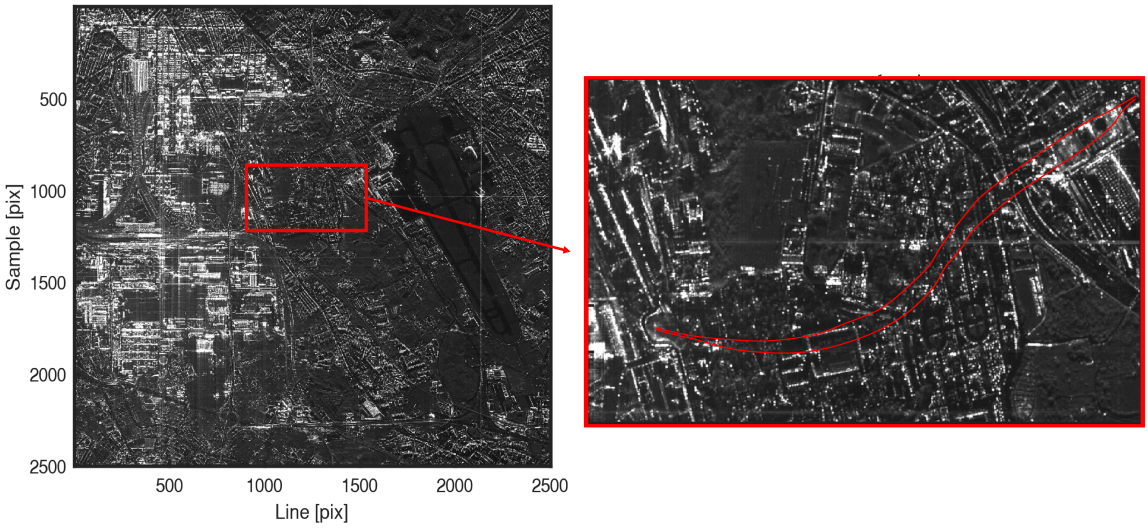
The situation becomes more complex towards the Poggioreale station, due to the presence of a stratigraphic discontinuity (Regione Campania 2013). This discontinuity is a fault that separates the Capodichino hill from the plain to the east, where the *Campanian Ignimbrite* disappears beneath the surface creating a discontinuity with the upstream profile. Along the fault surface, there are pyroclastic deposits, originated from the eruption of the *Neapolitan yellow tuff*, consisting primarily in fine silty sand commonly known as *Pozzolana*. The stratigraphic model at Poggioreale station is reported in Table 4.2.

4.2.3 MT-InSAR monitoring

In this study Synthetic Aperture Radar (SAR) images were obtained from the Italian Space Agency (ASI) dataset. SAR images were acquired by the first generation of the COSMO-SkyMed satellites. The constellation consists of 4 low Earth orbit (600 km) satellites, each of them carrying an X-band SAR antenna with a repeat cycle of 16 days over the major cities of the world. The images can be acquired primarily in three modes: Spotlight mode, acquires single polarized SAR images at very high spatial resolution (1

Table 4.2: Stratigraphic model for the station of Poggioreale

Layer	Depth [m]	E_0 [MPa]	c [kPa]	ϕ [°]	γ [kN m^{-3}]
Backfill, pumices and ashes	0-6	75	15	32	15
Pozzolana	6-25	150	16	34	17



(a) (b)

Figure 4.19: (a) Reflectivity Map (RM) and (b) subset of RM showing the analysed area and in red the tunnel alignments. Both figures are viewed in the local satellite coordinate system (Line and Sample directions, i.e. Azimuth and Range directions)

m or lower) covering an area up to 100 km^2 (10×10 km); Stripmap mode, acquires single or double polarized SAR images at medium-high spatial resolution (3-15 m) covering an area up to 1.600 km^2 (40×40 km); ScanSAR mode, acquires single polarized SAR images at low spatial resolution (30-100 meter) covering an area up to 40.000 km^2 (200×200 km). Our dataset is formed by a stack of 237 CSK Stripmap-Himage collected in an ascending path direction from March 7^{th} 2018 to January 29^{th} 2022, and covers an area of 40×40 km at 3 meters resolution in both azimuth and range directions (i.e. along track and cross track directions respectively). The Reflectivity Map (RM), i.e. the average amplitude of the microwave signal in the area, is shown in Figure 4.19a, while in Figure 4.19b is shown a subset of the RM that represents the analyzed area. The timeline of images acquisition is presented in Figure 4.20, where the acquisition period more frequent is of 16 days. The latter figure shows the spatio-temporal distribution of the images acquired by the satellite, with the indication of the normal baseline B_n (i.e. the virtual distance that connects the radar satellite positions at different times when acquiring SAR images with the position of the master acquisition) and the temporal baseline B_t.

This work uses the PSI method, consisting in detecting pixels that show high coherence, to retrieve the displacement map (better known as velocity map, mm/year)

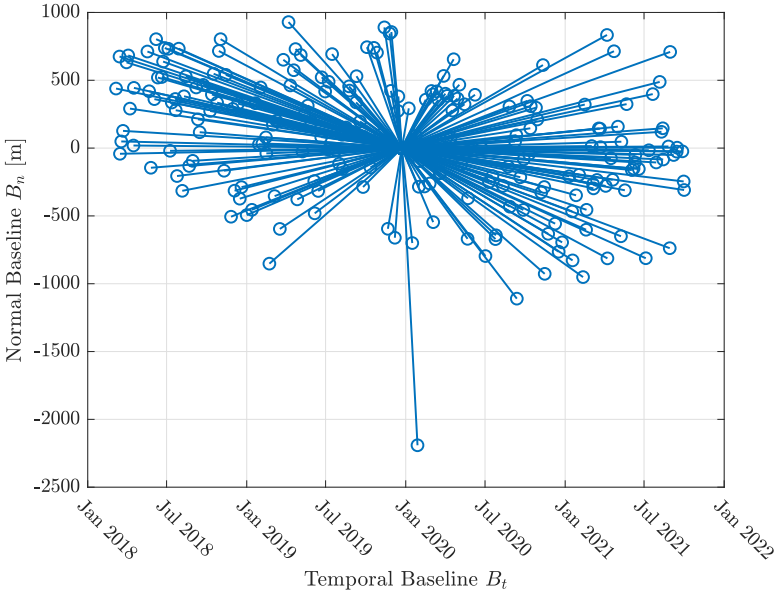


Figure 4.20: Interferogram network (single Master PS analysis), where it can be noted the timeline of data acquisition and normal baseline with reference to the Master Image (December 23^{rd} 2019)

of the interested area, using the software SARPROZ (Perissin 2016). A single Master PS linear analysis was adopted in this framework. PS were selected using a coherence threshold of 0.5, which led to roughly 20.000 scatters in the AoI, with a point density of 30.000 scatters/km^2.

For each scatters, temporal series were interpolated using four linear regressions (see Figure 4.21), one per each following period:

1. March 7^{th} 2018 to July 2^{nd} 2020 (i.e. from beginning of the analysis to prior the first excavation);
2. July 2^{nd} 2020 to March 23^{rd} 2021 (i.e. from the beginning to the end of the fist excavation);
3. March 23^{rd} 2021 to September 7^{th} 2021 (i.e. from the end of the first excavation to the beginning of the second excavation);
4. September 7^{th} 2021 to January 29^{th} 2022 (i.e. from the beginning of the second excavation to the end of the analysis).

From those interpolations, Line of Sight (LOS) cumulative displacements were obtained on July 2^{nd} 2020, March 23^{rd} 2021 and January 29^{th} 2022. By considering the reference point very close to the study area, the local topography and the expected

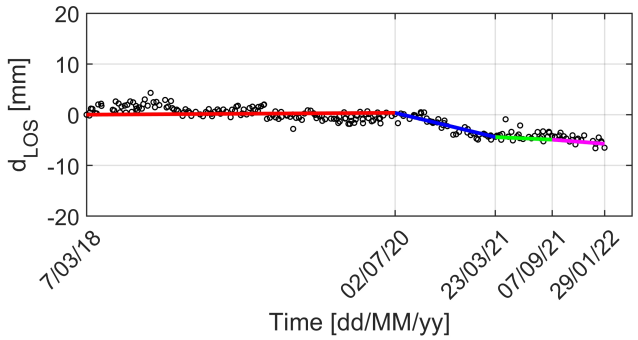


Figure 4.21: Example of time series multi-linear interpolation. Each colored line represents a linear interpolation. Notice that this scatter lies on the longitudinal axis of the first excavated tunnel (coherence γ =0.85.)

deformation processes, it is common to assume that the movements that occurred in these periods, due to tunnelling, are predominantly vertical (Giardina et al. 2019a, Macchiarulo et al. 2021). Monitored displacements data are affected by the presence of existing buildings through the soil-structure interaction. For this reason this study focuses on the northern area of the Cemetery of Poggioreale (Figure 4.17(b)), where only small burial chapels and niches are present. The small dimension of those chapels allows to neglect the soil-structure interaction and to continue to use the free-field approximation inherent in Equation 3.48. The result section is structured in three parts:

- the stability of the AoI is assessed;
- the displacement maps right after the excavation of the first and second excavation are presented;
- the monitored displacemets are compared with the empirical prediction;
- monitored data from MT-InSAR, that lies on cross sections orthogonal to the first excavated tunnel axis (the one further East in Figure 4.17(b)) are interpolated to gain information on V_L and i_x. Then the same will be applied to the second excavation.

Assessment of the AoI before the excavations

In Figure 4.22 are shown the MT-InSAR LOS cumulative displacements in mm from March 7^{th} 2018 to July 2^{nd} 2020, prior to the beginning of the first excavation, along

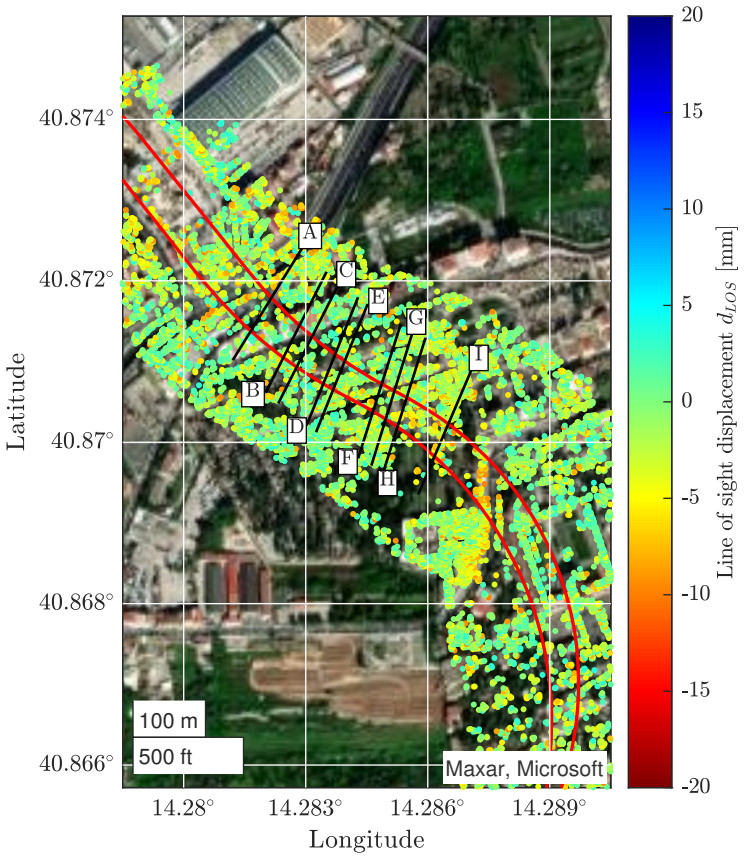


Figure 4.22: Cumulative displacements in mm along the LOS occurred from March 7^{th} 2018 to July 2^{nd} 2020, prior the beginning of the first tunnel excavation. (Image modified after Maxar for Microsoft)

the whole tunnel alignments. It can be noted that the area does not show significant deformations in this time-frame. Indeed, the maximum and minimum cumulative displacements detected along the LOS are roughly 5 mm and -8 mm, which lead to an average velocity of 2 mm/yr and -3 mm/yr respectively. The area was not affected by any phenomenon of subsidence or uplift, and the forthcoming displacements map can be seen as results of the tunnels excavation processes.

Displacements maps after the excavations

In Figure 4.23(a) are shown the cumulative displacements along the LOS from July 2^{nd} 2020 to March 23^{rd} 2021. In this figure the cumulative displacements were aligned to zero on July 2^{nd} 2020, to represent those that occurred due to the excavation of the first tunnel only. In this figure, it is possible to notice a concentration of negative LOS displacements (i.e. subsidence) in proximity of the eastern tunnel axis which is the first

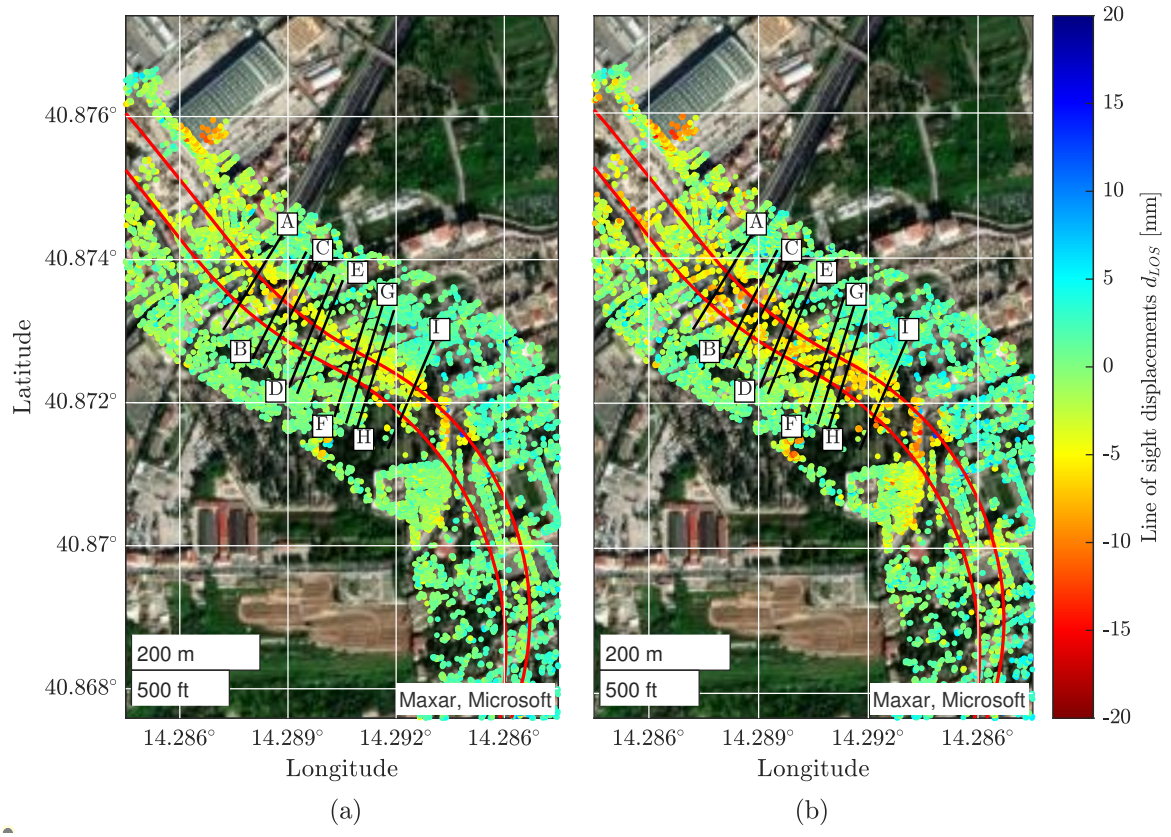


Figure 4.23: (a) Cumulative displacements in mm along the LOS occurred from to July 2^{nd} 2020 to March 23^{rd} 2021, due to the excavation of the first tunnel (right red longitudinal axes). (b) Cumulative displacements along the LOS occurred from to July 2^{nd} 2020 to January 29^{th} 2022, due to the excavation of both tunnels. (Images modified after Maxar for Microsoft).

excavated, as expected. Furthermore, the displacements return to almost zero gradually, as moving away orthogonally from the axis of the excavation. In Figure 4.23(b) are shown the cumulative displacements along the LOS from July 2^{nd} 2020 to January 29^{th} 2022, representing those occurred due to both excavations. In this figure, we can see the presence of many measurement points affected by negative LOS displacements in proximity of both tunnel axes, as expected, and displacements show movements close to zero away from both axes as per Figure 4.23(a).

Empirical settlement prediction

Monitored line of sight (LOS) displacements from Figure 4.23(a) are converted into vertical settlements according to Equation 3.41 and projected on cross sections (A to I of Figure 4.23 (a), (b), orthogonal to the first excavated tunnel axis), to be compared

Table 4.3: Percentage of monitored scatters that fall within the expected range.

A	B	C	D	E	F	G	H	I
64%	53%	67%	59%	78%	55%	64%	79%	54%

with predictions.

On the other hand, settlement profiles are predicted using Equation 3.48, which considers the influence of horizontal displacements. When using Equation 3.48, values of k=0.45, z_0=45 m and volume loss V_L=0.25, 1.0, and 1.75% are assumed. The local incidence angle in the AoI is roughly equal to $\vartheta' = 50°$ and the average angle formed by the cross sections with the LOS direction is $\gamma = 55°$. Thus, the expected increment in maximum settlement is equal to $\psi|_{max} = 1.04$. From Equation 3.47, the shift of the maximum settlement toward the satellite is $\Delta x_v = 5.7$ m. Figure 4.24 shows the comparison between monitored data projected on the vertical plane (black dots) and the expected settlement profiles using Equation 3.48. In most cases, monitored data fall within the expected range, as reported in Table 4.3. Scatters that shows positive values might be associated to errors inherent in the technique.

Volume loss assessment from MT-InSAR data

For volume loss assessment, monitored displacements from Figure 4.23 are converted in vertical settlements according to Equation 3.41, and are then projected on the nine cross sections orthogonal to the first excavated tunnel alignment, shown in the latter figure. Then Equation 3.48 is used to fit the observed settlements, in order to retrieve information on the volume loss V_L. In 4.25 is shown the fitting on nine cross sections considered. The correlation coefficient R^2 are considerably high for all sections but C and H, while the Root Mean Square Error (RMSE), which measures the differences between predicted values and observed values, never exceeds 3 mm. Nevertheless, all volume loss V_L obtained from the best fit are in the expected range of 0.5% to 1% for TBM excavation. The maximum settlements d_v from the best fit are 9.0, 12.5, 7.0, 7.8, 7.4, 6.1, 6.1, 6.5 and 7.7 mm for section A to I respectively.

To retrieve the actual maximum settlement $w(x)$, these values should be divided by the $\psi|_{max}$, which for $\vartheta' = 50°$, $\gamma = 55°$ and K=0.25-0.45 is equal to 1.01-1.04, pratically

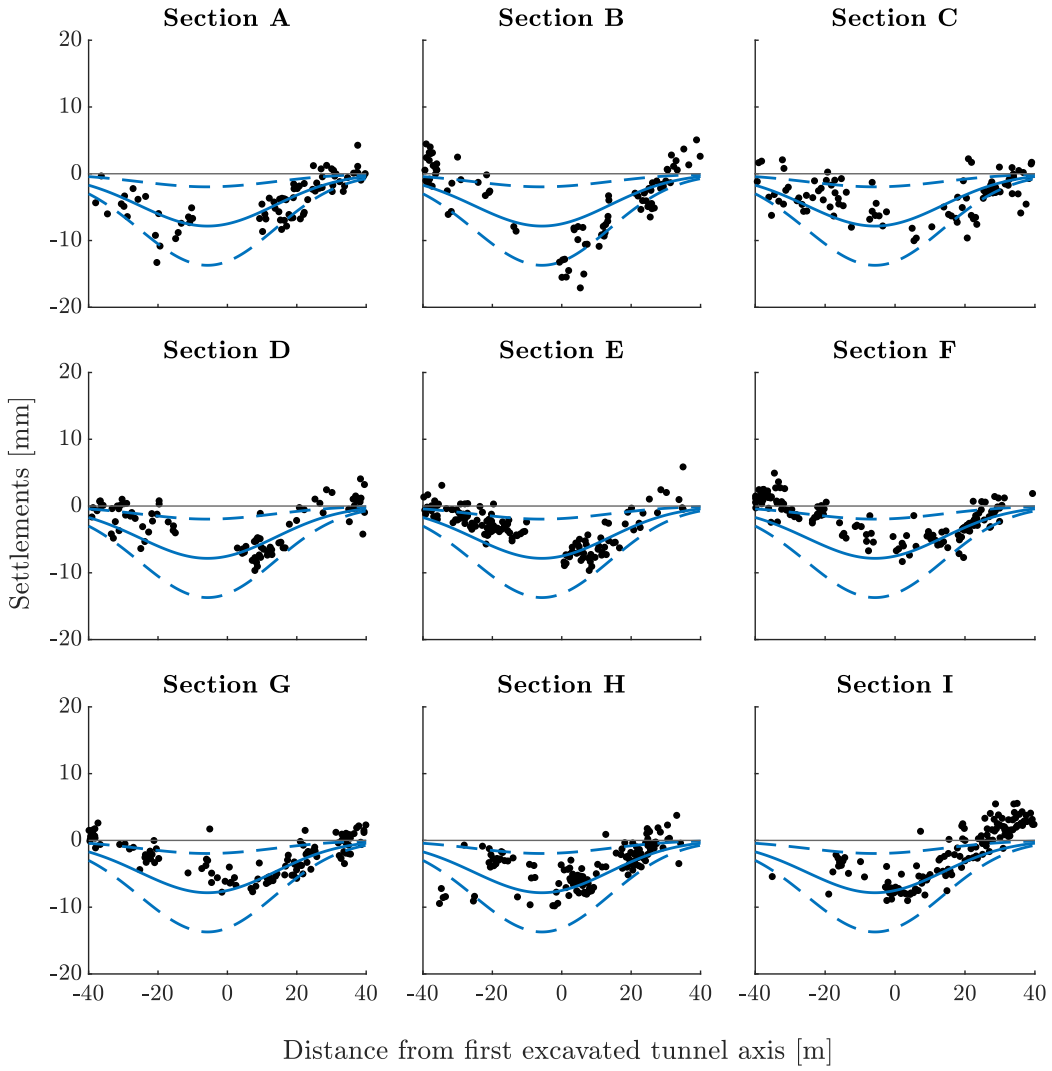


Figure 4.24: Comparison between monitored data projected on the vertical plane (black dots) and predicted settlement profiles d_v using Equation 3.48 (dashed-solid-dashed lines for V_L=0.25, 1, and 1.75%, respectively). Sections A to I refer respectively to those in Figures 4.23 (a), (b).

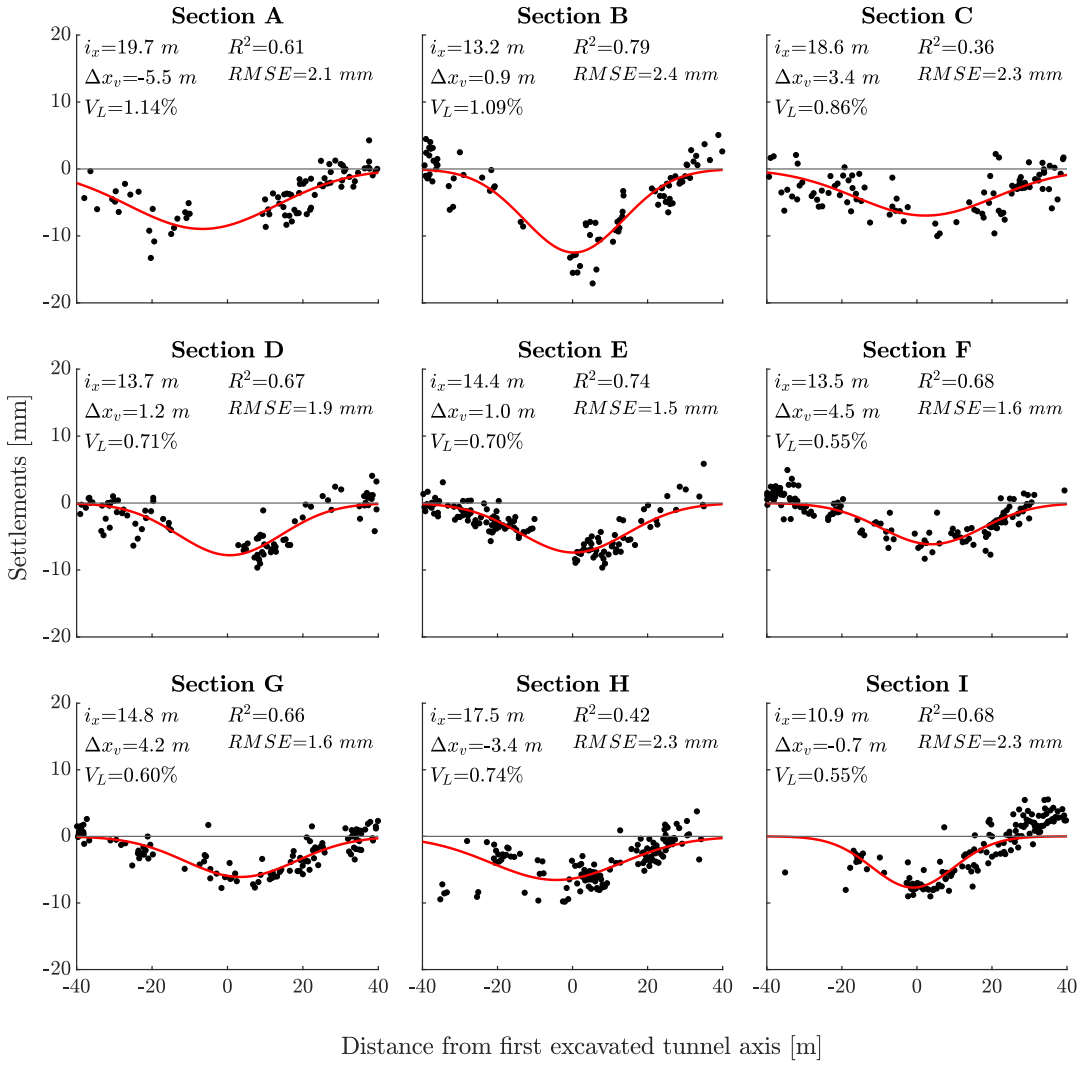


Figure 4.25: First excavation - monitored settlements d_v (black dots) vs Gaussian fit (solid red line, Equation 3.48).

negligible for engineering applications.

Figure 4.26 shows the fitting on the same cross sections as previously presented, focusing solely on the results of the second excavation. This approach involves subtracting the monitored data of the first excavation from the total settlements induced by both excavations. This time the correlation coefficient R^2 are lower compared to the first excavation, while the RMSE increases, but without exceeding the value of 3 mm. This might be due to the fact that more scatters are taken into account and the dispersion of the sample increases. Neverthless, also in this case the volume loss V_L obtained from the best fit are in the expected range of 0.5% to 1%, actually almost

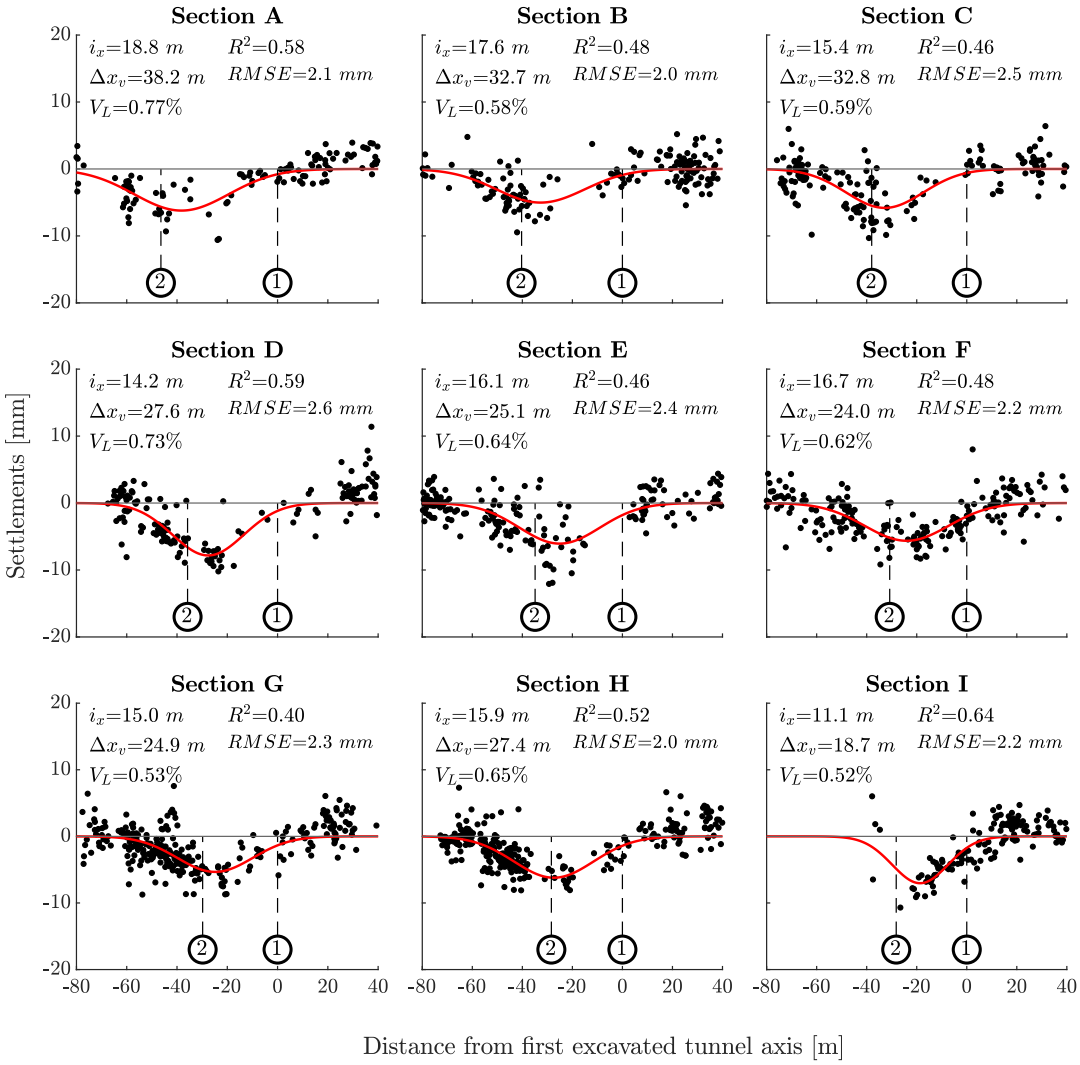


Figure 4.26: Second excavation - monitored settlements d_v (black dots) vs Gaussian fit (solid red line, Equation 3.48). The profiles are centered on the first tunnel axis.

matching those from the first excavation, indicating that both excavations have been performed in similar geological conditions (as it actually is).

4.3 MT-InSAR - Barcelona

4.3.1 Introduction

This case study pertains to a portion of the Metro Line 9 in Barcelona which total length is of 48 km with 52 stations. The whole metro line is divided into 4 main sections shown in the following Figure 4.27. Here the focus is directed toward a portion

of section number 2 that extends from *Zona Franca* to *Zona Universitaria*, where a residential complex has been damaged by the tunnelling excavation (Di Mariano et al. 2021) (Figure 4.28).

4.3.2 Excavation details and geological conditions

The excavation, belonging to the Line 9 (L9) project, was executed with a 12.06 m diameter Earth Pressure Balance (EPB) Tunnel Boring machine (TBM) and was part of the L9 branch connecting Barcelona to its port logistics activities zone. Tunnelling, in this area, started from Foneria station and was headed towards Ildefons Cerdà station (from the left to the right in Figure 4.29), about 700 m apart from the first one. The tunnel alignment crosses a densely urbanised area with a cover to diameter ratio, C/D, in the range 2.5-3.0.

The geological profile along the alignment (Figure 4.29) involved Quaternary soft alluvial and detrital deposits (QM, QS and QR), overlaying Miocene hard formations (M1U and M2L) consisting of siltstone and argillite. The water table is located in the alluvial deposits at a depth of about 8 m from the ground surface and at 22-28 m above the tunnel crown. The first 100 m or so of the excavation were quite challenging due to the presence of mixed ground conditions at the tunnel face, including a thin layer of highly permeable gravels at the tunnel crown. This contingency caused loss of pressure in the EPB cutter head and, as a result, some overexcavation was experimented

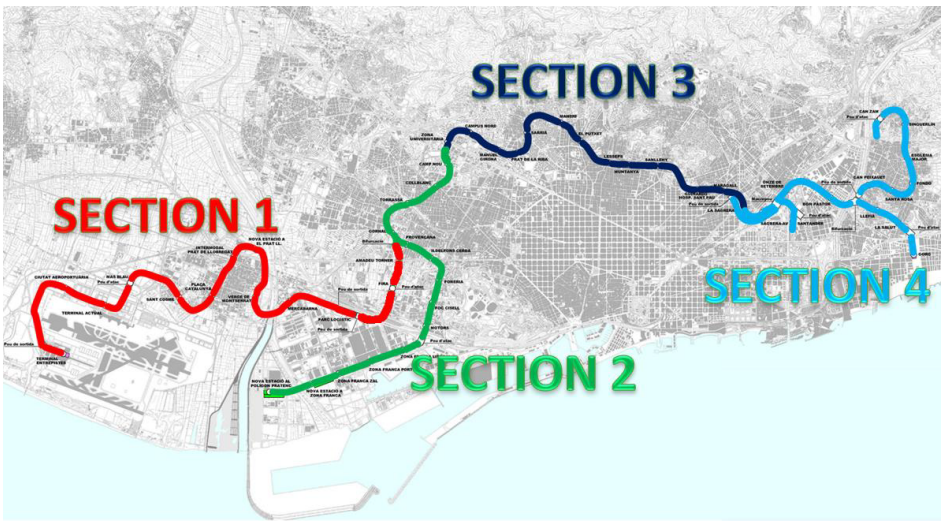


Figure 4.27: Overview of Metro Line 9 in Barcelona (Di Mariano 2023).

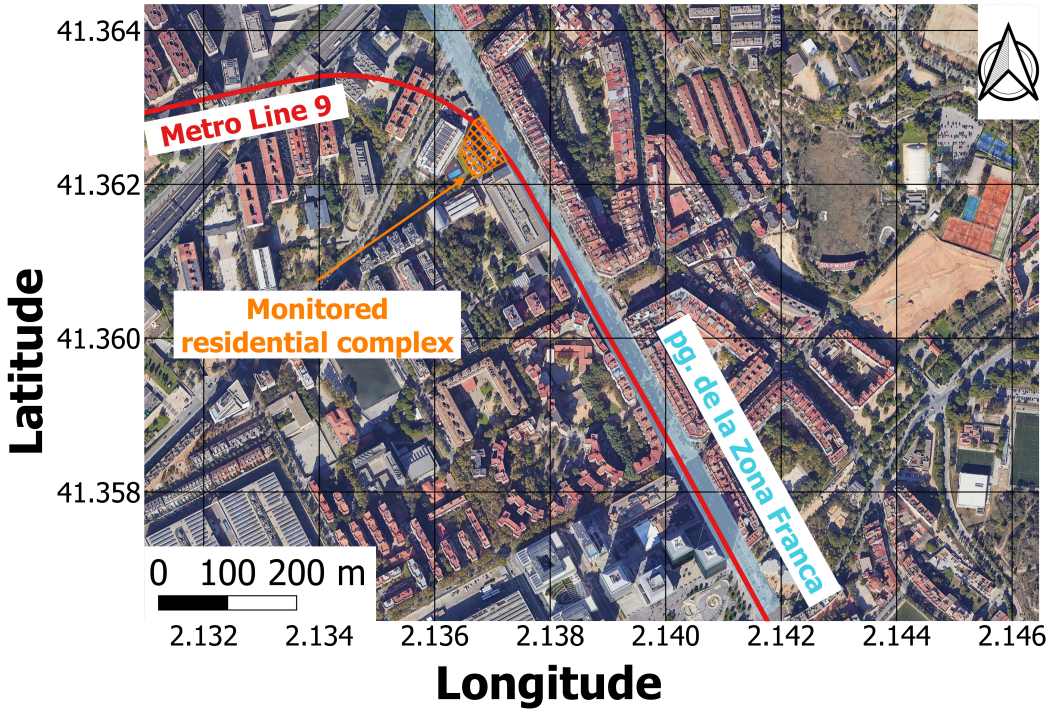


Figure 4.28: Portion of section number 2 of Figure 4.27. Area of Interest (AoI) with the indication of the Metro Line 9 (red solid line) and the monitored residential complex (in orange solid texture).

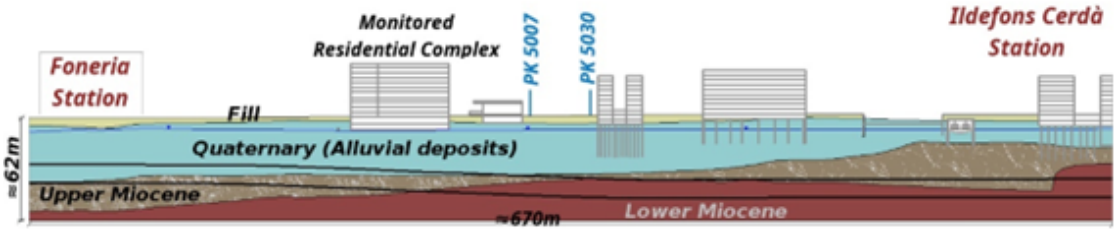


Figure 4.29: Geological profile of the tunnel alignment in the area of study.

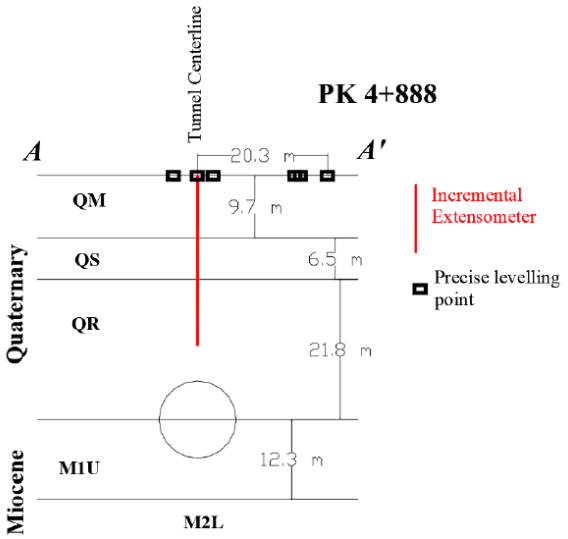


Figure 4.30: Conventional monitoring at PK4888, in proximity to the monitored residential building.

just before the boring machine approached a well monitored 10-storey residential framed building (Figure 4.29) having a 2-level underground parking garage. Below the building, tunnelling became even more difficult because the alignment curves (radius of curvature of 300 m) right where the building south façade is located (Figure 4.29). The challenging tunnelling conditions led to volume losses in the range 0.5-1.0% that gave rise to significant ground movements. As the EPB machine moved towards the north façade of the building, the mixed ground conditions at the tunnel face gradually changed to approximately uniform conditions with the harder Miocene materials occupying nearly the whole excavation section. Also, the tunnel depth slowly increased contributing to lower observed volume losses. A comprehensive instrumentation system was set up to monitor tunnelling operations. Manual and automatic instruments were used to measure surface and subsurface ground movements (Figure 4.30), as well as 3D movements of the framed building and its basement (Di Mariano et al. 2021).

4.3.3 Numerical analysis

To study the complex Soil Structure Interaction (SSI) phenomenon produced by tunnelling below the monitored residential building, fully coupled 3D numerical analyses were carried out with the commercial Finite Element (FE) code PLAXIS 3D. For simplicity

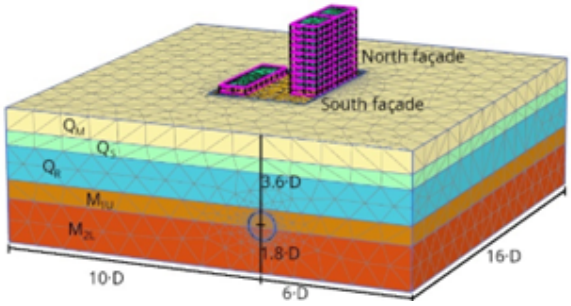


Figure 4.31: Finite Element Model for the excavation. D is the tunnel diameter.

purposes, a geological profile with horizontal stratigraphic layers was considered (Figure 4.31). The numerical model reproduces the tunnel curved alignment, the operating parameters of the EPB boring machine and the installation of the lining. It also reproduces the conicity of the shield, the weight of the back-up trailer and the eccentric position of the lining with respect to the EPB shield. The model replicates the excavation process with a step by step procedure that allows to consider the segments width. Nevertheless, the segmentation of the lining in the tunnel transverse direction is not considered.

A non-linear type of the hyperbolic constitutive model, formulated in the frame of friction hardening plasticity, was used to represent the behaviour of all ground materials (Hardening soil with small stiffness, HSsmall). The model considers the nonlinear ground stiffness decay as shear strains increase. On the other hand, linear-elastic laws were assumed for all structural elements, which were far from failure conditions. The main geomechanical parameters used in the analysis reported in this thesis are shown in Table 4.4. They were inferred from both laboratory and in situ investigations. Among other tests, SPT (Standard Penetration Test) tests, Menard type pressure tests and Lefranc permeability tests were realised on site. With the use of the extracted samples, laboratory tests were performed to assess the granulometry, the limits of Atteberg, humidity, dry density, apparent density and other characteristics of the different soil layers (Török 2021). A few attempts have been made to adjust the initial estimate of soil stiffness parameters to adequately reproduce the ground movements observed along the line, also considering the effect of contingency ground treatments that were undertaken during the underpassing of the residential building in the model.

Table 4.4: Soil parameters for the Barcelona metro line 9 case (Török 2021).

Material	g $[kN/m^3]$	c' [kPa]	ϕ' [°]	E_{50}^{ref} [MPa]	E_{ur}^{ref} [MPa]	E_{oed}^{ref} [MPa]	m [-]	K [m/s]
QM	17	0	29	16	48	12	0.9	5×10^{-4}
QS	19.6	0	34	11	33	10	0.65	4×10^{-4}
QR	21	1	30	15	46	10	0.6	1×10^{-5}
M1U	21	1	36	46	180	25	0.8	2×10^{-5}
M2L	22.5	10	33	278	833	100	0.9	1×10^{-7}

4.3.4 MT-InSAR monitoring

In this case study, Synthetic Aperture Radar (SAR) images were processed by TRE-Altamira as part of a research agreement with Universitat Politècnica de Catalunya (UPC). SAR images were acquired by the TerraSAR-X (TSX) archive in Stripmap mode, that is as single or double polarized SAR images at a very high spatial resolution (3 meters in this case), covering an area up to 1500 km^2 (30 $\times$ 50 km).

Thirtytwo scenes have been processed, that were collected by satellite TSX1 (sensor SM009) in an ascending path direction from January 7^{th} 2009 to October 2^{nd} 2012: this time range covers completely the time window interested by tunnelling for Line 9 in that area. A total number of 30883 targets over an area of 10.9 km^2 have been considered (corresponding to 2833 targets/km^2) and referenced using the WGS 1984 system in Microsoft Bing Maps. Figure 4.28 showed a detail of the Area of Interest (AoI) along the Passeig de la Zona Franca and Figure 4.32 the velocity displacement map of the AoI from January 7^{th} 2009 to October 2^{nd} 2012 as processed by SqueeSAR, an advanced algorithm for surface displacement detection developed by Ferretti, Fumagalli et al. 2011. Note that in this figure are shown the line of sight velocities in terms of mm/year.

Assessment of the AoI before the excavation

In Figure 4.33 are shown the MT-InSAR LOS cumulative displacements in mm from January 7^{th} 2009 to January 25^{th} 2011, prior the beginning of the excavation, along the whole tunnel alignments. It can be noted that the area does not show significant deformations in this time-frame. Indeed, the maximum and minimum cumulative displacements detected along the LOS are roughly 5 mm and -5 mm, which lead to an average velocity of 2.5 mm/yr and -2.5 mm/yr respectively, with an average velocity of

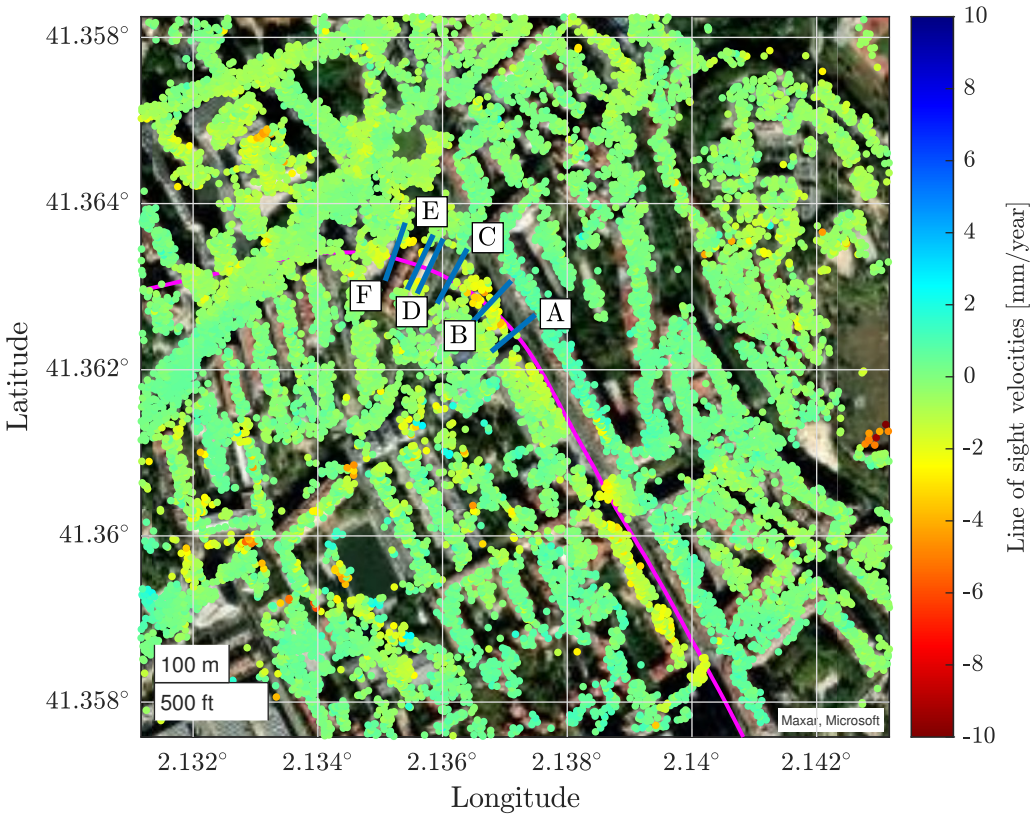


Figure 4.32: Velocity displacement map of the AoI from January 7^{th} 2009 to October 2^{nd} 2012.

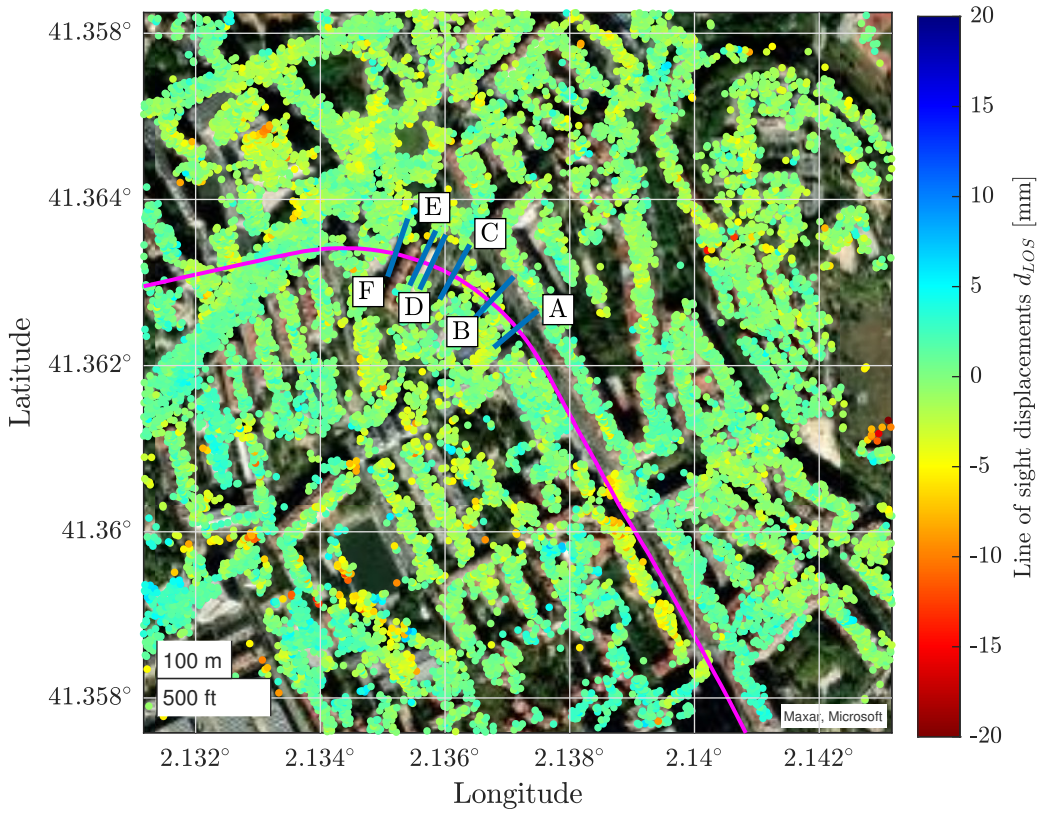


Figure 4.33: Line of sight cumulative displacements in mm from January 7^{th} 2009 to January 25^{th} 2011, prior the beginning of the excavation.

-0.53 mm/year over the whole area. The area was not affected by any phenomenon of subsidence or uplift, and the forthcoming displacements map can be seen as results of the tunnels excavation processes.

Displacements map after the excavation

In Figure 4.34 are shown the line of sight cumulative displacements along the LOS from January 25^{th} 2011 to October 2^{nd} 2012. In this figure the cumulative displacements were aligned to zero on January 25^{th} 2011, to represent those that occurred due to the excavation of the tunnel only. In this figure, it is possible to notice a concentration of negative LOS displacements (i.e. subsidence) in proximity of tunnel alignment, particularly in the area of the selected sections (A to F).

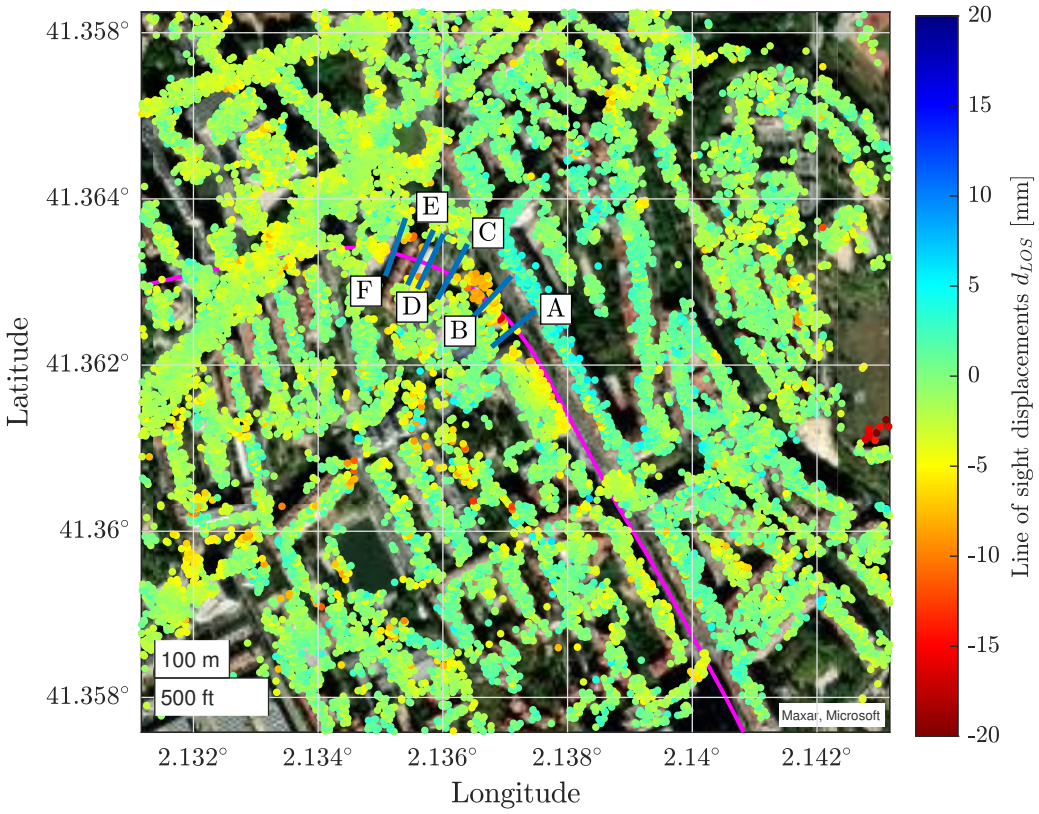


Figure 4.34: Line of sight cumulative displacements along the LOS from January 25^{th} 2011 to October 2^{nd} 2012, induced by the excavation.

Comparison with traditional monitoring

MT-InSAR line of sight cumulative displacements are converted in vertical diplacements (i.e. settlements) according to Equation 3.41. The ground movements measured through Multi Temporal InSAR in permanent scatterers (PS) of the AoI have been systematically compared with the closer precision levelling point (LP) of the conventional survey. Figure 4.35 shows the comparison of measurements in two locations along the tunnel axis, in correspondence of the monitored residential complex. The selected PS point 1 is located about 5 m away from the tunnel axis, 12 m apart from the corresponding T2F04896L037HN007 levelling point, that is located about 1 m away from the tunnel axis. Point 2 and the corresponding LP T2F04953E000HN007 are located about 2 m apart from each other, just on the tunnel axis (Figure 4.35(a)). The time histories of settlement starting from July 2009 are shown in Figure 4.35(b). Both PSs and LPs clearly registered the TBM passing in March 2011. PS point 2 (purple markers) well matches the settlement measured by the corresponding LP. PS point 1 (blue markers) underestimates the settlement measured by the corresponding LP. This is partly justified by the different distance from the tunnel axis of the two points: the out-of-alignment PS point 1 likely settles less than the corresponding levelling point, which is almost over the tunnel axis. Another reason for such discrepancy can be the amount of movement that the ground surface has experienced: this is larger than half of the radar signal wavelength (λ=31.1 mm), therefore the PSInSAR measurements are very likely affected by phase unwrapping (generally it is $\lambda/4$, but in case of monotonic displacements it is $\lambda/2$). In fact, by shifting the measurements to correct this error, the curve with grey markers is obtained for point 1, which is much closer to the corresponding LP curve.

The high density of permanent scatters in the AoI permitted also comparing settlement profiles in transverse direction to the tunnel. Several greenfield transverse alignments of permanent scatters have been identified and compared with the closest monitoring section of conventional optical levelling. Six sections, namely from A to F, have been selected and compared with traditional monitoring from Levelling Points (LP) stations. This comparison is shown in Figure 4.36.

The traditional data have been fitted using a classic gaussian function (i.e. Equation 2.7) while InSAR data have been fitted with Equation 3.48. From the latter figure,

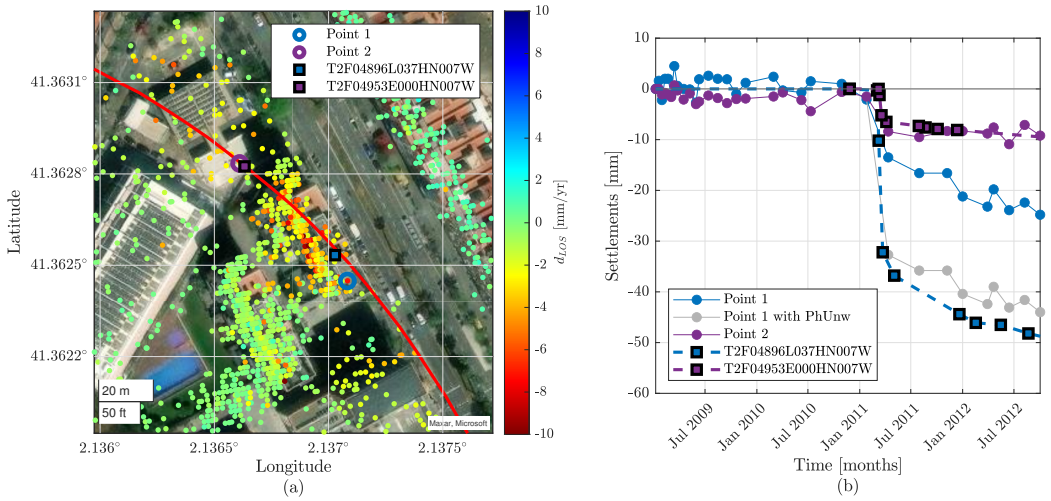


Figure 4.35: (a) Geographic location of traditional instrumentations (black markers) with the indication of the selected Permanent Scatterers for comparison; (b) history time series comparison between traditional mon-itoring stations (black lines) and InSAR scatterers (solid lines with circle markers).

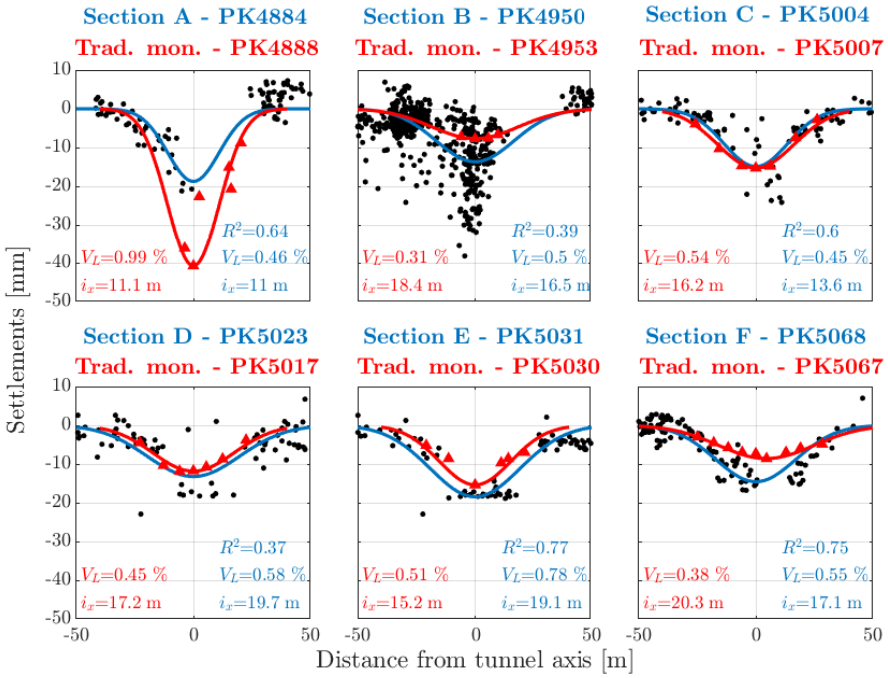


Figure 4.36: Induced settlement trough at six different locations. Comparison between Levelling Points (LP, red markers and solid lines) data and satellite data (InSAR, black circles, fitting blue solid line).

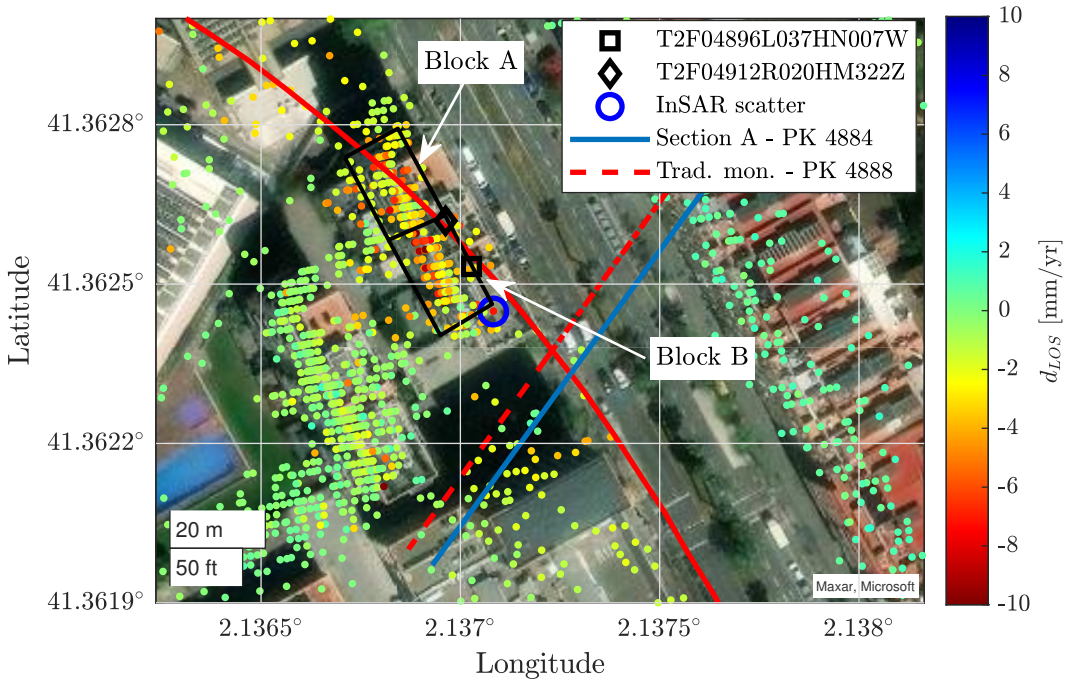


Figure 4.37: Section A. Location of traditional monitoring stations: over the building roof (T2F04912R020HM322Z) and at the street level (T2F4896L037HN007W). Location of the selected InSAR scatter at street level.

sections from C to F show a remarkaly agreement between the data, in terms of settlement shape profile, volume loss V_L and distance of the inflection point i_x from the tunnel axis. Different comments are needed for sections A and B.

For the first section, better displayed in Figure 4.37, it can be seen that the left side of the section crosses the underground residential parking lot, which is a portion of the investigated building, while the right side of the section crosses the street. This means that the left side of the section is stiffer than the right side due to the presence of the underground residental parking and this behaviour is well captured by the satellite data, while the softer behaviour is captured by the traditional monitoring.

On the other hand, section B crosses the residential building. For this reason InSAR data provides more scatterers, at different height along the building. Overall the mean trend follows that of a gaussian shape, but since the building can be affected by both vertical and horizontal movements induced by the tilt over the subsidence area, it is better to assess the bahaviour of the building separately. Figure 4.38 shows a comparison between the InSAR profile of the tunnelling-induced vertical displacement of the block B of the building complex (Figure 4.38(a)) and the corresponding settlement from the

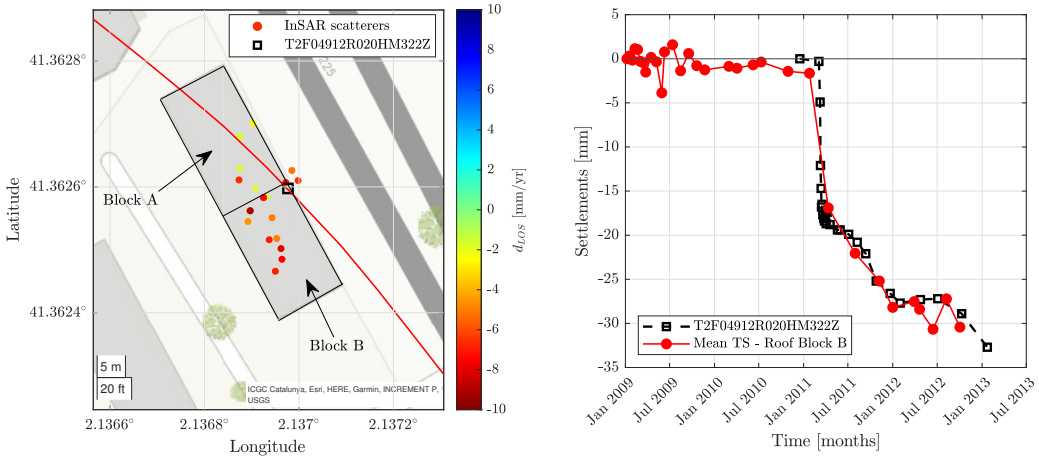


Figure 4.38: Building displacements. Comparison between Levelling Point (LP, black squared markers) data and satellite data (InSAR, circle markers).

conventional survey of optical prisms on the building façade (Figure 4.38(b)). Both trend and magnitude of the displacement are very close, confirming the reliability of the MT-InSAR analysis.

Comparison with 3D numerical analysis

Numerical 3D Finite Element results are used to prove the consistency of the agreement between traditional monitoring and InSAR data. Figure 4.39 shows a comparison between the settlement time history evaluated by processing SAR images of the scatterer, circled in blue in Figure 4.35 and Figure 4.37, and the corresponding settlement calculated by FEA. In the same figure the settlement profile of the close LP T2F4896L037HN007W has also been added for further comparison. Overall, the numerical results match well both InSAR and optical levelling data.

In Figure 4.40 the displacement of Permanent Scatterers and Levelling Points after the full passage of the TBM across the transverse section at PK4888 are compared with the computed settlement profile. The PS displacements along the satellite LoS, gathered in a 10 m wide band across the section, were projected along the vertical direction, assuming that the ground displacements due to tunnelling were predominantly vertical. This assumption may lead to an acceptable error, lower than 5% on the maximum settlement. The FE calculated profile matches only two LP measurements, while it generally overestimates the overall settlement trough that, despite the scatter of the

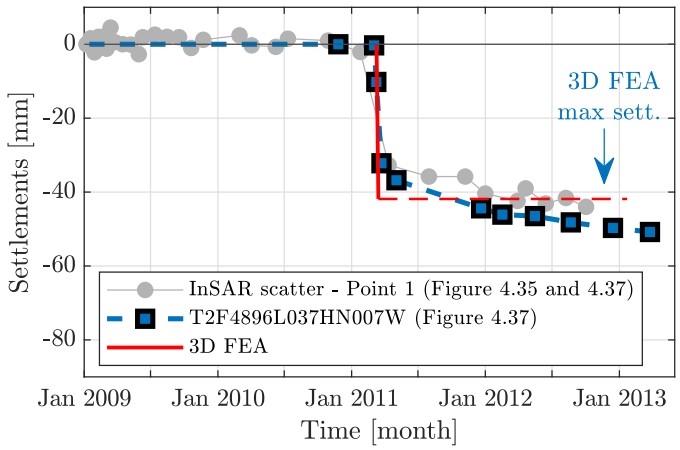


Figure 4.39: Time series comparison between InSAR scatterer, levelling point and corresponding FEA output. The point selected lies at street level.

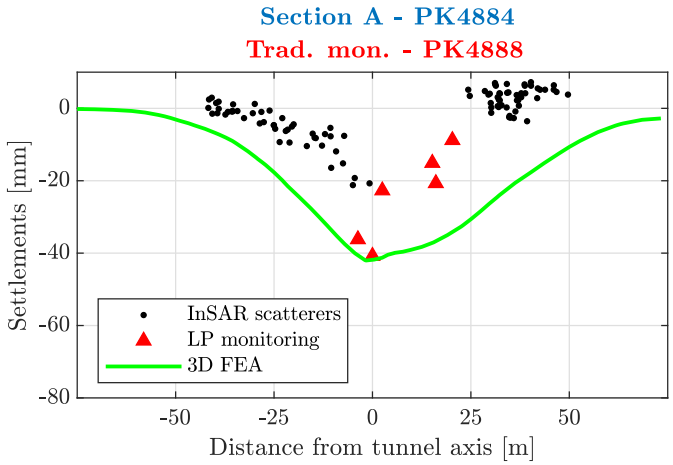


Figure 4.40: Settlement trough: satellite data (InSAR), conventional optical levelling (LP) and FEA results. Section A of Figure 4.36.

MT-InSAR data, emerges clearly from both sets of measurements.

Finally, in Figure 4.41 the time histories of displacement of the PSs that belong to the roof of Block B is averaged and compared both with that of the prism T2F04912R020HM322Z, on the same building roof, and with the corresponding numerical calculation. A good matching can be appreciated in this case.

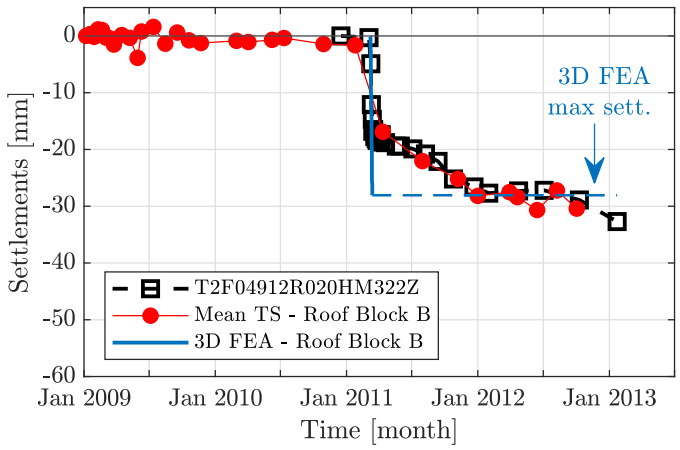


Figure 4.41: Comparison between InSAR, LP and FEA for Block B roof displacement.

Chapter 5

Conclusions

This research used 3D FEAs to expand the experimental evidence on the feasibility of using Distributed Fibre Optic Sensing technology for subsidence monitoring. The numerical analyses have been validated against experimental results from $1g$ trapdoor tests on DFOS cables embedded in a cohesionless soil layer. The displacement and strain fields measured in the tests were correctly predicted by carefully calibrating the constitutive model at small strain and stress levels. A method for numerical modelling of Hostun sand at low confining stresses is discussed and a list of calibrated parameters is provided. A frictional contact between the cable and the soil was defined in the numerical model to closely mimic the soil-cable interface during experimental testing. The 3D FE model enabled inspection of the soil strain field around the cable and in the far field. This made it possible to gain information on the reciprocal influence of the cable and the soil, which may affect the cable strain.

Experimental evidence has shown that measured fibre optic cable strains were much lower than PIV measured soil strains. The 3D numerical analyses corroborate this experimental observation, showing that the soil-cable interface permits a limited relative displacement between the soil and the cable. The difference between PIV measured soil strains and DFOS cable strain is hence mostly due to a loss of shear transfer between the soil and the cable interface.

The numerical results also show that the strains within the cable are mostly induced by horizontal movements. The FEAs confirmed common knowledge that enhanced measurement of the soil strain is obtained when improving the coupling between the

soil and the cable. However, the research also highlights that the signature strain profile for cables located close to the soil surface is generated almost purely by horizontal strain within the ground, which is transferred to the cable provided that its horizontal movement is not constrained. This provides valuable information for cable laying techniques, which is currently an important area of research (e.g. X. Xu, Kechavarzi et al. 2022). The results of this thesis imply that the horizontal stiffness of the system used to enhance soil-cable coupling in practice must be reduced as much as possible. The results of the numerical analyses also enabled validation of the methodology outlined by Möller et al. 2023 to locate the subsidence for realistic stress levels in the field. The limitations of the methodology used by Möller et al. 2023 are also highlighted, and in particular the cable installation at the boundary and the limited size of the box, a problem that would still persist in the centrifuge. Nevertheless, this thesis provides confidence in the $1g$ testing method as a proof of concept for the use of DFOS cables above subsidence formation.

Finally, the analyses presented in this thesis enable the findings to be extended numerically to the formation of subsidence in three dimensions. The results show that DFOS would display a large signature strain profile if located anywhere within $0.5D$ of the trapdoor centreline, but display a much attenuated signal when located at or beyond $0.75D$, where D is the trapdoor diameter. The results also demonstrate better accuracy for cables laid closer to the soil surface, where the horizontal ground movements are higher. This provides grounds for further research on how to lay fibre-optic cables to obtain efficient strain transfer, as well as on the interpretation of the strain to predict the surface damage zone. The reference tests used in this thesis were evidently performed in controlled conditions, where the measurements were not affected by changes in strain from external factors. In situ applications will, however, be subjected to temperature and moisture content changes, as well as vibrations from human activities (train, road, construction, etc.), which will pollute the otherwise sensitive DFOS signal. Temperature changes can typically be corrected by adding a fibre that senses seasonal and daily changes in temperature on a specific channel of the interrogator (Kechavarzi et al. 2016), but this technique might not be sufficient at small strain levels, as needed for this particular application. Further work is required to identify how to filter the signal

properly and reveal the signature strain profile indicating subsidence formation for application of this type of technology in the field; however, this thesis demonstrates that the use of distributed fibre optic sensing for the detection of subsidence at full scale is a promising technology.

The possibility of using combined Multi Temporal Interferometric Synthetic Aperture Radar (MT-InSAR) technology is also investigated for this purpose.

MT-InSAR has been used for many different applications in the past decades (earthquakes, volcanoes, landslides, subsidences and so on). Recently, its use has also been directed toward the monitoring of tunnel excavation. One of the main parameters to be monitored is the so-called volume loss V_L, which permits the prediction of the subsidence profile induced by the excavation. In this research, MT-InSAR was used to retrieve the surface settlement profiles from the excavation of twin tunnels belonging to the extension of the Metro Line 1 in the city of Naples (Italy) and for the well documented case of Line 9 extension (now Line 10 south) of Barcelona metro. For the first case study, satellite monitored data from the excavation of the first tunnel were projected onto the cross section orthogonal to the tunnel axis and interpolated using well known empirical relations. From the latter, information was gathered on the volume loss V_L and on the inflection point distance from tunnel axis i_x. As a result, volume loss V_L values were in the expected range for a common TBM excavation.

For the second case study, tunnelling induced ground and building displacements from conventional optical survey of and from Multi-Temporal Interferometry of SAR satellite image processing have been compared. MT-InSAR results agree overall with the displacement time histories that were measured from the Earth's surface with optical survey, as shown for ground settlements along the tunnel alignments and for building displacements along the Line of Sight of the satellite. Settlement profiles of Permanent Scatterers along tunnel transverse sections after the excavation also well agree with those of close levelling points. Some inaccuracy may be observed in the InSAR profiles that may be attributed either to difficult positioning or to low backscattering properties at some positions. However, both the volume loss, V_L, and the distance of inflection point from the tunnel axis, i_x, that have been assessed from satellite data are close to those from conventional monitoring transverse sections. A few assumptions were made

when interpreting processed SAR image data to overcome some limitations, such as phase unwrapping, that makes MT-InSAR useful to complement terrestrial monitoring and not to substitute it. Nevertheless, the potential of satellite images processing in this field is clearly shown in this research. It is also worth noticing that nowadays, more than one decade after the completion of this tunnel construction, SAR images datasets of urban areas interested by tunnelling works have increased. By integrating datasets from different satellite constellations, the quality of monitoring tunnelling induced displacements may significantly improve. New constellations of SAR satellites aimed to high resolution imaging of the earth surface are currently under production and this will permit very soon further reducing the time elapsed between observations and expanding the ground deformation database, with clear benefits for the application of multitemporal InSAR analysis in this field.

In conclusion, the methodology presented in this study provides an effective way of predicting settlements induced by tunneling processes using MT-InSAR data. The results obtained in this study demonstrate the reliability of the methodology and its potential to be used in real-life scenarios. However, the limitations of the methodology should be considered, and further research is needed to improve its accuracy and applicability in different scenarios.

Indeed, future applications might benefit from the improvements of the technology in terms of higher resolution (e.g. $0.1 \times 0.1m$ for the second generation of COSMO-SkyMed constellation) and shorter revist time, which could enable better continuous monitoring in space and time respectively. Furthermore, the analysis of multiple acquisitions in both ascending and descending directions presents an opportunity to discern vertical and east-west (E-W) displacement components. However, it's important to note that acquisitions in these directions do not occur simultaneously, requiring careful consideration during analysis. Looking ahead, future SAR constellations, such as those from the IRIDE space program by the Italian Space Agency, will deploy satellites with inclined orbits. These inclined orbits will facilitate the separation between the east-west horizontal component and the south-north horizontal component, leading to a complete definition of the displacement vector in three directions.

Appendix A

Solution of Equation 3.46

Step by step solution of Equation 3.46:

$$w(x) = w_{max} \cdot \exp\left(-\frac{x^2}{2 \cdot k^2 \cdot z^2}\right)$$

$$u(x) = \frac{x}{z_0} \cdot w(x)$$

$$\frac{u(x)}{w(x)} = \frac{x}{z0} \implies \alpha = \arctan\frac{x}{z_0}$$

$$\beta(x) = \vartheta' - \alpha(x)$$

$$d_{LOS}(x) = \sqrt{w(x)^2 + u(x)^2} \cdot \cos\beta = p(x) \cdot \cos\left(\vartheta' + \alpha(x)\right)$$

$$d_v = \frac{d_{LOS}(x)}{\cos\vartheta'} = \frac{p \cdot \cos\left(\vartheta' + \alpha(x)\right)}{\cos\vartheta'}$$

$$w(x) = p \cdot \cos\alpha(x)$$

$$\psi = \frac{d_v(x)}{w(x)} = \frac{p \cdot \cos\left(\vartheta' + \alpha(x)\right)}{\cos\vartheta'} \cdot \frac{1}{p \cdot \cos\alpha(x)} = \frac{\cos\left(\vartheta' + \alpha(x)\right)}{\cos\vartheta' \cdot \cos\alpha(x)} =$$

$$= \frac{\cos\vartheta' \cdot \cos\alpha(x) - \sin\vartheta' \cdot \sin\alpha(x)}{\cos\vartheta' \cdot \cos\alpha(x)} = 1 - \tan\vartheta' \cdot \tan\alpha(x) = 1 - \frac{x}{z_0} \cdot \tan\vartheta' \implies$$

$$\implies \psi = 1 - \frac{x}{z_0} \cdot \tan\vartheta' \qquad \text{(Eq. 3.46)}$$

Solution of Equation 3.47

Starting with the function:

$$d_v(x) = \left(1 + \frac{x}{z_0} \cdot \tan\vartheta'\right) \cdot 0.31 \cdot \frac{V_L \cdot D^2}{k \cdot z_0} \cdot \exp\left(-\frac{x^2}{2 \cdot k^2 \cdot z_0^2}\right)$$

Assuming $\sigma = 0.31 \cdot V_L \cdot D^2$, and substituting:

$$d_v(x) = \frac{\sigma}{k \cdot z_0} \cdot \exp\left(-\frac{x^2}{2 \cdot k^2 \cdot z_0^2}\right) + \frac{\sigma \cdot x \cdot \tan\vartheta'}{k \cdot z_0^2} \cdot \exp\left(-\frac{x^2}{2 \cdot k^2 \cdot z_0^2}\right)$$

Now, let's find the derivative with respect to x:

$$d_v'(x) = \frac{d}{dx}\left(\frac{\sigma}{k \cdot z_0} \cdot \exp\left(-\frac{x^2}{2 \cdot k^2 \cdot z_0^2}\right) + \frac{\sigma \cdot x \cdot \tan\vartheta'}{k \cdot z_0^2} \cdot \exp\left(-\frac{x^2}{2 \cdot k^2 \cdot z_0^2}\right)\right) =$$

$$= \frac{\sigma}{k \cdot z_0} \cdot \frac{d}{dx}\left(\exp\left(-\frac{x^2}{2 \cdot k^2 \cdot z_0^2}\right)\right) + \frac{\sigma \cdot \tan\vartheta'}{k \cdot z_0^2} \cdot \frac{d}{dx}\left(x \cdot \exp\left(-\frac{x^2}{2 \cdot k^2 \cdot z_0^2}\right)\right)$$

Using the chain rule ($\frac{d}{dx}e^{f(x)} = e^{f(x)}\frac{df}{dx}$), where $f(x) = -\frac{x^2}{2 \cdot k^2 \cdot z_0^2}$:

$$d_v'(x) = \frac{\sigma}{k \cdot z_0} \cdot \left(-\frac{2 \cdot x}{2 \cdot k^2 \cdot z_0^2}\right) \cdot \exp\left(-\frac{x^2}{2 \cdot k^2 \cdot z_0^2}\right) +$$

$$+\frac{\sigma \cdot \tan\vartheta'}{k \cdot z_0^2} \cdot \left(\exp\left(-\frac{x^2}{2 \cdot k^2 \cdot z_0^2}\right) + x \cdot \left(-\frac{2 \cdot x}{2 \cdot k^2 \cdot z_0^2}\right) \cdot \exp\left(-\frac{x^2}{2 \cdot k^2 \cdot z_0^2}\right)\right) =$$

$$= -\frac{\sigma}{k^3 \cdot z_0^3} \cdot x \cdot \exp\left(-\frac{x^2}{2 \cdot k^2 \cdot z_0^2}\right) + \frac{\sigma \cdot \tan\vartheta'}{k \cdot z_0^2} \cdot \exp\left(-\frac{x^2}{2 \cdot k^2 \cdot z_0^2}\right) \cdot \left(1 - \frac{x^2}{k^2 \cdot z_0^2}\right)$$

Now let's find the values of x at which the derivative is equal to zero:

$$d_v' = 0 \implies -\frac{\sigma}{k^3 \cdot z_0^3} \cdot x + \frac{\sigma \cdot \tan\vartheta'}{k \cdot z_0^2} \cdot \left(1 - \frac{x^2}{k^2 \cdot z_0^2}\right) = 0 \implies$$

$$-\frac{\sigma}{k^3 \cdot z_0^3} \cdot x + \frac{\sigma \cdot \tan\vartheta'}{k \cdot z_0^2} - \frac{\sigma \cdot \tan\vartheta' \cdot x^2}{k^3 \cdot z_0^4} = 0 \implies$$

$$-\sigma \cdot x + \sigma \cdot \tan\vartheta' \cdot k^2 \cdot z_0 - \frac{\sigma \cdot \tan\vartheta'}{z_0} \cdot x^2 = 0 \implies$$

$$\frac{\tan\vartheta'}{z_0} \cdot x^2 + x - \tan\vartheta' \cdot k^2 \cdot z_0 = 0 \implies$$

$$x = \frac{-1 \pm \sqrt{1 + 4 \cdot \tan^2 \vartheta' \cdot k^2}}{2 \cdot \tan \vartheta' / z_0} = 0.5 \cdot \cot \vartheta' \cdot z_0 \cdot (-1 \pm \sqrt{1 + 4 \cdot \tan^2 \vartheta' \cdot k^2})$$

Since we are intrested in the negative root:

$$\Delta x_v = 0.5 \cdot \cot \vartheta' \cdot z_0 \cdot (-1 - \sqrt{1 + 4 \cdot \tan^2 \vartheta' \cdot k^2}) \qquad \text{(Eq. 3.47)}$$

Proof $V_L^* = V_L$

Consider the functions $w(x)$ and $d_v(x)$. The integral of the first function $w(x)$ is a fraction (namely volume loss, V_L) of the excavated volume per unit of length:

$$\int w(x) \cdot dx = V_L \cdot \frac{\pi \cdot D^2}{4}$$

Moreover, the integral of the second function can be expressed as a fraction of the excavated volume per unit length (namely V_L^*), as follows:

$$\int d_v(x) \cdot dx = \int (1 + \frac{x}{z_0} \cdot \tan \vartheta') \cdot w(x) \cdot dx = V_L^* \cdot \frac{\pi \cdot D^2}{4}$$

Using the integration by parts,

$$\int f(x) \cdot g(x) \cdot dx = f(x) \cdot \int g(x) \cdot dx - \int f'(x) \cdot \left[\int g(x) \cdot dx \right] \cdot dx$$

and assuming $f(x) = 1 + \frac{x}{z_0} \cdot \tan \vartheta'$ and $g(x) = w(x)$, one obtains the following:

$$\int d_v(x) \cdot dx = \left(1 + \frac{x}{z_0} \cdot \tan \vartheta'\right) \cdot \int w(x) \cdot dx - \int \frac{\tan \vartheta'}{z_0} \cdot \left[\int w(x) \cdot dx \right] \cdot dx =$$

$$= \left(1 + \frac{x}{z_0} \cdot \tan \vartheta'\right) \cdot V_L \cdot \frac{\pi \cdot D^2}{4} - \int \frac{\tan \vartheta'}{z_0} \cdot V_L \cdot \frac{\pi \cdot D^2}{4} \cdot dx =$$

$$= V_L \cdot \frac{\pi \cdot D^2}{4} + \frac{x}{z_0} \cdot \tan \vartheta' \cdot V_L \cdot \frac{\pi \cdot D^2}{4} - \frac{x}{z_0} \cdot \tan \vartheta' \cdot V_L \cdot \frac{\pi \cdot D^2}{4} =$$

$$= V_L \cdot \frac{\pi \cdot D^2}{4} = V_L^* \cdot \frac{\pi \cdot D^2}{4} \qquad \Longrightarrow \; V_L = V_L^*$$

Bibliography

Agrawal, G. P. (2012). *Fiber-optic communication systems*. John Wiley & Sons.

Amelung, F., D. L. Galloway, J. W. Bell, H. A. Zebker and R. J. Laczniak (1999). 'Sensing the ups and downs of Las Vegas: InSAR reveals structural control of land subsidence and aquifer-system deformation'. In: *Geology* 27.6, pp. 483–486.

Ansari, F. and Y. Libo (1998). 'Mechanics of bond and interface shear transfer in optical fiber sensors'. In: *Journal of engineering mechanics* 124.4, pp. 385–394.

Attewell, P. (1978). 'Ground movements caused by tunnelling in soil'. In: *International Conference on Large Movements and Structures*, pp. 812–948.

Barla, G., A. Tamburini, S. Del Conte and C. Giannico (2016). 'InSAR monitoring of tunnel induced ground movements'. In: *Geomechanics and Tunnelling* 9.1, pp. 15–22.

Belli, R., B. Glisic, D. Inaudi and B. Gebreselassie (2009). 'Smart textiles for SHM of geostructures and buildings'. In: *Fourth International Conference on Structural Health Monitoring on Intelligent Infrastructure (SHMII-4)*, pp. 200922–24.

Benz, T., R. Schwab and P. Vermeer (2009). 'Small-strain stiffness in geotechnical analyses'. In: *Bautechnik* 86.S1, pp. 16–27.

Benz, Thomas (2007). 'Small-strain stiffness of soils and its numerical consequences'. PhD thesis. Univ. Stuttgart, Inst. f. Geotechnik Stuttgart.

Berardino, P., G. Fornaro, R. Lanari and E. Sansosti (2002). 'A new algorithm for surface deformation monitoring based on small baseline differential SAR interferograms'. In: *IEEE Transactions on geoscience and remote sensing* 40.11, pp. 2375–2383.

Bersan, S., O. Bergamo, L. Palmieri, L. Schenato and P. Simonini (2018). 'Distributed strain measurements in a CFA pile using high spatial resolution fibre optic sensors'. In: *Engineering Structures* 160, pp. 554–565.

Blairon, S., JM. Henault, E. Buchoud, G. Vinceslas and S. Delepine-Lesoille (2011). 'Truly distributed optical fiber extensometers for geotechnical structure monitoring (dikes and underground repository): Influence of sensor external coating'. In: *Eighth international symposium of Field Measurement in Geomecanics, Berlin, Germany*.

Bolton, M. D. (1986). 'The strength and dilatancy of sands'. In: *Géotechnique* 36.1, pp. 65–78.

Boscardin, M. D. and E. J. Cording (1989). 'Building response to excavation-induced settlement'. In: *Journal of Geotechnical Engineering* 115.1, pp. 1–21.

Brinkgreve, R. B. J., E. Engin and W. M. Swolfs (2015). *Plaxis 3D manual*. Plaxis bv, Bentley Systems,Inc.

Buchoud, E., V. Vrabie, J. I. Mars, G. D'Urso, A. Girard, S. Blairon and JM. Henault (2015). 'Quantification of submillimeter displacements by distributed optical fiber sensors'. In: *IEEE Transactions on instrumentation and measurement* 65.2, pp. 413–422.

Burland, J. B. and C. P. Wroth (1975). *Settlement of buildings and associated damage*. Tech. rep.

Chakraborty, T. and R. Salgado (2010). 'Dilatancy and shear strength of sand at low confining pressures'. In: *Journal of geotechnical and geoenvironmental engineering* 136.3, pp. 527–532.

Chehade, F. H. and I. Shahrour (2008). 'Numerical analysis of the interaction between twin-tunnels: Influence of the relative position and construction procedure'. In: *Tunnelling and underground space technology* 23.2, pp. 210–214.

Cording, E. J. (1975). 'Displacement around soft ground tunnels-General report'. In: *Fifth Pan-American Conference on Soil Mechanics and Foundation Engineering*, pp. 571–632.

Costantini, M., S. Falco, F. Malvarosa and F. Minati (2008). 'A new method for identification and analysis of persistent scatterers in series of SAR images'. In: *IGARSS 2008-2008 IEEE International Geoscience and Remote Sensing Symposium*. Vol. 2. IEEE, pp. II–449.

Crosetto, M., E. Biescas, J. Duro, J. Closa and A. Arnaud (2008). 'Generation of advanced ERS and Envisat interferometric SAR products using the stable point

network technique'. In: *Photogrammetric Engineering & Remote Sensing* 74.4, pp. 443–450.

Crosetto, M., O. Monserrat, M. Cuevas-González, N. Devanthéry and B. Crippa (2016). 'Persistent scatterer interferometry: A review'. In: *ISPRS Journal of Photogrammetry and Remote Sensing* 115, pp. 78–89.

Da Silva Burke, T. S. (2018). 'Centrifuge modelling of the behaviour of geosynthetic-reinforced soils above voids'. PhD thesis. University of Cambridge.

Da Silva Burke, T. S. and M. Z. E. B. Elshafie (2021). 'Arching in granular soils: experimental observations of deformation mechanisms'. In: *Géotechnique* 71.10, pp. 866–878.

Darendeli, M. B. (2001). 'Development of a new family of normalized modulus reduction and material damping curves'. PhD thesis. The University of Texas at Austin.

Davis, M., N. A. Hoult and A. Scott (2017). 'Distributed strain sensing to assess corroded RC beams'. In: *Engineering Structures* 140, pp. 473–482.

De Battista, N., C. Kechavarzi and K. Soga (2016). 'Distributed fiber optic sensors for monitoring reinforced concrete piles using Brillouin scattering'. In: *Sixth European Workshop on Optical Fibre Sensors*. Vol. 9916. SPIE, pp. 114–117.

Devanthéry, N., M. Crosetto, O. Monserrat, M. Cuevas-González and B. Crippa (2014). 'An approach to persistent scatterer interferometry'. In: *Remote sensing* 6.7, pp. 6662–6679.

Di Mariano, A. (2023). *Informal communication and presentations*.

Di Mariano, A., A. Franza, V. Limatola, A. Gens and E. Bilotta (2021). 'Building Response to Line 9 EPB Tunnelling in Barcelona. A Case Study'. In: *Challenges and Innovations in Geomechanics: Proceedings of the 16th International Conference of IACMAG*. Vol. 2. Springer, pp. 172–180.

Di Murro, V., L. Pelecanos, K. Soga, C. Kechavarzi, R. F. Morton and L. Scibile (2016). 'Distributed fibre optic long-term monitoring of concrete-lined tunnel section TT10 at CERN'. In: *Transforming the Future of Infrastructure through Smarter Information: Proceedings of the International Conference on Smart Infrastructure and ConstructionConstruction*. ICE Publishing, pp. 27–32.

Di Pace, M., R. Cocchi and M. L. De Gugliemo (2021). 'Scavo Meccanizzato: TBM a spasso per Napoli'. In: *Le Strade* 6, pp. 82–87.

Ding, X., Z. Li, J. Zhu, G. Feng and J. Long (2008). 'Atmospheric effects on InSAR measurements and their mitigation'. In: *Sensors* 8.9, pp. 5426–5448.

Duro, J., J. Inglada, J. Closa, N. Adam and A. Arnaud (2005). 'High resolution differential interferometry using time series of ERS and ENVISAT SAR data'. In: *Envisat & ERS Symposium*. Vol. 572.

Eichhorn, G. (2023). 'Landslide-pipeline interaction for onshore slopes in silty sand'. PhD thesis.

Enckell, M., B. Glisic, F. Myrvoll and B. Bergstrand (2011). 'Evaluation of a large-scale bridge strain, temperature and crack monitoring with distributed fibre optic sensors'. In: *Journal of Civil Structural Health Monitoring* 1, pp. 37–46.

ESA, European Space Agency (2012a). *COSMO-SkyMed*. Accessed on 2023-10-01. URL: https://www.eoportal.org/satellite-missions/cosmo-skymed.

— (2012b). *ERS-1 (European Remote-Sensing Satellite-1)*. Accessed on 2022-01-30. URL: https://www.eoportal.org/satellite-missions/ers-1.

— (2012c). *SeaSat (also called SeaSat-A or SeaSat-1)*. Accessed on 2022-01-30. URL: https://www.eoportal.org/satellite-missions/seasat#performance-specifications.

— (2012d). *SIR-A (Shuttle Imaging Radar)*. Accessed on 2022-01-30. URL: https://www.eoportal.org/satellite-missions/seasat#performance-specificationshttps://www.eoportal.org/other-space-activities/sir-a#sir-a-shuttle-imaging-radar--osta-1-payload-on-sts-2-mission.

— (2012e). *SRTM (Shuttle Radar Topography Mission)*. Accessed on 2022-01-30. URL: https://www.eoportal.org/satellite-missions/srtm.

— (2012f). *TSX (TerraSAR-X)*. Accessed on 2023-10-01. URL: https://www.eoportal.org/satellite-missions/terrasar-x.

— (2023). *Copernicus: Sentinel-1*. Accessed on 2023-10-01. URL: https://www.eoportal.org/satellite-missions/copernicus-sentinel-1#copernicus-sentinel-1--the-sar-imaging-constellation-for-land-and-ocean-services.

Ferretti, A., A. Fumagalli, F. Novali, C. Prati, F. Rocca and A. Rucci (2011). 'A new algorithm for processing interferometric data-stacks: SqueeSAR'. In: *IEEE transactions on geoscience and remote sensing* 49.9, pp. 3460–3470.

Ferretti, A., A. Monti-Guarnieri, C. Prati, F. Rocca and D. Massonet (2007). *InSAR principles-guidelines for SAR interferometry processing and interpretation*. Vol. 19.

Ferretti, A., A. Monti-Guarnieri, C. Prati, F. Rocca and D. Massonnet (2007). *InSAR Principles: Guidelines for SAR Interferometry Processing and Interpretation (ESA TM-19)*. ESA Publications.

Ferretti, A., C. Prati and F. Rocca (2000). 'Nonlinear subsidence rate estimation using permanent scatterers in differential SAR interferometry'. In: *IEEE Transactions on geoscience and remote sensing* 38.5, pp. 2202–2212.

— (2001). 'Permanent scatterers in SAR interferometry'. In: *IEEE Transactions on Geoscience and Remote Sensing* 39.1, pp. 8–20. DOI: 10.1109/36.898661.

Ge, D., Y. Wang, L. Zhang, X. Zhang, D. Yan and M. Li (2011). 'Integrating corner reflectors and PSInSAR technique to monitor regional land subsidence'. In: *2011 IEEE International Geoscience and Remote Sensing Symposium*. IEEE, pp. 1619–1622.

Giardina, G., P. Milillo, M. J. DeJong, D. Perissin and G. Milillo (2019a). 'Evaluation of InSAR monitoring data for post-tunnelling settlement damage assessment'. In: *Structural Control and Health Monitoring* 26.2, e2285.

— (2019b). 'Example applications of satellite monitoring for post-tunnelling settlement damage assessment for the Crossrail project in London'. In: *Structural analysis of historical constructions: An interdisciplinary approach*. Springer, pp. 2225–2235.

Goel, K. and N. Adam (2013). 'A distributed scatterer interferometry approach for precision monitoring of known surface deformation phenomena'. In: *IEEE Transactions on Geoscience and Remote Sensing* 52.9, pp. 5454–5468.

Guan, Jiang and Gao (2013). 'A calibration test of karst collapse monitoring device by optical time domain reflectometry (BOTDR) technique'. In: *Proceedings of the Thirteenth Multidisciplinary Conference on Sinkholes and the Engineering and Environmental Impacts of Karst (NCKRI Symposium 2)*. University of South Florida.

Guan, Z. (2015). 'Study on monitoring and early warning of karst collapse based on BOTDR technique'. In: *Proceedings of the Fourtheenth Multidisciplinary Conference on Sinkholes and the Engineering and Environmental Impacts of Karst (NCKRI Symposium 5)*.

Gue, C, M Wilcock, M Alhaddad, MZEB Elshafie, K Soga and R Mair (2014). 'Monitoring the effects of tunnelling under an existing tunnel-fibre optics'. In: *Proceedings of the Eigth International Symposium on Geotechnical Aspects of Underground Construction in Soft Ground*. CRC Press, pp. 357–361.

Güemes, A., A. Fernández-López and B. Soller (2010). 'Optical fiber distributed sensing-physical principles and applications'. In: *Structural Health Monitoring* 9.3, pp. 233–245.

Gutiérrez, F., A. B. Calvo, D. Carbonel, G. Desir, J. Sevil, J. Guerrero, A. M. Fernández, T. Karamplaglidis, A. G. Arnay and I. Fabregat (2019). 'Review on sinkhole monitoring and performance of remediation measures by high-precision leveling and terrestrial laser scanner in the salt karst of the Ebro Valley, Spain'. In: *Engineering Geology* 248, pp. 283–308. DOI: https://doi.org/10.1016/j.enggeo.2018.12.004.

Henderson, F. M. and A. J. Lewis (1998). *Principles and applications of imaging radar. Manual of remote sensing: Volume 2*. John Wiley and Sons, Inc., Somerset, NJ (United States).

Hetland, E. A., P. Musé, M. Simons, Y. N. Lin, P. S. Agram and C. J. DiCaprio (2012). 'Multiscale InSAR time series (MInTS) analysis of surface deformation'. In: *Journal of Geophysical Research: Solid Earth* 117.B2.

Hooper, A., H. Zebker, P. Segall and B. Kampes (2004). 'A new method for measuring deformation on volcanoes and other natural terrains using InSAR persistent scatterers'. In: *Geophysical research letters* 31.23.

Iglesia, G. R., H. H. Einstein and R. V. Whitman (2014). 'Investigation of soil arching with centrifuge tests'. In: *Journal of Geotechnical and Geoenvironmental engineering* 140.2, p. 04013005.

Inaudi, D. (2014). 'Sensing solutions for assessing the stability of levees, sinkholes and landslides'. In: *Sensor technologies for civil infrastructures*. Elsevier, pp. 396–421.

Innovations, Luna (2020). *Optical distributed sensor interrogator model ODiSI 6100: data sheet*. Blacksburg, VA, USA: Luna Innovations Incorporated.

ISTAT, Istituto Nazionale di Statistica (2022). *Turismo in Italia nel 2018*. Accessed on 2023-09-30. URL: https://www.istat.it/it/archivio/232137.

Kampes, B. M. (2006). 'Radar interferometry: persistent scatterers technique'. PhD thesis.

Kechavarzi, C., K. Soga, N. de Battista, L. Pelecanos, M. Z. E. B. Elshafie and R. J. Mair (2016). *Distributed Fibre Optic Strain Sensing for Monitoring Civil Infrastructure*. ICE Publishing. DOI: 10.1680/dfossmci.60555.

Klar, A., P. J. Bennett, K. Soga, R. J. Mair, P. Tester, R. Fernie, H. D. St John and G. Torp-Peterson (2006). 'Distributed strain measurement for pile foundations'. In: *Proceedings of the Institution of Civil Engineers-Geotechnical Engineering*. Vol. 159. 3. Thomas Telford Ltd, pp. 135–144.

Klar, A., I. Dromy and R. Linker (2014). 'Monitoring tunneling induced ground displacements using distributed fiber-optic sensing'. In: *Tunnelling and Underground Space Technology* 40, pp. 141–150.

Kogure, T. and Y. Okuda (2018). 'Monitoring the vertical distribution of rainfall-induced strain changes in a landslide measured by distributed fiber optic sensing with Rayleigh backscattering'. In: *Geophysical Research Letters* 45, pp. 4033–4040. DOI: 10.1029/2018GL077607.

Lancelot, L., I. Shahrour and Marwan. Al Mahmoud (2006). 'Failure and dilatancy properties of sand at relatively low stresses'. In: *Journal of Engineering Mechanics* 132.12, pp. 1396–1399.

Lanticq, V., E. Bourgeois, P. Magnien, L. Dieleman, G. Vinceslas, A. Sang and S. Delepine-Lesoille (2009). 'Soil-embedded optical fiber sensing cable interrogated by Brillouin optical time-domain reflectometry (B-OTDR) and optical frequency-domain reflectometry (OFDR) for embedded cavity detection and sinkhole warning system'. In: *Measurement Science and Technology* 20.3, p. 034018.

Linker, R. and A. Klar (2017). 'Detection of sinkhole formation by strain profile measurements using BOTDR: Simulation study'. In: *Journal of Engineering Mechanics* 143.3, B4015002.

López-Quiroz, P., M. Doin, F. Tupin, P. Briole and J. M. Nicolas (2009). 'Time series analysis of Mexico City subsidence constrained by radar interferometry'. In: *Journal of Applied Geophysics* 69.1, pp. 1–15.

Lv, X., B. Yazıcı, M. Zeghal, V. Bennett and T. Abdoun (2014). 'Joint-scatterer processing for time-series InSAR'. In: *IEEE Transactions on Geoscience and Remote Sensing* 52.11, pp. 7205–7221.

Macchiarulo, V., P. Milillo, M. J. DeJong, J. Gonzalez Marti, J. Sánchez and G. Giardina (2021). 'Integrated InSAR monitoring and structural assessment of tunnelling-induced building deformations'. In: *Structural Control and Health Monitoring* 28.9, e2781.

Mair, R. J. and R. N. Taylor (1997). 'Theme lecture: Bored tunnelling in the urban environment'. In: *Proceedings of the fourteenth international conference on soil mechanics and foundation engineering*. Rotterdam, pp. 2353–2385.

Meng, F. Ansari and X. Feng (2015). 'Detection and monitoring of surface micro-cracks by PPP-BOTDA'. In: *Applied optics* 54.16, pp. 4972–4978.

Meng, L., J. Zou and G. Liu (2020). 'Research on the Design and Automatic Recognition Algorithm of Subsidence Marks for Close-Range Photogrammetry'. In: *Sensors* 20, p. 544. DOI: 10.3390/s20020544.

Milillo, P., G. Giardina, M. J. DeJong, D. Perissin and G. Milillo (2018). 'Multi-temporal InSAR structural damage assessment: The London crossrail case study'. In: *Remote Sensing* 10.2, p. 287.

Minardo, A., E. Catalano, A. Coscetta, G. Zeni, C. Di Maio, R. Vassallo, L. Picarelli, R. Coviello, G. Macchia and L. Zeni (2021). 'Long-term monitoring of a tunnel in a landslide prone area by Brillouin-based distributed optical fiber sensors'. In: *Sensors* 21.21, p. 7032.

MN, Metropolitana di Napoli s.p.a. (2020). *Al via i lavori di scavo del tunnel Capodichino*. Accessed on 2022-12-16. URL: https://www.metropolitanadinapoli.it/tunnel-capodichino-poggioreale-visita-sindaco.

— (2021). *Termina lo scavo della prima galleria da Capodichino a Poggioreale*. Accessed on 2022-09-30. URL: https://www.metropolitanadinapoli.it/metropolitana-linea-1-prima-galleria-da-capodichino-a-poggioreale/.

Möller, T., T. S. da Silva Burke, X. Xu, G. Della Ragione, E. Bilotta and C. N. Abadie (2023). 'Distributed fibre optic sensing for sinkhole early warning: experimental study'. In: *Géotechnique* 73.8, pp. 701–715. DOI: 10.1680/jgeot.21.00154.

Mora, O., J. J. Mallorqui and A. Broquetas (2003). 'Linear and nonlinear terrain deformation maps from a reduced set of interferometric SAR images'. In: *IEEE Transactions on Geoscience and Remote Sensing* 41.10, pp. 2243–2253.

Moritz, B., R. Heissenberger, T. Schachinger and W. Lienhart (2021). 'Long-term monitoring of railway tunnels'. In: *Geomechanics and Tunnelling* 14.1, pp. 35–46.

O'Reilly, M. P. and B. M. New (1982). *Settlements above tunnels in the United Kingdom-their magnitude and prediction*. Tech. rep.

Ohno, H., H. Naruse, M. Kihara and A. Shimada (2001). 'Industrial applications of the BOTDR optical fiber strain sensor'. In: *Optical fiber technology* 7.1, pp. 45–64.

Oztoprak, S. and M. D. Bolton (2011). 'Parameter calibration of a modified hyperbolic model for sands using pressuremeter test data'. In: *Deformation Characteristics of Geomaterials*. IOS Press, pp. 949–956.

Peck, R. B. (1969). 'Deep excavations and tunneling in soft ground'. In: *7th International Conference on Soil Mechanics and Foundation Engineering*.

Perissin, D. (2016). 'Interferometric SAR multitemporal processing: Techniques and applications'. In: *Multitemporal Remote Sensing: Methods and Applications*, pp. 145–176.

— (2018). 'Geometric Processing: Active Sensor Modeling and Calibration (SAR)'. In: *Comprehensive Remote Sensing*. Elsevier, pp. 61–76.

Perissin, D., F. Rocca, M. Pierdicca, E. Pichelli, D. Cimini, G. Venuti and B. Rommen (2011). 'Mitigation of atmospheric delay in InSAR: The ESA Metawave project'. In: *2011 IEEE International Geoscience and Remote Sensing Symposium*. IEEE, pp. 2558–2561.

Perissin, D., Z. Wang and H. Lin (2012). 'Shanghai subway tunnels and highways monitoring through Cosmo-SkyMed Persistent Scatterers'. In: *ISPRS Journal of Photogrammetry and Remote Sensing* 73, pp. 58–67.

Perissin, D., Z. Wang and T. Wang (2011). 'The SARPROZ InSAR tool for urban subsidence/manmade structure stability monitoring in China'. In: vol. 1015.

Rankin, W. J. (1988). 'Ground movements resulting from urban tunnelling: predictions and effects'. In: *Geological Society, London, Engineering Geology Special Publications* 5.1, pp. 79–92.

Regione Campania, Dipartimento 52 della Salute e delle Risorse Naturali Direzione Generale 5 per l'ambiente e l'ecosistema U.O.D. 7 Valutazioni ambientali (2013). *Relazione Geologica e Geotecnica, Decreto Dirigenziale n. 267 del 09/12/2013*.

Sadek, M. and I. Shahrour (2004). 'A three dimensional embedded beam element for reinforced geomaterials'. In: *International journal for numerical and analytical methods in geomechanics* 28.9, pp. 931–946.

Sagaseta, C. (1987). 'Analysis of undrained soil deformation due to ground loss'. In: *Geotechnique* 37.3, pp. 301–320.

Santangelo, V., E. Bilotta, D. Di Martire, M. Ramondini and G. Russo (2021). 'An application of A-DInSAR for monitoring tunnelling induced displacements in urban area. The case study of the Naples Metro Line 6 stretch Mergellina-Chiaia'. In: *Gallerie e Grandi Opere Sotterranee* 9, pp. 31–38.

Schanz, T. and P. A. Vermeer (1996). 'Angles of friction and dilatancy of sand'. In: *Géotechnique* 46.1, pp. 145–151.

Schanz, T., P. A. Vermeer and P. G. Bonnier (1999). 'The hardening soil model: formulation and verification'. In: *Beyond 2000 in computational geotechnics* 1, pp. 281–296.

Schmidt, B. (1969). *Settlements and ground movements associated with tunneling in soil*. University of Illinois at Urbana-Champaign.

Schmidt, D. A. and R. Bürgmann (2003). 'Time-dependent land uplift and subsidence in the Santa Clara valley, California, from a large interferometric synthetic aperture radar data set'. In: *Journal of Geophysical Research: Solid Earth* 108.B9.

Shen, N., B. Wang, H. Ma, X. Zhao, Y. Zhou, Z. Zhang and J. Xu (2023). 'A review of terrestrial laser scanning (TLS)-based technologies for deformation monitoring in engineering'. In: *Measurement* 223, p. 113684. DOI: https://doi.org/10.1016/j.measurement.2023.113684.

Soga, K. (2023). 'Smart Infrastructure for Smart Cities'. In: *BRIDGE*, p. 22.

Soga, K., C. Kechavarzi, L. Pelecanos, N. de Battista, M. Williamson, C. Y. Gue, V. Di Murro, M. Elshafie, D. Monzón-Hernández Sr, E. Bustos et al. (2018). 'Fiber-optic underground sensor networks'. In: *Underground sensing*. Elsevier, pp. 287–356.

Stanier, S. A., J. Blaber, W. A. Take and D. J. White (2016). 'Improved image-based deformation measurement for geotechnical applications'. In: *Canadian Geotechnical Journal* 53.5, pp. 727–739.

Sun, Y., B. Shi, D. Zhang, H. Tong, G. Wei, H. Xu et al. (2016). 'Internal deformation monitoring of slope based on BOTDR'. In: *Journal of Sensors* 2016.

Suwansawat, S. and H. H. Einstein (2007). 'Describing settlement troughs over twin tunnels using a superposition technique'. In: *Journal of geotechnical and geoenvironmental engineering* 133.4, pp. 445–468.

Taylor, R. N. (1995). 'Tunnelling in soft ground in the U.K.' In: *Underground Construction in Soft Ground*. Ed. by Fujita and Kusakabe.

— (2018). *Geotechnical centrifuge technology*. CRC Press.

Török, Viktória (2021). '3D numerical analysis of tunnelling effects on a multi-storey building: the case of Line 9 EPB tunnelling in Barcelona'. MA thesis. Universitat Politècnica de Catalunya.

Van Leijen, F. J. (2014). 'Persistent scatterer interferometry based on geodetic estimation theory'. PhD thesis.

Villalba, S. and J. R. Casas (2013). 'Application of optical fiber distributed sensing to health monitoring of concrete structures'. In: *Mechanical Systems and Signal Processing* 39.1-2, pp. 441–451.

Villard, P. and L. Briancon (2008). 'Design of geosynthetic reinforcements for platforms subjected to localized sinkholes'. In: *Canadian Geotechnical Journal* 45.2, pp. 196–209.

Vollset, S. E., E. Goren, C. Yuan, J. Cao, A. E. Smith, T. Hsiao, C. Bisignano, G. S. Azhar, E. Castro, J. Chalek et al. (2020). 'Fertility, mortality, migration, and population scenarios for 195 countries and territories from 2017 to 2100: a forecasting analysis for the Global Burden of Disease Study'. In: *The Lancet* 396.10258, pp. 1285–1306.

Webb, G. T., P. J. Vardanega, N. A. Hoult, P. R. A. Fidler, P. J. Bennett and C. R. Middleton (2017). 'Analysis of fiber-optic strain-monitoring data from a prestressed concrete bridge'. In: *Journal of Bridge Engineering* 22.5, p. 05017002.

Werner, C., U. Wegmuller, T. Strozzi and A. Wiesmann (2003). 'Interferometric point target analysis for deformation mapping'. In: *IGARSS 2003. 2003 IEEE International Geoscience and Remote Sensing Symposium. Proceedings (IEEE Cat. No. 03CH37477)*. Vol. 7. IEEE, pp. 4362–4364.

Wichtmann, T. and T. Triantafyllidis (2004). 'Influence of a cyclic and dynamic loading history on dynamic properties of dry sand, part I: cyclic and dynamic torsional prestraining'. In: *Soil Dynamics and Earthquake Engineering* 24.2, pp. 127–147.

Xu, J., Y. Dong, Z. Zhang, S. Li, S. He and H. Li (2016). 'Full scale strain monitoring of a suspension bridge using high performance distributed fiber optic sensors'. In: *Measurement Science and Technology* 27.12, p. 124017.

Xu, X., C. N. Abadie, T. Möller, G. Della Ragione and T. S. Da Silva Burke (2022). 'On the use of high-resolution distributed fibre optic sensing for small-scale geotechnical experiments at 1g'. In: *10th International Conference on Physical Modelling in Geotechnics.(ICPMG)*.

Xu, X., C. Kechavarzi, D. Wright, G. Horgan, H. Hangen, N. De Battista, D. Woods, E. Bertrand, S. Trinder and N. Sartain (2022). 'Fibre optic instrumented geogrid for ground movement detection'. In: *11th International Symposium on Field Monitoring in Geomechanics (ISFMG2022). London, U.K.*

Young, A. (2013). 'Inequality, the urban-rural gap, and migration'. In: *The Quarterly Journal of Economics* 128.4, pp. 1727–1785.

Zhang, C., H. Zhu and B. Shi (2016). 'Role of the interface between distributed fibre optic strain sensor and soil in ground deformation measurement'. In: *Scientific Reports* 6.1, p. 36469.

Zheng, G., R. Wang, H. Lei, T. Zhang, J. Guo and Z. Zhou (2023). 'Relating twin-tunnelling-induced settlement to changes in the stiffness of soil'. In: *Acta Geotechnica* 18.1, pp. 469–482.